On transport properties of Weyl semimetals
Baireuther, P.S.

Citation

Baireuther, P. S. (2017, April 26). *On transport properties of Weyl semimetals*. Retrieved from https://hdl.handle.net/1887/48876

Cover Page

The handle http://hdl.handle.net/1887/48876 holds various files of this Leiden University dissertation

Author: Baireuther, P.S.
Title: On transport properties of Weyl semimetals
Issue Date: 2017-04-26

On transport properties
of Weyl semimetals

Paul Sebastian Baireuther

geboren te Freiburg im Breisgau (Duitsland) in 1985

Promotores: Prof. dr. C. W. J. Beenakker
Prof. dr. Yu. V. Nazarov (Technische Universiteit Delft)
Co-promotor: Dr. J. Tworzydło (University of Warsaw)

Promotiecommissie: Prof. dr. İ. Adagideli (Sabancı University, Istanbul)
Prof. dr. ir. A. Brinkman (Universiteit Twente)
Dr. V. Cheianov
Prof. dr. E. R. Eliel
Prof. dr. J. Zaanen

Cover: Density of states of an Amperian superconductor as a function of
energy and momentum (cf. Fig. 5.1, Chapter 5).

To Orkide and to my parents.

Contents

Contents

1 Introduction

1.1 Preface

Band theory is one of the most powerful quantum mechanical tools available to understand the electronic properties of crystalline solids. It has been extremely successful in grouping a wide variety of materials into just two categories: metals and insulators. In a metal, the Fermi energy lies within a band, called the conduction band. A metal is characterized by its finite conductivity at zero temperature. In an insulator, the Fermi energy lies in a gap between a fully occupied valence band and an empty conduction band. At zero temperature, the conductivity of an insulator is zero.

The finite band gap at the Fermi energy of insulators allows us to adiabatically transform different Hamiltonians with the same symmetries into one another while remaining in the ground state. However, this is not always possible. There are Hamiltonians of insulators that cannot be transformed into each other without closing the bulk gap, despite them having the same symmetries. Such insulators are topologically distinct [1].

In mathematics topology is a way to distinguish objects that cannot be transformed into each other without tearing or cutting them. For example, consider two-dimensional surfaces. If the number of holes ('genus') in two such surfaces is not the same, they can not be transformed into one another continuously. The surface of a sphere is topologically equivalent to the surface of a vase, but not to the surface of a pipe, which is in turn equivalent to the surface of a coffee mug.

In the context of topological insulators one can identify so-called topological invariants, which are integer numbers, very much like the genus of a surface. While the genus is related to the numbers of holes in the surface, the topological invariants are related to the number of topologically protected edge states at the interface of two topologically distinct insulators. These edge states are robust to weak disorder [2–4] and cannot be gapped, as long as the perturbations do not break the symmetries of the system or close the insulating bulk gap.

During the last decade, topological insulators have been in the center of attention of condensed matter research [5–9]. This thesis is concerned

with a new class of topological materials, that has emerged very recently: Topological semimetals [10–18].

Semimetals are in-between metals and insulators. In semimetals, the bottom of the conduction band overlaps with the top of the valence band. Therefore, they have a gapless spectrum, which forbids adiabatic transformations. At first sight, it is therefore counterintuitive that a semimetal can have topological properties. If translation symmetry is preserved, however, we can look at the semimetal in reciprocal space. A key distinction to a normal metal is that the Fermi surface is very small. In a topological semimetal the Fermi surface shrinks all the way to a point.

Although the topological semimetal is not fully gapped, it is possible to construct planes in the Brillouin zone in which the spectrum is gapped. These planes are characterized by topological invariants [8, 19], much like the topological insulators. The bulk-boundary correspondence then implies that there exist topologically protected surface states [10]. In contrast to topological insulators, in a topological semimetal these states are only defined in parts of the Brillouin zone — they merge with the bulk bands near the gapless regions.

The focus in this thesis is on a particular topological semimetal called a *Weyl semimetal* [18, 20–22]. At first sight, a Weyl semimetal is just a three-dimensional version of graphene. However, the third spatial dimension plays a subtle, but powerful role, that distinguishes Weyl semimetals from graphene. Unlike in graphene, the existence and stability of the gapless points in the spectrum (so-called Weyl points) is not guaranteed by a symmetry, but by the third spatial dimension itself. The Weyl points are protected by a topological invariant (the so-called chirality or Berry flux) and cannot be removed by local perturbations. The only way to open a gap is to merge two Weyl points of opposite chirality. The chirality of the Weyl points leads to remarkable electronic properties, such as chiral Landau levels and the chiral magnetic effect. These, and other properties that distinguish Weyl semimetals from graphene, are the core subjects of this thesis.

1.2 Weyl semimetals

1.2.1 Band structure

Just like in graphene, the low-energy spectrum of a Weyl semimetal has a linear energy-momentum relation. The low-energy excitations are massless and move with an energy-independent velocity (analogous to the speed
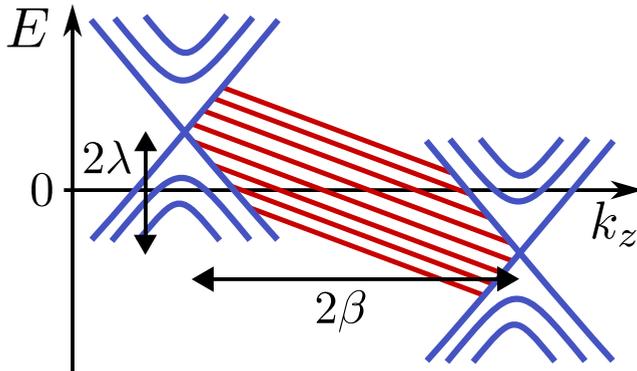
Figure 1.1: Schematic drawing of the energy-momentum relation of a Weyl semimetal slab. The bulk Weyl cones (blue) are separated in momentum space by a time-reversal-symmetry breaking magnetization β. If inversion symmetry is broken ($\lambda \neq 0$), the Weyl points are displaced with respect to each other in energy. On the surface the projection of the Weyl cones are connected by chiral edge states (red).

of light for photons). Many of the remarkable electronic properties of graphene, such as Klein tunneling [23–25], are therefore also present in Weyl semimetals. If we consider a slab geometry, which is finite in one direction and translationally invariant in the other two directions, the surface states look just like the dispersionless surface states of graphene with a zigzag edge. A schematic drawing of the band structure is shown in Fig. 1.1. In our numerical simulations, we use a tight-binding model

$$\begin{aligned}
\mathcal{H}(\boldsymbol{k}) &= \tau_z(t'\sigma_x \sin k_x + t'\sigma_y \sin k_y + t'_z\sigma_z \sin k_z) \\
&\quad + m(\boldsymbol{k})\tau_x\sigma_0 + \beta\tau_0\sigma_z + \lambda\tau_z\sigma_0 \\
m(\boldsymbol{k}) &= m_0 + t(2 - \cos k_x - \cos k_y) + t_z(1 - \cos k_z),
\end{aligned} \quad (1.1)$$

which is equivalent to the model introduced in [26], up to a unitary transformation. The Pauli matrices σ and τ represent spin and orbital degrees of freedom. (For brevity, we will set $\hbar \equiv 1$, and often also the lattice constant $a \equiv 1$.) The first two terms in Eq. 1.1 describe a Weyl semimetal with eight Weyl cones located at $\boldsymbol{k} = (\{0, \pi\}, \{0, \pi\}, \pm\beta)$ for small β. The third term, the "mass term" $\mu(\boldsymbol{k})$, gaps the Weyl points at $k_x = \pi$ and $k_y = \pi$ so that only two Weyl points remain at $\boldsymbol{k} = (0, 0, \pm\beta)$. The inversion breaking term b_0 shifts the Weyl cones in energy in opposite directions.

1.2.2 Topological properties

To understand the topological properties of a Weyl semimetal, we first focus on a single, non-degenerate Weyl cone. Such a Weyl-cone consists of a conduction band and a valence band, that *accidentally* touch at single point, the Weyl point. The Hamiltonian of a single isotropic Weyl cone reads

$$H = \chi v_F (k_x \sigma_x + k_y \sigma_y + k_z \sigma_z), \tag{1.2}$$

where $\chi = \pm$ is the chirality, v_F is the Fermi velocity, k_i a momentum component, and σ_i a spin Pauli matrix. In this context, chirality means that the momentum and the spin of electrons in a given Weyl cone are (anti-)parallel.

The Weyl Hamiltonian in Eq. 1.2 looks almost like the Hamiltonian for a single Dirac cone in graphene, with the key difference that all three Pauli matrices are coupled to the momentum. Therefore, adding any additional terms to the Hamiltonian, e.g. $m\sigma_z$, only shifts the Weyl point in momentum space or energy, but does not open a gap. This is what we mean when we say that the Weyl points are topologically protected.

To understand the existence of topologically protected surface states, we need to consider a pair of Weyl points with opposite chirality. Let us assume that those Weyl points are located at $\boldsymbol{k}_\chi = (0, 0, \chi k_0)$. Because the band structure of a Weyl semimetal is gapless, topological invariants [1] are not well defined. However, as mentioned in the preface, if translation symmetry is conserved, we can define the three-dimensional Brillouin zone as a stack of two dimensional planes S_{k_z}, labeled by the third component of the momentum k_z. (This is called dimensional reduction [19, 27, 28].) The spectra of all planes, except for those that contain Weyl points, are gapped. We can therefore calculate their topological invariants, the so-called Chern numbers,

$$C_{k_z} = \frac{1}{2\pi} \int_{S_{k_z}} d\boldsymbol{k} \cdot \boldsymbol{B}(\boldsymbol{k}) \tag{1.3}$$

by integrating the Berry flux

$$\boldsymbol{B}(\boldsymbol{k}) = \nabla_{\boldsymbol{k}} \times i \sum_n^{\text{filled}} \langle u_n(\boldsymbol{k}) | \nabla_{\boldsymbol{k}} | u_n(\boldsymbol{k}) \rangle \tag{1.4}$$

over all filled bands [1], where $u_n(\boldsymbol{k})$ are Bloch wave functions.

By calculating the Berry flux through a sphere that encloses one of the Weyl points, we see that Weyl points are sources and sinks of Berry flux [29], depending on their chirality. The Berry flux flows from the Weyl cone

with positive chirality to the Weyl cone with negative chirality via the time-reversal invariant points. Therefore, all planes in-between* the Weyl points have a non-trivial Chern number and are topological insulators with topologically protected surface states [10]. The Chern number of the planes outside of the Weyl points is zero, and hence they do not have topological surface states. The property that Weyl points are sources and sinks of Berry flux is another way to see that they must be topologically protected: The only way to annihilate a pair of Weyl points is to merge a source with a sink.

1.2.3 Landau levels

The Landau levels of massive electrons are quantized as $E_n \sim \sqrt{n + 1/2}$. For the massless electrons in graphene the $1/2$ offset is absent, and the $n = 0$ Landau level is magnetic-field independent [30]. In a three-dimensional Weyl semimetal the Landau levels also posses a dispersion along the direction of the magnetic field. The zeroth Landau level is chiral and disperses only in one direction [31].

To derive the Landau levels of a Weyl semimetal, we consider a single isotropic Weyl cone with chirality χ and include the vector potential $\boldsymbol{A}$ of the magnetic field via

$$H = \chi v_F (\boldsymbol{k} - q\boldsymbol{A}) \cdot \boldsymbol{\sigma}, \tag{1.5}$$

where we will assume $q > 0$. We take the magnetic field in the z-direction and choose the symmetric gauge

$$\boldsymbol{A} = (-By/2, Bx/2, 0). \tag{1.6}$$

An instructive way [32–34] to calculate the spectrum of such a Hamiltonian is to introduce the canonical momenta

$$\Pi_x \equiv k_x + qBy/2 \qquad \Pi_y \equiv k_x - qBx/2, \tag{1.7}$$

whose commutation relation is given by

$$[\Pi_x, \Pi_y] = iqB. \tag{1.8}$$

---

*"In-between" the Weyl points is defined is as follows: In a Dirac semimetal, the Dirac cones are doubly degenerate. By breaking inversion or time-reversal symmetry, these cones become separated from each other in the Brillouin zone. "In-between" the Weyl points is then defined as a line in the Brillouin zone that connects the Weyl points via the Dirac point from which they emerged.
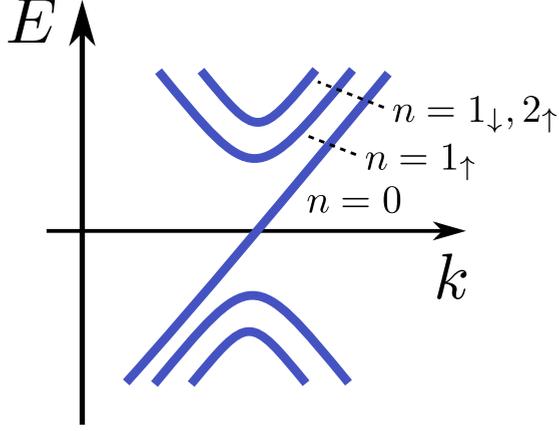
Figure 1.2: Landau levels of a single Weyl cone with positive chirality $\chi = +$.

In the z-direction, the motion is not affected by the magnetic field. In the usual way, we introduce raising and lowering operators

$$a = \sqrt{\tfrac{1}{2qB}}(\Pi_x + i\Pi_y), \qquad a^\dagger = \sqrt{\tfrac{1}{2qB}}(\Pi_x - i\Pi_y), \qquad (1.9)$$

which act on the Landau level index n. In this notation, the Hamiltonian reads*

$$H = \chi\sqrt{2qB}v_F(a\sigma_- + a^\dagger\sigma_+) + \chi v_F k_z \sigma_z, \qquad (1.10)$$

where $\sigma_\pm = (\sigma_x \pm i\sigma_y)/2$. The zeroth Landau level ($n = 0$) is special [31], the only eigenstate is

$$H|n = 0, k_z, \uparrow\rangle = \chi v_F k_z |n = 0, k_z, \uparrow\rangle. \qquad (1.11)$$

The higher Landau levels can be found by squaring the Hamiltonian

$$H^2 = qBv_F^2(2a^\dagger a + 1 - \sigma_z) + v_F^2 k_z^2. \qquad (1.12)$$

From this, we can read off the $n \geq 1$ Landau levels

$$E_{n,\uparrow} = \pm v_F\sqrt{k_z^2 + 2qBn} \quad \text{and} \quad E_{n,\downarrow} = \pm v_F\sqrt{k_z^2 + 2qB(n+1)}, \quad (1.13)$$

which are illustrated in Fig. 1.2.

---

*We used the convention $q > 0$.

1.2.4 Chiral anomaly

The chiral anomaly is the condensed matter analogue of the Adler-Bell-Jackiw anomaly from particle physics [35, 36]. In high-energy physics, massless fermions in odd spatial dimensions have chiral symmetry. This means that the number of fermions with a given chirality, and therefore the total chiral charge, is conserved. In a Weyl semimetal, the low-energy physics is described by the same relativistic equation. However, chiral symmetry can be broken by applying a magnetic and an electric field in parallel. The electric field pumps electrons from one Weyl cone to the other, therefore changing the total chiral charge. This so-called chiral anomaly has been studied in the condensed matter context for some time [31, 37, 38].

Many of the most fascinating transport phenomena of Weyl semimetals are direct consequences of the chiral anomaly, most famously the huge magnetoconductance [31, 39–41] and the chiral magnetic effect [42–46].

1.2.5 Surface states

The surface band of a Weyl semimetal is one of its most remarkable features and a key experimental signature. The Fermi surfaces, that are formed by the intersection of the surface bands with the Fermi energy, are called Fermi arcs. They are open lines which run from one projection of a Weyl cone to another [10]. This is illustrated in Fig. 1.3 a. Usually, Fermi surfaces are closed contours, separating filled from empty states. So how can an open Fermi surface exist? They answer is that the Fermi arcs on both surfaces complement each other. Together, they form a closed Fermi surfaces [47]. If we were to make the Weyl semimetal thinner and thinner, the Fermi arcs would eventually merge into a closed Fermi surfaces.

The real-space properties of the surface states are also unusual and interesting. They are chiral, in the sense that they disperse only in one direction, circling around the direction of the internal magnetization. If inversion symmetry is broken, their velocity also has a component along the magnetization. In a cylinder geometry, where the Weyl cones are separated along the translationally invariant axis, the surface states have the shape of a solenoid and spiral along the cylinder surface as shown in Fig. 1.3 b.
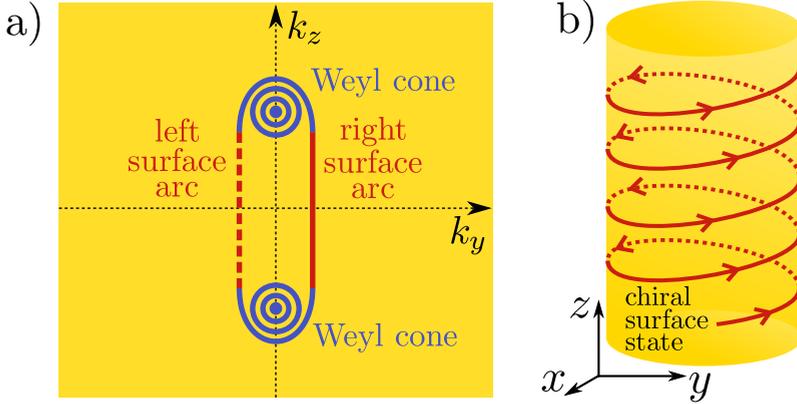
Figure 1.3: Left: Schematic illustration of the density of states of a Weyl semimetal in a slab geometry at an energy slightly away from the band touching point. The slab is finite in the x-direction with width W and translation invariant in the y- and z-directions. Due to finite size quantization, the density of states of the Weyl cones consists of several discrete circles (blue). The surface arcs (red) at the left $(x = 0)$ and right $(x = W)$ surface connect near the Weyl cones. Together, they form a closed contour. Right: For a cylindrical Weyl semimetal wire, the chiral surface states have the shape of a solenoid.

1.2.6 Experimental realizations

The interest in Weyl semimetals exploded with their experimental discovery in 2015. The first experimental realization was in tantalum arsenide (TaAs) [48–51]. Soon after, Weyl semimetals were reported in niobium arsenide (NbAs) [52] and tantalum phosphide (TaP) [53]. It turns out all of those materials have a very similar screw-like crystal structure. They are symmetric under a combination of rotation and translation [52, 53], a so-called non-symmorphic C_4 symmetry.

All of these pioneering experiments used a combination of low- and high-energy angle-resolved photoemission spectroscopy (ARPES). The low-energy (ultraviolet) ARPES probes the surface dispersion and shows the Fermi arcs. The high-energy (soft X-ray) ARPES probes the underlying bulk dispersion and shows the Weyl cones. One of the most impressive proofs that TaAs is indeed a Weyl semimetal is shown in Fig. 1.4. In the top part (green), a low-energy ARPES map shows the Fermi arcs on the surface. In the bottom part, the low-energy ARPES map is overlaid with a high energy ARPES map, which shows the projections of the Weyl
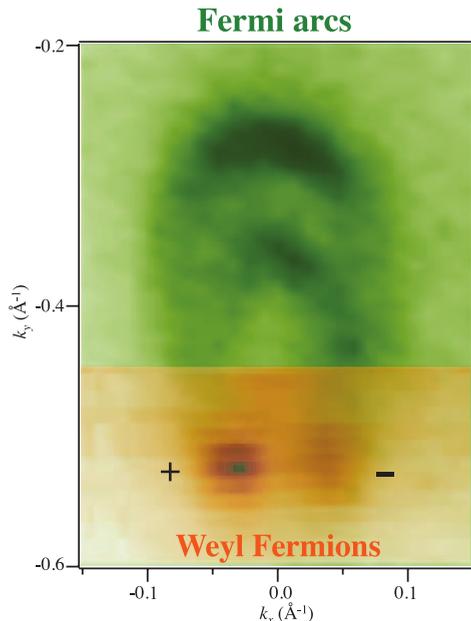
Figure 1.4: High-resolution ARPES maps of TaAs. Green region: Surface state Fermi surface map (darker color means higher ARPES signal). Brown region: Surface state Fermi surface map overlaid with bulk Fermi surface map. The surface Fermi arcs indeed terminate at the projections of the bulk Weyl points on the surface Brillouin zone. Figure from Ref. [48]. Reprinted with permission from AAAS.

points onto the surface Brillouin zone. We see that the Fermi arcs indeed terminate at projections of the Weyl points.

So far, all experimental realizations are Weyl semimetals with preserved time-reversal symmetry. However, several proposals have been put forward on how to realize Weyl semimetals with broken time-reversal symmetry [10, 54, 55]. In this thesis, we focus on the time-reversally broken situation, because it provides the minimal number of two Weyl points — when time-reversal symmetry is preserved one must have at least four Weyl points.
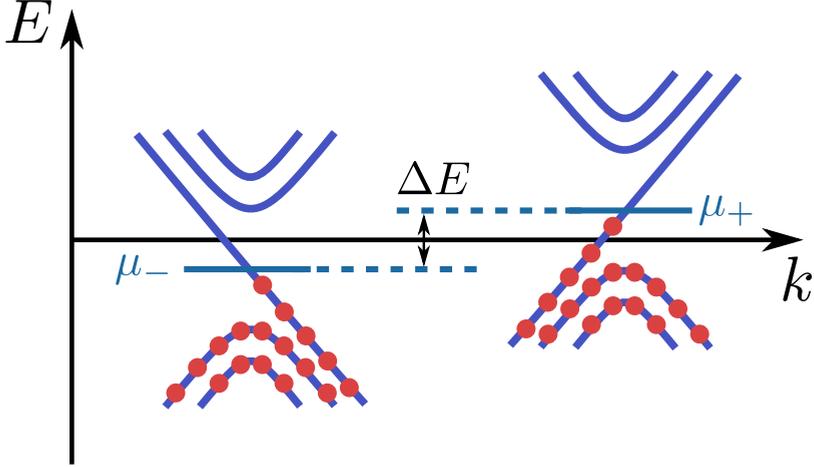
Figure 1.5: Illustration of the chiral chemical potentials μ_χ induced by an inversion breaking perturbation. The energy difference between the two Weyl points ΔE is the difference of the chiral chemical potentials.

1.3 Chiral magnetic effect

The Chiral Magnetic Effect (CME) is a "topological" current response, that is directly related to the chiral anomaly. Its universal value

$$j = (e/h)^2 \Delta E\, B \tag{1.14}$$

does not depend on the details of the material or model. The only terms that enter are the energy displacement of the Weyl points ΔE and the amplitude of the external magnetic field B. Initially, it was believed that the chiral magnetic effect might be a static current response. However, it is now understood that a slow periodic modulation of either ΔE or B is needed to overcome relaxation. The reason is that in any real system, there will always be a relaxation channel that scatters between the Weyl cones, even though this scattering is suppressed by the separation of the Weyl cones in the Brillouin zone. In this thesis, we therefore study the CME as a response to an oscillating parameter. The CME is one of the unique features of a Weyl semimetals that sets it apart from graphene.
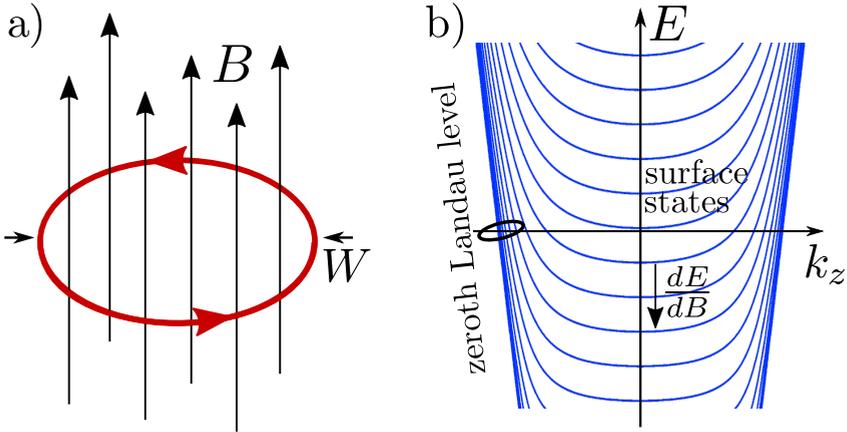
Figure 1.6: Left: In a wire geometry with diameter W, the chiral surface state encircles the entire magnetic flux. Right: Low-energy dispersion of a Weyl semimetal in a strong magnetic field. The surface states merge near the Weyl points and form the zeroth Landau levels (cf. Fig. 3.1, Chapter 3).

1.3.1 Chiral magnetic effect with Landau levels

In the first studies of the chiral magnetic effect [42–45], a Weyl semimetal was placed into a static magnetic field, strong enough for Landau levels to develop. Then, by means of an inversion symmetry breaking perturbation, the Weyl cones were periodically shifted up and down in energy in opposite directions. This so-called chiral chemical potential $\mu_\chi \approx \chi\lambda$ creates a non-equilibrium distribution at each Weyl cone, as illustrated in Fig. 1.5. The chiral Landau levels carry electron and hole currents in opposite directions. Together, they create a universal current density (Eq. 1.14).

We can derive the universal coefficient $(e/h)^2$ by very simple arguments, using an approach similar to the well-known Landauer formula, which we introduce in chapter 3. In contrast to the original Landauer formula, here the reservoirs are separated in momentum space rather than in real space. The contribution of the Weyl cone with positive chirality to the current is the product of the conductance per mode, the number of modes, and the chiral voltage μ_+/e. The conductance per mode is e^2/h and the degeneracy of the zeroth Landau level $B\mathcal{A}/\Phi_0$, where $\mathcal{A}$ is the cross section of the wire and $\Phi_0 = h/e$ is the magnetic flux quantum.

Altogether, the current response is given by

$$I_+ = \frac{e^2}{h} \frac{e\mathcal{A}B}{h} \frac{\mu_+}{e}. \tag{1.15}$$

The zeroth Landau level of the Weyl cone with negative chirality disperses in the opposite direction. At the same time, the chiral chemical potential of the other Weyl cone is the negative equal $\mu_- = -\mu_+$. Therefore, both Weyl cones contribute equally to the current, resulting in the current density 1.14.

1.3.2 Chiral magnetic effect without Landau levels

In chapter 3 we introduce a variant of the chiral magnetic effect in a weak oscillating magnetic field, that does not rely on the presence of Landau levels. For this, we consider a Weyl semimetal with both, broken time- and broken inversion symmetry. We have found that in this case the topological response is carried by the surface states. This is unexpected, because one would expect a surface current to scale with the circumference, rather than the cross section. The reason for the unusual scaling of the response is that the chiral surface states encircle the entire flux (see Fig. 1.6 a), and therefore have a magnetic moment that scales with the diameter W.

In fact, there is a deep connection between the two manifestations of the chiral magnetic effect: If one slowly turns on a strong magnetic field, the surface bands are shifted in energy and merge near the Weyl points into the zeroth Landau level (Fig. 1.6 b). Therefore, the states that carry the chiral magnetic effect in the conventional CME and our variant are directly related.

1.4 Interfaces with superconductors

1.4.1 Andreev scattering

In a superconductor, excitations consist of unpaired electrons (filled states above the Fermi level) or holes (empty states below the Fermi level). These excitations can be described in a mean-field approximation as moving in a background pair potential, which is formed by the condensate of Cooper pairs. Electrons can be scattered into holes by the pair potential, a process known as Andreev scattering [56, 57]. When an electron is converted into a hole, a Cooper pair is formed, which accounts for the missing $2e$ charge (see Fig. 1.7).
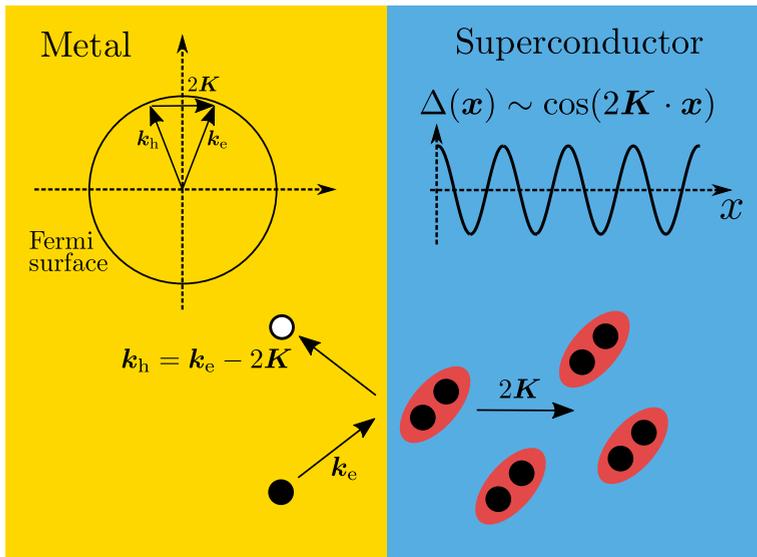
Figure 1.7: Schematic drawing of Andreev-Bragg scattering in a metal-superconductor junction. Bottom: Sketch of the Andreev scattering process. An electron enters the superconductor, where it forms a Cooper pair together with another electron. As a result, a hole is scattered back into the metal. Top left: Schematic drawing of the Brillouin zone of the metal. If the wave vector of the PDW connects two points of the Fermi surface, Andreev-Bragg scattering is allowed. Right: Drawing of the spatial dependence of the order parameter as a function of position.

Andreev scattering has a series of surprising features, that are discussed in more detail for example in [58, 59]. Most remarkably, it explains why there is a finite conductance from a metal into a superconductor at the Fermi energy, despite the excitation gap in the superconductor: An incoming electron is not simply transmitted into the superconductor, but gets Andreev reflected into a hole, transferring a charge of $2e$ from the metal into the superconductor. Therefore, the conductance from a normal metal into a superconductor (assuming an ideal interface) is twice the normal-state conductance. If the interface is not ideal, described for example by a finite transmission probability T, the conductance drops quadratically $\propto T^2$. This quadratic dependence derives from the two particle nature of Andreev scattering.

The conversion of an electron into a hole by Andreev scattering at

a metal-superconductor interface introduces a phase coherence between electrons and holes in the metal. This coherence extends the properties of the superconductor into the metal. Most notably, the local density of states near the interface is suppressed around the Fermi energy. One speaks of *proximity effect* and *induced superconductivity*. The relationship between Andreev scattering and the proximity effect has been reviewed in detail in [60]. In a ballistic system, the length scale on which superconductivity is induced into the metal is the electron-hole coherence length in the metal. It is often much longer than the coherence length in the superconductor, which characterizes the "size" of Cooper pairs. This coherence is, however, rapidly destroyed if the metal breaks time-reversal symmetry. There also exists an inverse proximity effect: The pair-breaking scattering in the metal reduces the pairing amplitude in the superconductor near the interface [61].

1.4.2 Andreev-Bragg scattering

In a conventional superconductor, Cooper pairs carry zero net momentum. Therefore, momentum conservation dictates that an Andreev-reflected hole carries the same momentum as the incoming electron. Since the mass of a hole is the negative equal of the electron, in an ideal and time-reversal symmetric setting, the hole is reflected into the direction where the electron came from: $\boldsymbol{v}_h = \boldsymbol{k}_e/(-m_e) = -\boldsymbol{v}_e$. Its reflection angle is the opposite of that of a billiard ball bouncing from a hard wall (so-called retroreflection).

There exist also unconventional superconductors [62–65], where the Cooper pairs may carry a finite net momentum. From a theoretical perspective, the FFLO phase [66, 67] has received a lot of attention. The order parameter of such a superconductor varies periodically in space $\Delta_{2\boldsymbol{K}}(\boldsymbol{x}) \sim \cos(2\boldsymbol{K} \cdot \boldsymbol{x})$.

The interest in these so-called pair density waves has recently been revived, when it was suggested that they might play a role in the pseudogap phase of cuprate superconductors [68]. If an electron Andreev scatters from a pair density wave, the momentum of the outgoing hole is shifted: $\boldsymbol{k}_h = \boldsymbol{k}_e - 2\boldsymbol{K}$. If we take multiple Andreev scattering processes into account, we see that electrons, that are reflected as electrons, are shifted by even multiples of the Cooper pair momentum $\boldsymbol{k}'_e = \boldsymbol{k}_e - 2n \cdot 2\boldsymbol{K}$. If on the other hand an electron is scattered into a hole, the momentum is shifted by an odd multiple $\boldsymbol{k}_h = \boldsymbol{k}_e - (2n + 1) \cdot 2\boldsymbol{K}$. In a sense, the Cooper pairs act very much like a crystal lattice, absorbing and emitting quantized momenta.

Following this analogy, we call this type of scattering Andreev-Bragg

scattering. In general, the scattering angle in position space is determined by which points of the Fermi surface of the non-interacting system are connected by multiples of the Cooper pair momentum. In extreme cases, the scattering angle can be the opposite of conventional Andreev reflection.

1.4.3 Proximity effect in Weyl semimetals

In Weyl semimetals, the proximity effect is fundamentally different for those with and those without time-reversal symmetry. In the time-reversal symmetric case, the proximity to a spin singlet *s*-wave superconductor will gap the Weyl cones [69]. In Weyl semimetals with broken time-reversal symmetry, on the other hand, the proximity effect is suppressed and only affects the states that are localized at the interface between the Weyl semimetal and the superconductor. The reason is that a conventional superconductor pairs electrons from $+\boldsymbol{k}$ with electrons from $-\boldsymbol{k}$, hence from different Weyl cones. In a time-reversal symmetric Weyl semimetal, these Weyl cones have the same chirality due to Kramers degeneracy. In a Weyl semimetal with broken time-reversal symmetry, however, the cones have opposite chirality. In order for a superconductor to induce a gap, it would have to flip the chirality, which conventional spin singlet *s*-wave superconductors do not do.

At the interface, the situation is different. The interface states live both in the Weyl semimetal and in the superconductor. In the Weyl semimetal, they are localized by the time-reversal breaking magnetization, in the superconductor by the coherence length. Their orbital structure is therefore a hybrid of the orbital structure in the Weyl semimetal and the orbital structure in the superconductor. An interesting feature of these interface states is that the pairing is between electrons from the same band. This band splits into two, nearly charge neutral bands, which are called Majorana bands [69–71].

1.5 This thesis

In this section, we give a brief outline of the topics discussed in the chapters of this thesis.

Chapter 2

Topological insulators are classified based on their symmetries. The celebrated "ten-fold way" [28] considers time-reversal, particle-hole, and chiral

symmetry. (There also exist topological insulators that do not fall into these categories.) In this chapter, we study a layered system with anti-ferromagnetic order, a so-called anti-ferromagnetic topological insulator [72]. In this system, time-reversal symmetry is broken locally, but restored in conjunction with a translation by half a unit cell. Unlike true time-reversal symmetry, this effective time-reversal symmetry is destroyed by weak disorder. However, in our studies, we find a remarkable robustness of the topological phase against electrostatic disorder. The reason is that the symmetry still holds *on average*, placing the antiferromagnetic topological insulator in the class of statistical topological insulators [73, 74].

Weyl semimetals make their first appearance in this chapter, but not yet as a stable phase — they require fine tuning of parameters. Nevertheless, we are be able to calculate the conductance and the Fano factor (ratio of shot noise power and average current) at the Weyl point. Our key finding is that the Fano factor is distinct from the 1/3 value in graphene.

Chapter 3

The chiral magnetic effect (CME) is a unique experimental signature of a Weyl semimetal that does not exist in graphene. It has been studied extensively as a response of a Weyl semimetal in a strong magnetic field to a slowly oscillating inversion breaking perturbation. However, such a perturbation is difficult to achieve experimentally. In this chapter, we study the complementary response of a Weyl semimetal with broken inversion symmetry to a small oscillating magnetic field. We find that, in this case, the CME has a surface contribution from the Fermi arc that scales with sample size in the same way as the bulk contribution. While the bulk contribution is not universal, and susceptible to disorder, we argue that the surface contribution is robust and universal, demonstrating its topological origin.

The CME from the surface Fermi arcs persists in the limit of an infinitesimally small magnetic field, when no Landau levels are formed. This "chiral magnetic effect without Landau levels" is reminiscent of the "quantum Hall effect without Landau levels".

Chapter 4

The surface states of a Weyl semimetal with broken time-reversal and inversion symmetry form a chiral solenoid in *real space* (see Fig. 1.3). In the previous chapter 3 we showed that this solenoid carries the topological response to an oscillating magnetic field. In this chapter, we investigate

what happens if we coat the solenoid with a superconductor. We find that the proximity effect is short-ranged, affecting only the states localized at the Weyl semimetal – superconductor interface. There, the proximity effect splits the surface mode into a pair of Majorana modes. We derive an effective surface Hamiltonian and show how such a system can be used to trap Majorana fermions.

Chapter 5

In the final chapter, we depart from Weyl semimetals to study another type of system that has Fermi arcs. Spectroscopy of the pseudo-gap phase in high T_c-cuprates has revealed such disconnected pieces of Fermi surface. Even though these materials have been studied for several decades, there is no consensus about the microscopic mechanism behind the pseudo-gap phase. Recently, Patrick Lee proposed that an extreme form of finite-momentum Cooper pairing, a so-called pair density wave, might be the solution to this ongoing puzzle [68]. The pairing is called Amperian, because it is similar to the attractive force from Ampère's law that appears between two parallel currents.

We show that Amperian pairing would lead to specular Andreev reflection (rather than the usual retroreflection) and we propose a simple three-terminal setup to detect it.

2 Quantum phase transitions of a disordered antiferromagnetic topological insulator

2.1 Introduction

Topological insulators (TI) have an insulating bulk and a conducting surface, protected by time-reversal symmetry [75, 76]. In three-dimensional (3D) lattices the concept can be extended to include magnetic order [72, 77–80]: Antiferromagnetic topological insulators (AFTI) break time-reversal symmetry locally, but recover it in combination with a lattice translation. Layered structures with a staggered magnetization provide the simplest example of an AFTI [72]: The quantum anomalous Hall effect in a single layer produces edge states with a chirality that changes from one layer to the next. Interlayer coupling gives these counterpropagating edge states an anisotropic dispersion, similar to the unpaired Dirac cone on the surface of a time-reversally invariant TI — but now appearing only on surfaces perpendicular to the layers.

While the first AFTI awaits experimental discovery, it is clear that disorder will play a essential role in any realistic material. Electrostatic disorder breaks translational symmetry, and therefore indirectly breaks the effective time-reversal symmetry of the AFTI. The topological protection of the conducting surface is expected to persist, at least for a range of disorder strengths, because the symmetry is restored on long length scales. A disordered AFTI belongs to the class of statistical topological insulators, protected by a symmetry that holds on average [73, 74].

Here we explore these unusual disorder effects both analytically and numerically, for a simple model of a layered AFTI. We find that, while sufficiently strong disorder suppresses both bulk and surface conduction, intermediate disorder strengths may actually favor conductivity. Over a broad range of magnetizations the electrostatic disorder drives the insulating bulk into a metallic phase, via an Anderson metal-insulator transition. Disorder may also produce a topological phase transition, enabling surface conduction while keeping the bulk insulating — as a magnetic analogue of the "topological Anderson insulator" [81–84]. Each of these quantum phase transitions is identified via the scaling of the conductance with system size.

The outline of the chapter is as follows. In the next section we construct a simple model of an antiferromagnetically ordered stack, starting from the Qi-Wu-Zhang Hamiltonian [85] for the quantum anomalous Hall effect in a single layer, and alternating the sign of the magnetization from one layer to the next. We identify the effective time-reversal symmetry of Mong, Essin, and Moore [72], locate the 2D Dirac cones of surface states and the 3D Weyl cones of bulk states, and calculate their contributions to the electrical conductance. All of this is for a clean system. Disorder is added in Secs. 2.3 and 2.4, where we study the quantum phase transitions between the AFTI phase and the metallic or topologically trivial insulating phases. The phase boundaries are calculated analytically using the self-consistent Born approximation, following the approach of Ref. [82], and numerically from the scaling of the conductance with system size in a tight-binding discretization of the AFTI Hamiltonian. We conclude in Sec. 2.5.

2.2 Clean limit

2.2.1 Model Hamiltonian

There exists a broad class of 3D magnetic textures that produce an AFTI [72, 78, 79]. Here we consider a particularly simple example of antiferromagnetically ordered layers, see Fig. 2.1, but we expect the generic features of the phase diagram to be representative of the entire class of AFTI.

For a single layer we take the Qi-Wu-Zhang Hamiltonian of the quantum anomalous Hall effect [85],

$$
\begin{aligned}
H_{\pm}(k_x, k_y) = {}&\pm \sigma_z(\mu - \cos k_x - \cos k_y) \\
&+ \sigma_x \sin k_x + \sigma_y \sin k_y.
\end{aligned}
\tag{2.1}
$$
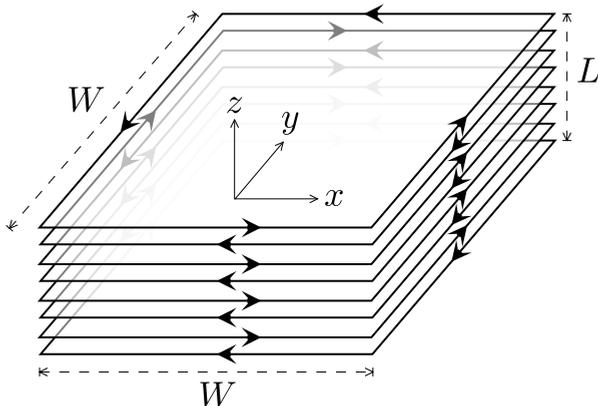
Figure 2.1: Stack of antiferromagnetically ordered layers. Each layer is insulating in the interior but supports a chiral edge state (arrows) because of the quantum anomalous Hall effect. Interlayer hopping (in the z-direction) produces an anisotropic Dirac cone of surface states on surfaces perpendicular to the layers. The unpaired Dirac cone is robust against disorder, as in a (strong) topological insulator, although time-reversal symmetry is broken locally.

This is a tight-binding Hamiltonian on a square lattice in the x-y plane, with two spin bands (Pauli matrices $\boldsymbol{\sigma}$, unit matrix σ_0) coupled to the wave vector $\boldsymbol{k}$. The lattice constant and the nearest-neighbor hopping energies are set equal to unity, so that both the wave vector $\boldsymbol{k}$ and the magnetic moment μ are dimensionless. Time-reversal symmetry maps H_+ onto H_-,

$$\sigma_y H_\pm^*(-\boldsymbol{k})\sigma_y = H_\mp(\boldsymbol{k}). \tag{2.2}$$

The topological quantum number (Chern number) $\mathcal{C}_\pm$ of the quantum anomalous Hall Hamiltonian $H_\pm$ is [85]

$$\mathcal{C}_\pm = \begin{cases} \pm\operatorname{sign}\mu & \text{if } |\mu| < 2, \\ 0 & \text{if } |\mu| > 2. \end{cases} \tag{2.3}$$

A change in $\mathcal{C}_\pm$ is accompanied by a closing of the excitation gap at $\mu = -2, 0, 2$.

The quantum anomalous Hall layers can be stacked in the z-direction with ferromagnetic order (same Chern number in each layer, see Ref. [17]) or with antiferromagnetic order (opposite Chern number in adjacent layers). Ferromagnetic order breaks time-reversal symmetry globally, producing a 3D analogue of the quantum Hall effect with chiral surface states [86, 87].

To obtain an effective time-reversal symmetry and produce a surface Dirac cone we take an antiferromagnetic magnetization.

The Hamiltonian is constructed as follows. Because of the staggered magnetization, the unit cell extends over two adjacent layers, distinguished by a pseudospin degree of freedom τ. The corresponding Brillouin zone is $|k_x| < \pi$, $|k_y| < \pi$, $|k_z| < \pi/2$, half as small in the z-direction because of the doubled unit cell. Interlayer coupling by nearest-neigbor hopping (with strength t_z) is described by the Hamiltonian

$$H_z(k_z) = t_z \begin{pmatrix} 0 & \rho^\dagger e^{2ik_z} + \rho \\ \rho e^{-2ik_z} + \rho^\dagger & 0 \end{pmatrix}, \tag{2.4}$$

with a 2×2 matrix ρ acting on the spin degree of freedom. The term $\rho^\dagger e^{2ik_z}$ moves up one layer in the next unit cell, while the term ρ moves down one layer in the same unit cell. We require that the interlayer Hamiltonian preserves time-reversal symmetry,

$$\sigma_y H_z^*(-k_z)\sigma_y = H_z(k_z) \Rightarrow \sigma_y \rho^* \sigma_y = \rho. \tag{2.5}$$

This still leaves some freedom in the choice of ρ, we take $\rho = i\sigma_z$.

The staggered magnetization is described by combining H_+ in one layer with H_- in the next layer, so by replacing σ_z with $\tau_z \otimes \sigma_z$ in Eq. (2.1). [The Pauli matrices $\boldsymbol{\tau}$ (unit matrix τ_0) act on the layer degree of freedom.] The full Hamiltonian of the stack takes the form

$$H_{\text{AFTI}}(\boldsymbol{k}) = H_z(k_z) + (\tau_z \otimes \sigma_z)(\mu - \cos k_x - \cos k_y)$$
$$+ \tau_0 \otimes (\sigma_x \sin k_x + \sigma_y \sin k_y), \tag{2.6}$$
$$H_z(k_z) = t_z(\tau_y \otimes \sigma_z)(\cos 2k_z - 1) + t_z(\tau_x \otimes \sigma_z)\sin 2k_z. \tag{2.7}$$

2.2.2 Effective time-reversal symmetry

Following Mong, Essin, and Moore [72], we construct an effective time-reversal symmetry operator,

$$\mathcal{S}(k_z) = \Theta\mathcal{T}(k_z) = \mathcal{T}(k_z)\Theta, \tag{2.8}$$

by combining the fundamental time-reversal operation Θ with a translation $\mathcal{T}(k_z)$ over half a unit cell in the z-direction. The translation operator is represented by a 2×2 matrix acting on the layer degree of freedom,

$$\mathcal{T}(k_z) = \begin{pmatrix} 0 & e^{2ik_z} \\ 1 & 0 \end{pmatrix} = e^{ik_z}(\tau_x \cos k_z - \tau_y \sin k_z). \tag{2.9}$$

Both off-diagonal matrix elements switch the layers, either remaining in the same unit cell or moving to the next unit cell. One verifies that the square $\mathcal{T}^2(k_z) = e^{2ik_z}\tau_0$ represents the Bloch phase acquired by a shift over the full unit cell (two layers).

The interlayer Hamiltonian (2.4) commutes with the translation over half a unit cell,

$$\mathcal{T}(k_z)H_z(k_z) = H_z(k_z)\mathcal{T}(k_z). \tag{2.10}$$

Since we have also assumed that H_z preserves time-reversal symmetry, $\Theta H_z(k_z) = H_z(k_z)\Theta$, it commutes with the combined operation,

$$\mathcal{S}(k_z)H_z(k_z) = H_z(k_z)\mathcal{S}(k_z). \tag{2.11}$$

The full Hamiltonian,

$$H_{\text{AFTI}}(\boldsymbol{k}) = H_z(k_z) + \begin{pmatrix} H_+(k_x, k_y) & 0 \\ 0 & H_-(k_x, k_y) \end{pmatrix}, \tag{2.12}$$

then also commutes with $\mathcal{S}(k_z)$, because

$$\Theta H_+(k_x, k_y) = H_-(k_x, k_y)\Theta. \tag{2.13}$$

For the quantum anomalous Hall layers the fundamental time-reversal operation is

$$\Theta = i\sigma_y\mathcal{K}, \tag{2.14}$$

where $\mathcal{K}$ takes the complex conjugate and inverts the momenta, $\mathcal{K}f(\boldsymbol{k}) = f^*(-\boldsymbol{k})$. [One verifies that the identity (2.13) is equivalent to Eq. (2.2).] The effective time-reversal symmetry operation is then given explicitly by

$$\mathcal{S}(k_z) = i\sigma_y \otimes (\tau_x \cos k_z - \tau_y \sin k_z)\mathcal{K}, \tag{2.15}$$

up to an irrelevant phase factor e^{ik_z}.

The fundamental time-reversal operation (2.14) squares to -1, as it should do for a spin-$\frac{1}{2}$ degree of freedom. As noted by Liu [79], one can equally well start from a spinless time-reversal symmetry that squares to $+1$, for example, taking $\Theta = \mathcal{K}$. Since $\mathcal{S}^2(k_z) = e^{2ik_z}\Theta^2$, the choice of $\Theta^2 = \pm 1$ amounts to shift of k_z by $\pi/2$. Gapless surface states appear at the k_z-value for which $\mathcal{S}$ squares to -1, so at the center of the surface Brillouin zone ($k_z = 0$) for $\Theta^2 = -1$ and at the edge ($k_z = \pi/2$) for $\Theta^2 = 1$.
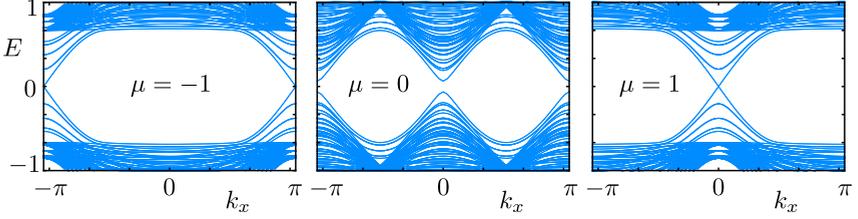
Figure 2.2: Energy spectrum of the AFTI Hamiltonian (2.6), with $t_z = 0.4$, for a stack of 16 layers in the z-direction with periodic boundary conditions. The layers are infinitely wide in the x-direction and truncated at 16 lattice sites in the y-direction. At $\mu = \pm 1$ the system is in the AFTI phase, with a nondegenerate Dirac cone of surface states centered at the edge of the Brillouin zone $(-2 < \mu < 0)$ or at the center of the Brillouin zone $(0 < \mu < 2)$. At $\mu = 0$ the bulk gap closes at a pair of twofold degenerate Weyl cones, one at the center and one at the edge of the Brillouin zone. In this plot a finite gap remains for $\mu = 0$, because of the confinement in the y-direction.

2.2.3 Bulk and surface states

The bulk spectrum $E(\boldsymbol{k})$ of the Hamiltonian (2.6) can be easily calculated by noting that $H^2_{\mathrm{AFTI}}(\boldsymbol{k})$ reduces to a unit matrix in σ, τ space, hence

$$E^2(\boldsymbol{k}) = (\mu - \cos k_x - \cos k_y)^2 + \sin^2 k_x + \sin^2 k_y$$
$$+ (2t_z \sin k_z)^2. \tag{2.16}$$

The gap closes with a 3D conical dispersion (Weyl cone) at $(k_x, k_y, k_z) = (0, 0, 0)$ for $\mu = 2$, at $(\pi, \pi, 0)$ for $\mu = -2$, and at the two points $(0, \pi, 0)$, $(\pi, 0, 0)$ for $\mu = 0$. Each cone is twofold degenerate and has the anisotropic dispersion

$$E^2_{\mathrm{Weyl}}(\delta\boldsymbol{k}) = (\delta k_x)^2 + (\delta k_y)^2 + 4t_z^2(\delta k_z)^2, \tag{2.17}$$

with $\delta\boldsymbol{k}$ the wave vector measured from the conical point (Weyl point). Unlike in the case of ferromagnetic order [11, 17], the bulk spectrum is only gapless at specific values of $\mu \in \{0, \pm 2\}$ — there is no Weyl semimetal phase in this model.

The surface spectrum of the antiferromagnetically ordered stack is gapless in the interval $0 < |\mu| < 2$, if finite-size effects are avoided by taking periodic boundary conditions in the z-direction. The surface states

have an anisotropic 2D conical dispersion (Dirac cone),

$$E_{\text{Dirac}}^2(q, k_z) = (q - q_0)^2 + 4t_z^2 k_z^2,$$
$$q_0 = \begin{cases} 0 & \text{if } 0 < \mu < 2, \\ \pi & \text{if } -2 < \mu < 0, \end{cases} \tag{2.18}$$

with $q = k_x$ on the x-z plane and $q = k_y$ on the y-z plane.

These AFTI surface states emerge from the counterpropagating chiral edge states at $k_z = 0$ and are protected by the effective time-reversal symmetry (2.15). They are reminiscent of the surface states in a weak topological insulator, formed by stacking quantum spin Hall layers with helical edge states. The essential difference is that in a weak TI there is a second Dirac cone at $k_z = \pi$, while the AFTI has only a single Dirac cone. (The "fermion doubling" is avoided by the restriction of the Brillouin zone to $|k_z| < \pi/2$.)

Notice that the closing of the gap at $\mu = 0$ is not accompanied by a change in the number of surface Dirac cones. Instead, the single Dirac cone switches from the center to the edge of the surface Brillouin zone when μ crosses zero. (See Fig. 2.2.) This is a quantum phase transition in the sense of Ref. [88], between band insulators with the same topological quantum number but distinguished by the location of the surface Dirac cone.

2.2.4 Surface conductance from the Dirac cone

To study the transport properties of the AFTI, we take layers in the x-y plane of width $W \times W$, stacked in the z-direction over a length L. The top and bottom layers are connected to electron reservoirs at voltage difference V, and the current I in the z-direction then determines the conductance $G = \lim_{V \to 0} I/V$ perpendicular to the layers. We fix the Fermi level $E_F = 0$ at the middle of the bulk gap, where the conductance is minimal.

In the AFTI phase, for $0 < |\mu| < 2$, the conductance is dominated by the surface states. Analogously to graphene [89, 90], each 2D Dirac cone contributes a conductance $(e^2/\pi h)(W/L_{\text{eff}})$, at the Dirac point ($E_F = 0$) and for $W \gg L_{\text{eff}} \equiv L/2t_z$. There are four Dirac cones (one on each surface perpendicular to the layers), totaling

$$G_{\text{Dirac}} = \frac{8e^2}{\pi h} \frac{t_z W}{L}. \tag{2.19}$$
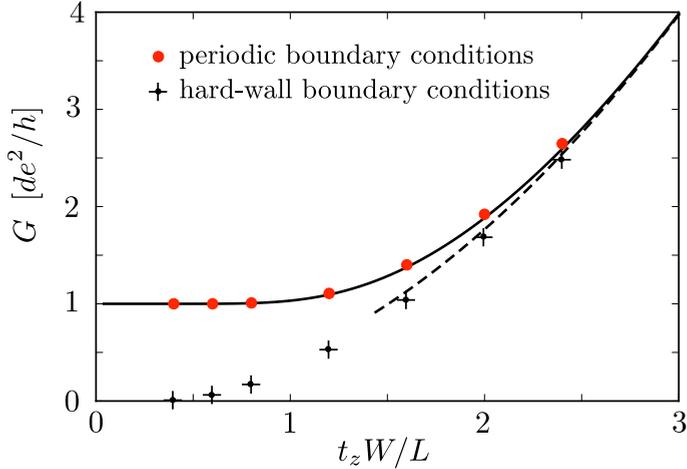
Figure 2.3: Conductance at the Weyl point for periodic boundary conditions, according to Eq. (2.20) (solid curve) and the asymptotic form for large aspect ratio (2.22) (dashed). The data points are calculated from the AFTI Hamiltonian (2.6), at $\mu = 2$, $t_z = 0.4$, for a lattice of 8 layers in the z-direction, with periodic boundary conditions in the x and y-directions (red dots) and for hard-wall boundary conditions (black crosses).

2.2.5 Bulk conductance from the Weyl cone

When the bulk gap closes, at $\mu = 0, \pm 2$, the 3D Weyl cones contribute an amount of order $(W/L_{\text{eff}})^2$ to the conductance, which dominates over the surface conductance when $W \gg L_{\text{eff}}$. A similar calculation as in Ref. [91] gives the minimal conductance at the Weyl point ($E_F = 0$),

$$G_{\text{Weyl}} = d\,\frac{e^2}{h} \sum_{n,m=-\infty}^{\infty} T_{nm}, \tag{2.20}$$

$$T_{nm} = \cosh^{-2}\left[2\pi(L_{\text{eff}}/W)\sqrt{n^2 + m^2}\right], \tag{2.21}$$

for periodic boundary conditions in the x and y-directions. Four Weyl cones contribute at $\mu = 0$ (degeneracy factor $d = 4$) and two Weyl cones contribute at $\mu = \pm 2$ (degeneracy factor $d = 2$).

The dependence of G_{Weyl} on the aspect ratio W/L_{eff} is plotted in Fig. 2.3. For $W \gg L_{\text{eff}}$ one has the asymptotic result

$$G_{\text{Weyl}} = d\,\frac{e^2}{h}\frac{2\ln 2}{\pi}\left(\frac{t_z W}{L}\right)^2. \tag{2.22}$$

26
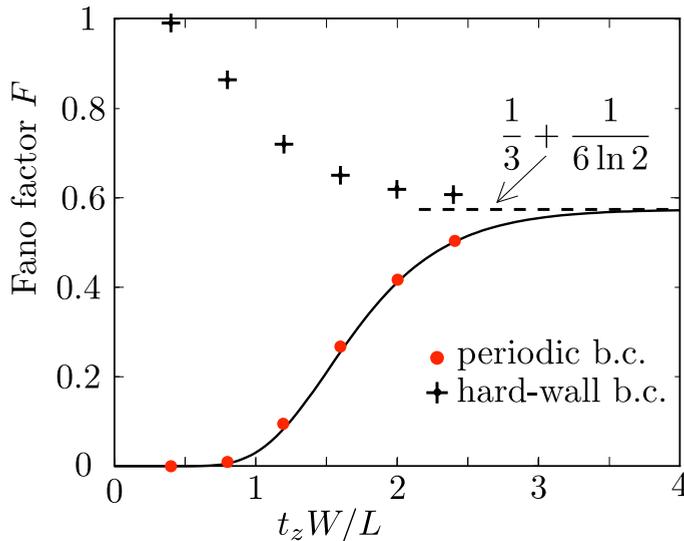
Figure 2.4: Same as Fig. 2.3, but for the Fano factor at the Weyl point.

The conduction at the Weyl point is not "pseudo-diffusive", as it is at the Dirac point of graphene, because the conductivity $\sigma_{\mathrm{Weyl}} = G_{\mathrm{Weyl}} L/W^2$ is not scale invariant. The Fano factor F_{Weyl} (ratio of shot noise power and average current) at the Weyl point is scale invariant, but it differs from the value $F = 1/3$ characteristic of pseudo-diffusive conduction [91]. We find

$$F_{\mathrm{Weyl}} = \frac{\sum_{n,m=-\infty}^{\infty} T_{nm}(1 - T_{nm})}{\sum_{n,m=-\infty}^{\infty} T_{nm}}$$
$$= \frac{1}{3} + (6\ln 2)^{-1} \approx 0.574 \ \text{ for } \ W \gg L_{\mathrm{eff}}. \qquad (2.23)$$

The aspect ratio dependence of F_{Weyl} is plotted in Fig. 2.4.

2.3 Phase diagram of the disordered system

We add disorder to the AFTI Hamiltonian (2.6) in the form of a spin-independent random potential chosen independently on each lattice site from a Gaussian distribution of zero mean and variance δU^2. In σ, τ

representation the disorder Hamiltonian is given by

$$H_{\text{disorder}} = \sum_i \left[(\tau_0 \otimes \sigma_0)U_i^{(1)} + (\tau_z \otimes \sigma_0)U_i^{(2)} \right], \tag{2.24}$$

$$\langle U_i^{(n)} \rangle = 0, \quad \langle U_i^{(n)} U_{i'}^{(n')} \rangle = \tfrac{1}{2} \delta U^2 \delta_{ii'} \delta_{nn'}. \tag{2.25}$$

The sum over i runs over bilayer unit cells and $\langle \cdots \rangle$ denotes the disorder average.

Different layers see a different random potential, so the effective time-reversal symmetry of Sec. 2.2.2 is broken locally by the disorder — but restored on long length scales. We expect the effect of a random potential on the AFTI to be equivalent to the effect of a random magnetic field on a strong TI [74, 92]: The surface remains conducting while the bulk remains insulating, separated from the trivial insulator by a topological phase transition.

In this section we explore the phase diagram of the disordered AFTI, first analytically using the self-consistent Born approximation (SCBA) and then numerically by calculating the conductance.

We calculate the disorder-averaged density of states from the self-energy Σ, defined by

$$\overline{\frac{1}{E_F + i0^+ - H_{\text{AFTI}} - \Sigma}}$$
$$= \left\langle \frac{1}{E_F + i0^+ - H_{\text{AFTI}} - H_{\text{disorder}}} \right\rangle. \tag{2.26}$$

We set the Fermi level at $E_F = 0$, in the middle of the gap of the clean system. The SCBA self-energy, for a disorder potential of the form (2.24), is given by the equation

$$\Sigma = \tfrac{1}{2} \delta U^2 \sum_{\boldsymbol{k}} \Bigg([i0^+ - H_{\text{AFTI}}(\boldsymbol{k}) - \Sigma]^{-1}$$
$$+ \tau_z [i0^+ - H_{\text{AFTI}}(\boldsymbol{k}) - \Sigma]^{-1} \tau_z \Bigg). \tag{2.27}$$

The sum over $\boldsymbol{k}$ ranges over the first Brillouin zone, in the continuum limit

$$\sum_{\boldsymbol{k}} \mapsto \frac{1}{4\pi^3} \int_{-\pi}^{\pi} dk_x \int_{-\pi}^{\pi} dk_y \int_{-\pi/2}^{\pi/2} dk_z. \tag{2.28}$$

The SCBA self-energy is a $\boldsymbol{k}$-independent 4×4 matrix in the spin and layer degrees of freedom,

$$\Sigma = (\tau_z \otimes \sigma_z)\delta\mu - (\tau_0 \otimes \sigma_0)i\gamma. \tag{2.29}$$

The term $\delta\mu$ renormalizes the magnetic moment μ and thus accounts for a disorder-induced shift of the phase boundary of the topologically nontrivial band insulator. The term γ produces a density of states $\pi^{-1}\text{Im}\,(H_{\text{AFTI}} + \Sigma)^{-1}$, induced by the disorder within the gap of the clean system. A nonzero γ may indicate a metallic phase or a topologically trivial Anderson insulator (the density of states cannot distinguish between the two).

Substitution of Eq. (2.29) into Eq. (2.27), and use of the identity

$$
\begin{aligned}
H_{\text{AFTI}}(k_x, k_y, k_z) &+ \tau_z H_{\text{AFTI}}(-k_x, -k_y, k_z)\tau_z \\
&= 2(\tau_z \otimes \sigma_z)(\mu - \cos k_x - \cos k_y),
\end{aligned} \tag{2.30}
$$

produces two coupled equations for γ and $\delta\mu$:

$$
\gamma = \delta U^2 \sum_{\boldsymbol{k}} \frac{\gamma + 0^+}{\gamma^2 + E_{\mu+\delta\mu}^2(\boldsymbol{k})}, \tag{2.31a}
$$

$$
\delta\mu = -\delta U^2 \sum_{\boldsymbol{k}} \frac{M_{\mu+\delta\mu}(\boldsymbol{k})}{\gamma^2 + E_{\mu+\delta\mu}^2(\boldsymbol{k})}, \tag{2.31b}
$$

with the definitions

$$
E_\mu^2(\boldsymbol{k}) = M_\mu^2(\boldsymbol{k}) + \sin^2 k_x + \sin^2 k_y + 4t_z^2 \sin^2 k_z, \tag{2.32a}
$$

$$
M_\mu(\boldsymbol{k}) = \mu - \cos k_x - \cos k_y. \tag{2.32b}
$$

The phase boundary at $\mu = 0$ remains unaffected by disorder, because

$$
\sum_{\boldsymbol{k}} \frac{M_0(\boldsymbol{k})}{E_0^2(\boldsymbol{k})} = 0, \tag{2.33}
$$

so $\gamma = 0 = \delta\mu$ solves the SCBA equations for $\mu = 0$. The phase boundaries at $\mu = \pm 2$ do shift when we switch on the disorder. If we seek a solution of Eq. (2.31) with $\gamma = 0$, $\delta\mu = \pm 2 - \mu_\pm$ we obtain the phase boundaries at

$$
\mu_\pm = \pm 2 + \delta U^2 \sum_{\boldsymbol{k}} \frac{M_{\pm 2}(\boldsymbol{k})}{E_{\pm 2}^2(\boldsymbol{k})}. \tag{2.34}
$$

These phase boundaries between band insulators are plotted in Fig. 2.5 (dashed curves), at the value $t_z = 0.4$ for which $\mu_\pm = \pm 2 \pm 0.345\,\delta U^2$.

The outward curvature of the phase boundaries implies that the addition of disorder to a topologically trivial insulator can convert it into a nontrivial insulator, or in other words, that disorder can produce metallic conduction on surfaces perpendicular to the layers — analogous to a topological Anderson insulator [81–84].
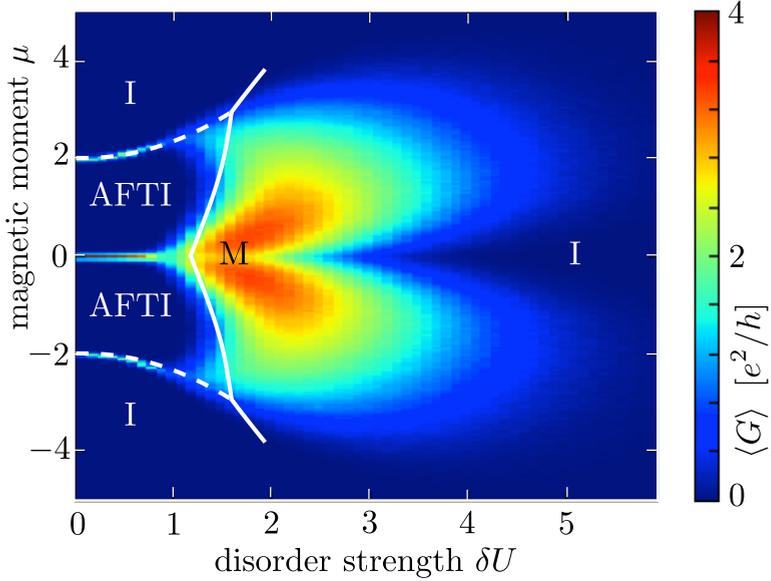
Figure 2.5: Color-scale plot of the conductance of a disordered AFTI, calculated numerically from the Hamiltonian (2.6) for current flowing perpendicular to a stack of 20 layers. Each layer has dimensions 20×20 with periodic boundary conditions, the interlayer coupling is $t_z = 0.4$. The topological insulator phase (AFTI), the trivial insulator phase (I), and the metallic phase (M) are indicated in the plot. The white curves are the phase boundaries resulting from the self-consistent Born approximation (SCBA). The Anderson transition between a metal and a trivial insulator is not captured by the SCBA.

For sufficiently large $\delta U > \delta U_c$, the SCBA equations may support a solution with nonzero γ. The dependence of δU_c on μ follows from the solution of Eq. (2.31) for infinitesimal $\gamma \neq 0$,

$$\delta U_c^2 = \left[\sum_{\boldsymbol{k}} \frac{1}{E_x^2(\boldsymbol{k})} \right]^{-1} , \quad \mu = x + \delta U_c^2 \sum_{\boldsymbol{k}} \frac{M_x(\boldsymbol{k})}{E_x^2(\boldsymbol{k})}. \qquad (2.35)$$

By varying $x \equiv \mu + \delta\mu$ we obtain the phase boundary $\delta U_c(\mu)$ plotted in Fig. 2.5 (solid curve), separating the band insulator from a metallic phase (or possibly an Anderson insulator with a finite density of states in the band gap).

At $x = \pm 2$ we reach a tricritical point, where the metal meets two topologically distinct insulating phases. For $t_z = 0.4$ these tricritical

points occur at $\mu = \pm 2.940$, $\delta U_c = 1.654$.

We have tested the SCBA by calculating the conductance from the AFTI Hamiltonian (2.6), discretized on a cubic lattice of dimensions $W \times W \times L = 20 \times 20 \times 20$. (These numerical calculations were performed using the Kwant code [93].) We impose periodic boundary conditions in the x and y-directions and connect the layers at $z = 0$ and $z = L$ to W^2 one-dimensional chains, as a model of a heavily doped electron reservoir. The interlayer coupling is fixed at $t_z = 0.4$. The conductance, averaged over a few hundred disorder realizations, is shown as a color-scale plot in Fig. 2.5.

As expected, the SCBA cannot describe the phase boundary between the trivial insulator and the metal, since it cannot distinguish between insulating and extended states in the bulk gap. For the other phase boundaries, between the topologically trivial and nontrivial insulators (dashed) as well as between the nontrivial insulator and the metal (solid), the SCBA is found to be in good agreement with the conductance calculations.

2.4 Finite-size scaling

The conductance in the phase diagram of Fig. 2.5 is given for a single size of the conductor. To establish the metallic or insulating character of a phase it is necessary to compare different system sizes. A phase transition is then identified by a scale invariant "critical" conductance.

Such finite-size scaling plots are shown in Fig. 2.6. Panel a shows the transition from a metal to an insulator with increasing disorder, while panel b shows the reverse transition. Panel c shows the transition between a topologically trivial and nontrivial insulator. The critical point of each transition is indicated by an arrow.

The finite-size scaling on the line $\mu = 0$ is shown in Fig. 2.7. For weak disorder the conductance tends to saturate with increasing system size at the clean limit (2.20), which for $d = 4$, $t_z = 0.4$, and $W = L$ is close to $G_{\text{Weyl}} = 4e^2/h$. For strong disorder the conductance shows the metallic scaling $\propto W^2/L = L$, but only after an intermediate regime where the conductance decreases with increasing system size — suggestive of an insulating regime. We will discuss the implications in the next section.
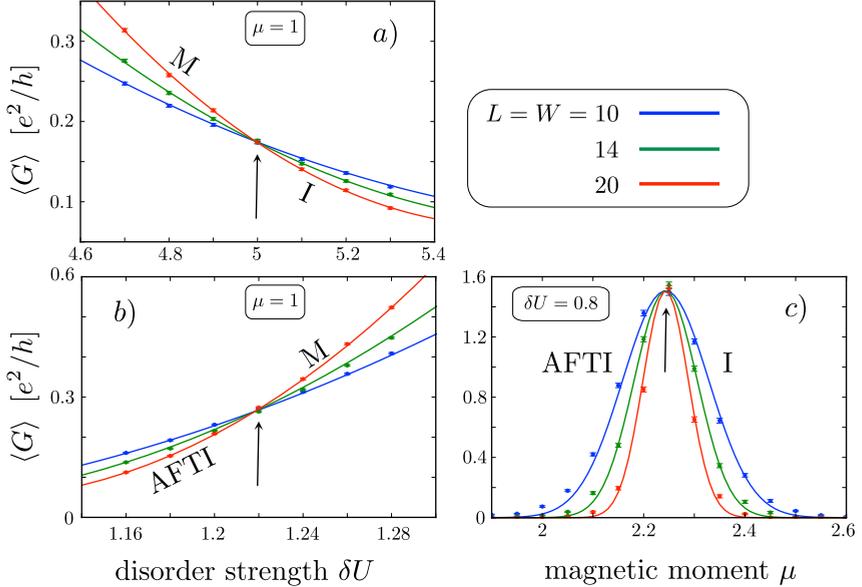
Figure 2.6: Disorder averaged conductance for three system sizes. Panels *a* and *b* show the transition between a metal (M) and an insulator which is topologically trivial (I) or nontrivial (AFTI). Panel *c* show the trivial-to-nontrivial insulator transition. The scale-independent conductance at the critical point of the phase transition is indicated by an arrow. The curves are guides to the eye. Data points from panels *a* and *b* are averages over 20000 disorder configurations, data points from panel *c* are averages over 200 configurations.

2.5 Discussion

We have investigated how disorder affects the phase diagram of a simple model in the class of antiferromagnetic topological insulators [72]. Depending on the disorder strength, topologically trivial (I) or nontrivial (AFTI) phases appear, as well as a metallic phase (M). The I-AFTI and M-AFTI phase boundaries are well described by the self-consistent Born approximation (dashed and solid curves in Fig. 2.5), including the location of the tri-critical point at which all three phases meet.

Without disorder, there is also an AFTI-AFTI transition at magnetic moment $\mu = 0$. When the sign of μ changes, the surface Dirac cone switches from the center to the edge of the Brillouin zone (Fig. 2.2). Precisely at the transition, the bulk gap closes and a Weyl cone appears with a
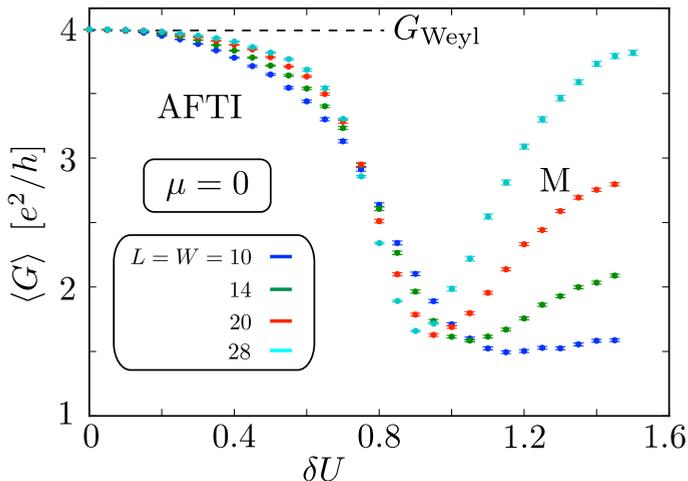
Figure 2.7: Disorder averaged conductance on the line $\mu = 0$, within the AFTI phase for weak disorder and metallic for strong disorder. The ballistic conductance at the Weyl point is indicated.

scale-invariant conductance G_{Weyl} (Fig. 2.3) and Fano factor F_{Weyl} (Fig. 2.4). Since the AFTI has a $\mathbb{Z}_2$ topological quantum number, there cannot be two topologically distinct nontrivial phases. We would expect disorder to open up a pathway of localized states in the phase diagram, that would connect the AFTI phases at positive and negative magnetic moment.

The numerical calculations in Fig. 2.7 show an indication of this localized regime on the line $\mu = 0$, for disorder strengths around $\delta U \approx 0.8$, before the transition into a metallic phase at stronger disorder. The limited range of system sizes does not allow for a conclusive identification, but the numerics is consistent with our expectation of one single topologically nontrivial phase.

In conclusion, we have demonstrated that the notion of an antiferromagnetic topological insulator [72], protected by the effective k-dependent time-reversal symmetry (2.8), extends to disordered systems where momentum k is no longer a good quantum number. The system then belongs to the class of *statistical* topological insulators [73, 74], protected by an ensemble-averaged symmetry.

3 Scattering theory of the chiral magnetic effect in a Weyl semimetal: Interplay of bulk Weyl cones and surface Fermi arcs

3.1 Introduction

The conduction electrons in a Weyl semimetal have an unusual velocity distribution in the Brillouin zone [94]. The conical band structure (Weyl cone) has a chirality that generates a net current at the Fermi level in the presence of a magnetic field [31]. The Weyl cones come in pairs of opposite chirality, so that the total current vanishes in equilibrium [26, 95, 96], but a nonzero current I parallel to the field B remains if the cones are offset by an energy μ — slowly oscillating to prevent equilibration [44, 45, 97–100]. This is the chiral magnetic effect (CME) from particle physics [101–104], see Refs. [105–107] for recent reviews in the condensed matter setting. In an infinite system the current density has the universal form [13, 42]

$$j_0 = -(e/h)^2 \mu B, \tag{3.1}$$

independent of material parameters. This amounts to a conductance of e^2/h in the lowest (zeroth) Landau level, multiplied by the degeneracy equal to the enclosed flux in units of the flux quantum. The minus sign in Eq. (3.1) follows from the usual convention of associating a positive μ to a positive energy offset of the Weyl cone with left-movers in the zeroth Landau level (the left Weyl cone in Fig. 3.1d).

The recent condensed-matter realizations of Weyl semimetals [48–53, 108] have boosted the search for the chiral magnetic effect [109–117]. Future experimental developments may well include nanostructured materials, to minimize effects of disorder. In a finite system, the zeroth Landau level in the bulk hybridizes with the Fermi arcs connecting the two Weyl cones along the surface [10, 118]. Previous studies [119, 120] have pointed to the importance of boundaries for the chiral magnetic effect — a sign reversal of the current density as one moves from the bulk towards a boundary ensures that zero current flows in response to a static perturbation. Here we wish to study how this interplay of surface and bulk states impacts on the chiral magnetic effect in response to a low-frequency dynamical perturbation. For that purpose we seek a linear response theory that does not assume translational invariance in an infinite system. A scattering formulation *à la* Landauer seems most appropriate for such a mesoscopic system.

The Landauer approach to electrical conduction considers the current driven between two spatially separated electron reservoirs by a chemical potential difference, and expresses this in linear response by a sum over transmission probabilities at the Fermi level [121–123]. The chiral magnetic effect is driven by a nonequilibrium population of the Weyl cones, so in reciprocal space (Brillouin zone) rather than in real space — we will show how to modify the Landauer formula accordingly.

We first apply our scattering formula to a current driven by a slowly oscillating offset μ of the Weyl cones (a so-called "chiral" or "axial" chemical potential [104]), and recover Eq. (3.1) in the infinite-system limit. We then turn to the more practical scenario of a current driven by a slowly oscillating magnetic field B. We find that the surface Fermi arcs give a contribution to the total induced current equal to *minus twice* the bulk contribution in the infinite-system limit. That the surface Fermi arc contribution does not vanish relative to the bulk contribution is unexpected and not captured by previous calculations of the chiral magnetic effect.

The outline of the chapter is as follows. In the next section 3.2 we derive the scattering formula for the chiral magnetic effect, in a general setting. In Sec. 3.4 we apply it to the model Hamiltonian of a Weyl semimetal from Ref. [26], summarized in Sec. 3.3. We evaluate the induced current in response to variations in μ and B, both numerically for a finite system and analytically in the limit of an infinite system size. Finite-size corrections are considered in some detail in Sec. 3.5. We conclude in Sec. 3.6 with a summary and a discussion of the robustness of the results against disorder scattering.

3.2 Scattering formula

For a scattering theory of the chiral magnetic effect we consider a disordered mesoscopic system attached to ideal leads. Such an "electron wave guide" has propagating modes with band structure $E_n(k)$, labeled by a mode index $n = 1, 2, \ldots$ and dependent on the wave vector k along the lead. At a given energy ε (measured relative to the equilibrium Fermi level E_{F}), each incident mode has wave vector $k_n(\varepsilon)$ and carries the same current e/h per unit energy interval*.

The scattering matrix $S(\varepsilon)$ relates amplitudes of incident and outgoing modes. We take a two-terminal geometry (the multi-terminal generalization is straightforward), with N modes each in the left and right lead — so S is a $2N \times 2N$ unitary matrix. The current I through the system can be calculated in the left lead, by current conservation it must be the same through each cross section.

The projection matrix onto the left lead is $\mathcal{P} = \left(\begin{smallmatrix} 1 & 0 \\ 0 & 0 \end{smallmatrix}\right)$, where each sub-block is an $N \times N$ matrix. The current is driven by a set of non-equilibrium occupation numbers $\delta f_n(\varepsilon)$, with $n = 1, 2, \ldots N$ for the left lead and $n = N + 1, N + 2, \ldots 2N$ for the right lead. We collect these numbers in a $2N \times 2N$ diagonal matrix $\delta\mathcal{F}(\varepsilon)$. The net current in the left lead is then given by the difference of incoming and outgoing currents,

$$ I = \frac{e}{h} \int d\varepsilon \, \mathrm{Tr} \left[\mathcal{P}\delta\mathcal{F}(\varepsilon) - \mathcal{P}S(\varepsilon)\delta\mathcal{F}(\varepsilon)S^\dagger(\varepsilon) \right]. \tag{3.2} $$

We consider the linear response to a slowly varying parameter X that adiabatically perturbs the system away from its equilibrium state at $X = X_0$. We assume that the wave vector k along the lead (say, in the z-direction) is not changed by the perturbation. This requires that the perturbation should neither break the translational invariance along z, nor involve a time-dependent vector potential component A_z.

The band structure evolves from $E_n(k|X_0)$ to $E_n(k|X_0 + \delta X)$. To first order in the perturbation δX the energy shift at constant k is

$$ E_n(k|X_0 + \delta X) - E_n(k|X_0) = \delta X \lim_{X \to X_0} \frac{\partial}{\partial X} E_n(k|X). \tag{3.3} $$

The corresponding deviation of the occupation number from the equilibrium

---

*To avoid a confusion of minus signs, we assign charge $+e$ to the carriers. The final result for the induced current contains e^2, so this sign convention does not affect it.

Fermi function $f_{\mathrm{eq}}(\varepsilon) = (1 + e^{\varepsilon/k_{\mathrm{B}}T})^{-1}$ is

$$
\begin{aligned}
\delta f_n(\varepsilon) &= f_{\mathrm{eq}}\big(E_n(k_n(\varepsilon)|X_0)\big) - f_{\mathrm{eq}}(\varepsilon) \\
&= -\delta X f'_{\mathrm{eq}}(\varepsilon) \lim_{X \to X_0} \frac{\partial}{\partial X} E_n(k_n(\varepsilon)|X),
\end{aligned}
\tag{3.4}
$$

where we have used that $E_n(k_n(\varepsilon)|X_0 + \delta X) \equiv \varepsilon$.

At zero temperature the derivative $f'_{\mathrm{eq}}(\varepsilon) \to -\delta(\varepsilon)$, so the expression (3.2) for the current contains only Fermi level scattering amplitudes. We may write it in a more explicit form in terms of the transmission probabilities

$$
T_n = \begin{cases} \sum_{m=N+1}^{2N} |S_{mn}|^2 & \text{for } 1 \le n \le N, \\ \sum_{m=1}^{N} |S_{mn}|^2 & \text{for } N+1 \le n \le 2N, \end{cases}
\tag{3.5}
$$

evaluated at $\varepsilon = 0$. (The two cases correspond to transmission from left to right or from right to left.) Since $\sum_{m=1}^{2N} |S_{mn}|^2 = 1$ because of unitarity, we have

$$
\begin{aligned}
I &= \frac{e}{h} \delta X \sum_{n=1}^{2N} \chi_n T_n, \\
\chi_n &= \lim_{k \to k_n} \lim_{X \to X_0} \frac{\partial E_n(k|X)}{\partial X} \times \operatorname{sign} \frac{\partial E_n(k|X)}{\partial k}.
\end{aligned}
\tag{3.6}
$$

The sign of the derivative $\partial E_n/\partial k$ distinguishes the right-moving modes $n = 1, 2, \ldots N$ from the left-moving modes $n = N+1, N+2, \ldots 2N$.

The Landauer conductance formula [121–123]

$$
G = I/V = (e^2/h)\textstyle\sum_{n=1}^{N} T_n
\tag{3.7}
$$

is obtained from Eq. (3.6) if we identify $\delta X = V$ with the voltage difference between the left and right lead, and then set $\chi_n = 1$ for $n = 1, 2, \ldots N$ and $\chi_n = 0$ for $n = N+1, N+2, \ldots 2N$. The chiral magnetic effect is driven by a non-equilibrium population in momentum space, rather than in real space, so modes from both leads contribute — hence the need to sum over $2N$ rather than N modes.

3.3 Model Hamiltonian of a Weyl semimetal

A simple model of a Weyl semimetal is given by the four-band Hamiltonian [26]

$$
\begin{aligned}
H(\boldsymbol{k}) &= t'\tau_z(\sigma_x \sin k_x + \sigma_y \sin k_y) + t'_z\tau_y \sin k_z \\
&\quad + M(\boldsymbol{k})\tau_x + \tfrac{1}{2}\gamma\tau_y\sigma_z + \tfrac{1}{2}\beta\sigma_z, \\
M(\boldsymbol{k}) &= M_0 + t(2 - \cos k_x - \cos k_y) + t_z(1 - \cos k_z).
\end{aligned} \tag{3.8}
$$

The Pauli matrices σ_j and τ_j ($j = x, y, z$) act, respectively, on the spin and orbital degree of freedom. The momentum $\boldsymbol{k}$ varies over the Brillouin zone $-\pi < k_j < \pi$ of a simple cubic lattice (lattice constant $a \equiv 1$). The material is layered in the x-y plane, with nearest-neighbor hopping energies t (within the layer) and t_z (along the z-axis). The primed terms t', t'_z indicate hopping with spin-orbit coupling. Inversion symmetry, $\tau_x H(-\boldsymbol{k})\tau_x = H(\boldsymbol{k})$, is broken by strain $\propto \gamma$, while time-reversal symmetry, $\sigma_y H^*(-\boldsymbol{k})\sigma_y = H(\boldsymbol{k})$, is intrinsically broken by a magnetization $\propto \beta$. Additionally, we may apply a magnetic field in the $+z$-direction, by substituting $k_y \mapsto k_y - eBx/\hbar$. The field strength is characterized by the magnetic length $l_B = \sqrt{\hbar/eB}$.

We confine the layers to a $W_x \times W_y$ lattice in the x-y plane, infinite in the z-direction so k_z remains a good quantum number. The tight-binding Hamiltonian in this wire geometry is diagonalized with the help of the KWANT toolbox [93], see Fig. 3.1. In zero magnetic field (panels a,c) there are two Weyl cones, gapped by the finite system size. The conical points (Weyl points) are separated along k_z by approximately β/t'_z and they are separated in energy by approximately γ. The precise energy separation μ that governs the chiral magnetic effect was determined from the bandstructure in an infinite system, for our parameter values it differs from γ by a few percent.

As long as $\mu, M_0 \ll \beta$ the Weyl cones remain distinct in an energy interval around $E = 0$. The Fermi velocity of the massless Weyl fermions is $v_{\mathrm{F}} = t'/\hbar$ in the plane of the layers and $v_{\mathrm{F},z} = t'_z/\hbar$ perpendicular to the layers. Surface states connect the Weyl cones across the Brillouin zone, forming the so-called Fermi arc. The arc states are chiral, spiraling along the wire with a velocity $v_{\mathrm{arc},z} = (\mu/\beta)v_{\mathrm{F},z}$, as illustrated in Fig. 3.2. In a magnetic field (panels b,d in Fig. 3.1) Landau levels develop. The Weyl cones are pushed away from $E = 0$, but the zeroth Landau level closes the gap. Just like the Fermi arc, the zeroth Landau level propagates along the wire, in opposite direction for the two Weyl cones.
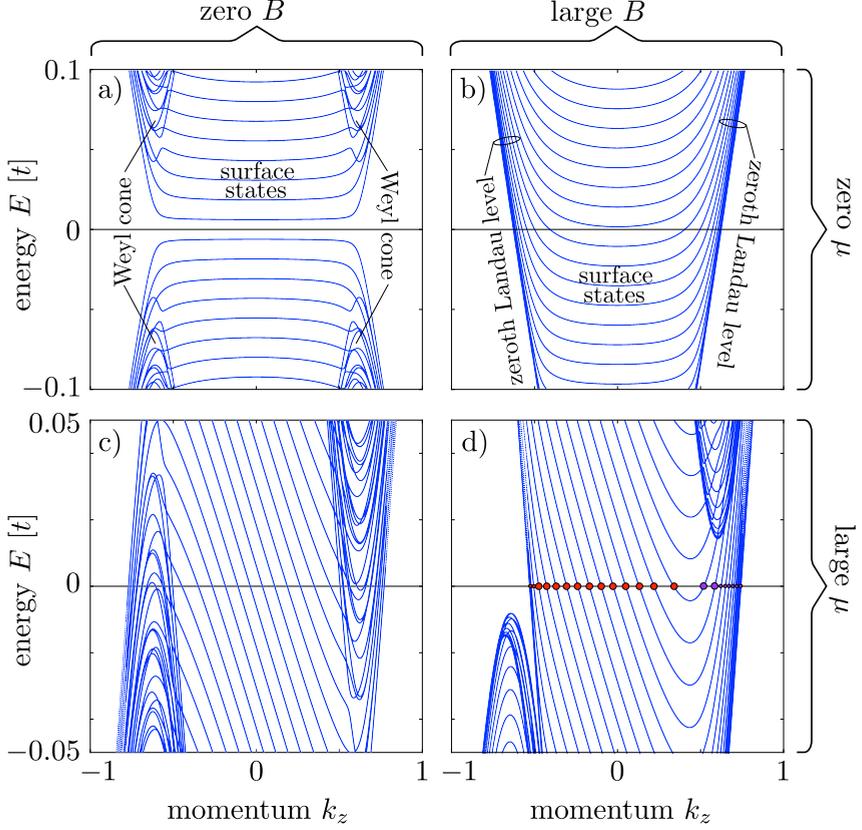
Figure 3.1: Band structure of the Hamiltonian (3.8) in a wire geometry along the z-axis. The panels show the Weyl cones in zero magnetic field (panels a,c), the Landau levels in a strong magnetic field along z (panels b,d for $l_B = 25$), each for $\pm k_z$ symmetry (panels a,b) and when this inversion symmetry is broken (panels c,d for $\gamma = 0.2\,t \Rightarrow \mu = 0.196\,t$). The other model parameters are $t_z = t'_z = t$, $t' = 2t$, $\beta = 1.2\,t$, $M_0 = -0.3\,t$, $W_x = W_y = 255$ in units of the lattice constant a. The intersections of the subbands $E_n(k_z)$ with the Fermi level $E_F = 0$ determine the momenta k_n appearing in the scattering formula (3.6). These are indicated by dots in panel d, colored purple or red depending on whether the mode propagates in the $+z$ or in the $-z$ direction (as determined by the sign of dE_n/dk_z).
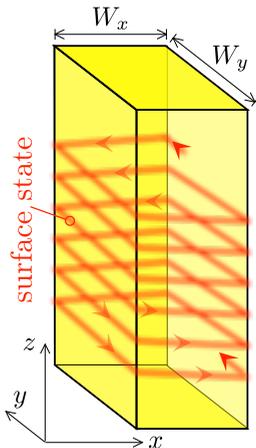
Figure 3.2: *Weyl solenoid.* Illustration of a chiral surface Fermi arc spiraling along the wire (cross-sectional area $\mathcal{A}$ and perimeter $\mathcal{P}$). Its flux sensitivity is set by the orbital magnetic moment $ev_{\mathrm{F}}\mathcal{A}/\mathcal{P}$, while the number of surface modes at the Fermi level scales $\propto \mathcal{P}$, so their total contribution to the magnetic response is $\propto \mathcal{A}$ — of the same order as the bulk contribution.

3.4 Induced current in linear response

3.4.1 Numerical results from the scattering formula

We have calculated the current density δj flowing along the wire in response to a slowly varying μ or B. In the former case we fix B at $l_B = 25$ and increase $\mu \equiv X$ from $X_0 \equiv 0$ to $\delta X \equiv \delta\mu$, in the latter case we fix $\mu = 0.196\, t$ and increase $B \equiv X$ from $X_0 \equiv 0$ to $\delta X \equiv \delta B$. We obtain the CME coefficients in linear response,

$$\mathcal{J}_\mu \equiv B^{-1}\delta j/\delta\mu, \;\; \mathcal{J}_B = \mu^{-1}\delta j/\delta B, \tag{3.9}$$

from the scattering formula (3.6), with $T_n \equiv 1$ (no disorder, so unit transmission for all modes). The Fermi level is set at $E_{\mathrm{F}} = 0$. Results are shown in Fig. 3.3. We see that the numerical data points[*] lie close to the dashed lines given by

$$\mathcal{J}_\mu = -(e/h)^2, \;\; \mathcal{J}_B = \tfrac{1}{2} \times (e/h)^2. \tag{3.10}$$

---

[*]The derivative $\partial E_n/\partial X$ needed in the scattering formula (3.6) can be calculated most easily from the Hellmann-Feynman equation $\partial E_n/\partial X = \langle \psi_n | \partial H/\partial X | \psi_n \rangle$, with ψ_n the eigenfunction of mode n. In this way a numerical differentiation of the energy spectrum can be avoided.
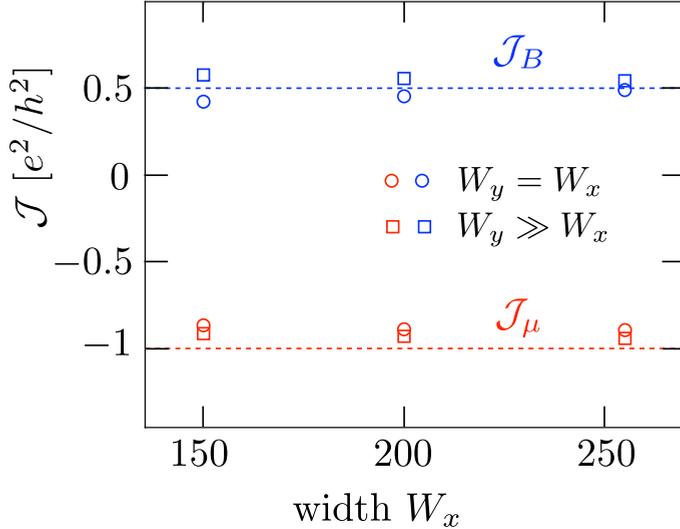
Figure 3.3: Results for $\mathcal{J}_B = \mu^{-1}\delta j/\delta B$ and $\mathcal{J}_\mu = B^{-1}\delta j/\delta\mu$ following from the scattering formula (3.6), for the Weyl semimetal Hamiltonian (3.8) with parameters as in Fig. 3.1. The data is shown at three different values of W_x, for two geometries: $W_y = W_x$ (circular symbols, hard-wall boundary conditions in both x and y directions) and $W_y = 5000 \gg W_x$ (square symbols, hard-wall boundary conditions along x, periodic boundary conditions along y).

The CME coefficient $\mathcal{J}_\mu$ agrees with the expected value from Eq. (3.1), while the CME coefficient $\mathcal{J}_B$ has the opposite sign and is smaller by a factor of two. Inspection of the contributions from individual modes, plotted in Fig. 3.4, indicates that surface states are behind the different response, as we now explain in some detail.

3.4.2 Why surface Fermi arcs contribute to the magnetic response in the infinite-system limit

Consider the propagating modes through a wire of diameter W. The number of surface modes scales $\propto W$, while the number of bulk modes scales $\propto W^2$, so one might surmise that surface contributions to the current density I/W^2 can be neglected in the limit $W \to \infty$. This is correct for $\mathcal{J}_\mu$ — but not for $\mathcal{J}_B$, because each surface mode individually contributes an amount $\propto W$, so the total surface contribution scales $\propto W^2$, just like the bulk contribution.
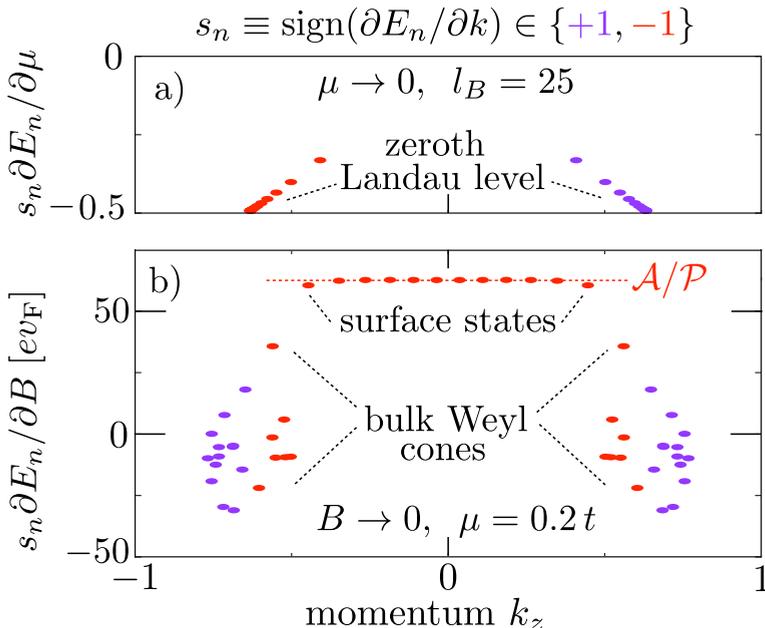
Figure 3.4: Contributions to $\mathcal{J}_\mu$ (panel a) and $\mathcal{J}_B$ (panel b) from each individual mode, corresponding to the band structures shown in Figs. 3.1b and 3.1c. The sum of these contributions produces the total CME coefficient of Fig. 3.3, at $W_y = W_x = 255$. The dotted line in panel b is the contribution (3.12) expected from the Fermi arc Hamiltonian (3.11) for a surface enclosing an area $\mathcal{A} = (255)^2$ with perimeter $\mathcal{P} = 4 \times 255$. The color of the data points distinguishes left-movers from right-movers, $s_n \equiv \text{sign}\,(\partial E_n/\partial k) = +1$ (purple) or -1 (red).

To make this argument more precise, we consider the effective Hamiltonian of the surface Fermi arcs,

$$H_{\text{arc}} = v_{\text{F}}(p_s - e\Phi/\mathcal{P}) - v_{\text{arc},z}p_z, \tag{3.11}$$

with p_s the component of the momentum along the perimeter of the wire in the x-y plane, of length $\mathcal{P}$ enclosing a flux $\Phi = B\mathcal{A}$ in an area $\mathcal{A}$. The energy spacing of the surface states at given momentum p_z along the wire is $\delta E = h v_{\text{F}}/\mathcal{P}$, so an energy separation μ of the Weyl cones pushes $N_{\text{arc}} = \mu/\delta E = \mu\mathcal{P}/h v_{\text{F}}$ surface modes through the Fermi level. Each contributes

$$\chi_n = \text{sign}(\partial E_n/\partial p_z) \times \partial E_n/\partial B = e v_{\text{F}} \mathcal{A}/\mathcal{P} \tag{3.12}$$
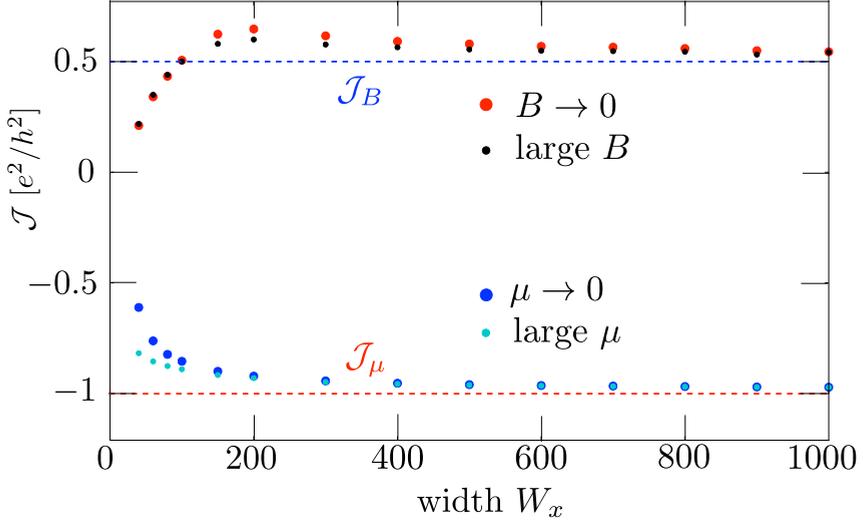
Figure 3.5: Same as Fig. 3.3, but for a larger range of widths W_x at fixed $W_y = 5000$ (periodic boundary conditions in the y-direction). The data for $\mathcal{J}_B = \mu^{-1}\delta j(B)/\delta B$ is shown at $\gamma = 0.1\,t \Rightarrow \mu = 0.098\,t$ in the limit $B \to 0$ and at a large magnetic field in the Landau level regime ($l_B = 50$). The data for $\mathcal{J}_\mu = B^{-1}\delta j(\mu)/\delta\mu$ is shown at $l_B = 50$ in the limit $\mu \to 0$ and for a large $\mu = 0.098\,t$.

to the induced current, which is just its orbital magnetic moment. The total surface contribution takes on the universal value

$$\mathcal{J}_{B,\mathrm{arc}} = (e/h)N_{\mathrm{arc}}\chi_n/\mu\mathcal{A} = (e/h)^2. \tag{3.13}$$

The red dotted line in Fig. 3.4b confirms this reasoning.

3.4.3 Bulk Weyl cone contribution to the magnetic response

The numerical data in Fig. 3.3 indicates that the bulk Weyl cones contribute

$$\mathcal{J}_{B,\mathrm{bulk}} = -\tfrac{1}{2}(e/h)^2 \tag{3.14}$$

to the CME coefficient induced by a magnetic field, for a total $\mathcal{J}_{B,\mathrm{bulk}} + \mathcal{J}_{B,\mathrm{arc}} = \tfrac{1}{2}(e/h)^2$. We have not found a simple intuitive argument for Eq. (3.14), but we do have an explicit analytical calculation, see App. 3.A.
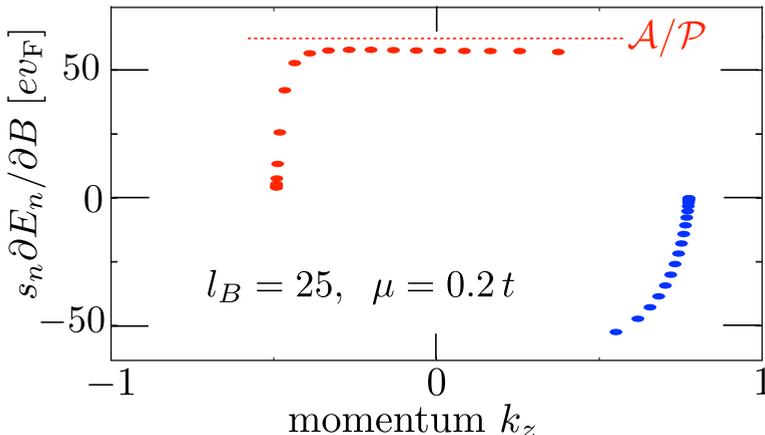
Figure 3.6: Same as Fig. 3.4b, but now at a large magnetic field corresponding to the bandstructure in Fig. 3.1d. The contribution from the surface Fermi arcs, close to $\mathcal{A}/\mathcal{P}$, goes to zero when they hybridize with the zeroth Landau level (for which $\partial E_n/\partial B = 0$).

The difference between $\mathcal{J}_\mu$ and $\mathcal{J}_B$ goes against the original expectation [44] that the low-frequency response to small variations in μ at fixed B should be the same as to small variations in B at fixed μ. That there is no such reciprocity was found recently in two studies [99, 100] of currents induced by an oscillating magnetic field in an infinite isotropic system. Their bulk response has a different numerical coefficient than our Eq. (3.14) (1/3 instead of 1/2), possibly because of the intrinsic anisotropy of a wire geometry.

3.4.4 Interplay of surface Fermi arcs with bulk Landau levels

So far we have considered the magnetic response in the zero-magnetic field limit, when the bulk contribution arises from Weyl cones. We can also ask for the current density δj in response to a slow variation $\delta X \equiv \delta B$ around some nonzero $X_0 \equiv B_0$, all at fixed μ. As shown in Fig. 3.5, the magnetic response is the same whether we vary B around zero or nonzero B_0. This is remarkable, because the bulk states are entirely different — Weyl cones versus Landau levels, compare the band structures in Figs. 3.1c and 3.1d. The individual modes also contribute very differently to $\mathcal{J}_B$, compare Figs. 3.4b and 3.6, and yet the net contribution is still close to $\frac{1}{2} \times (e/h)^2$. We
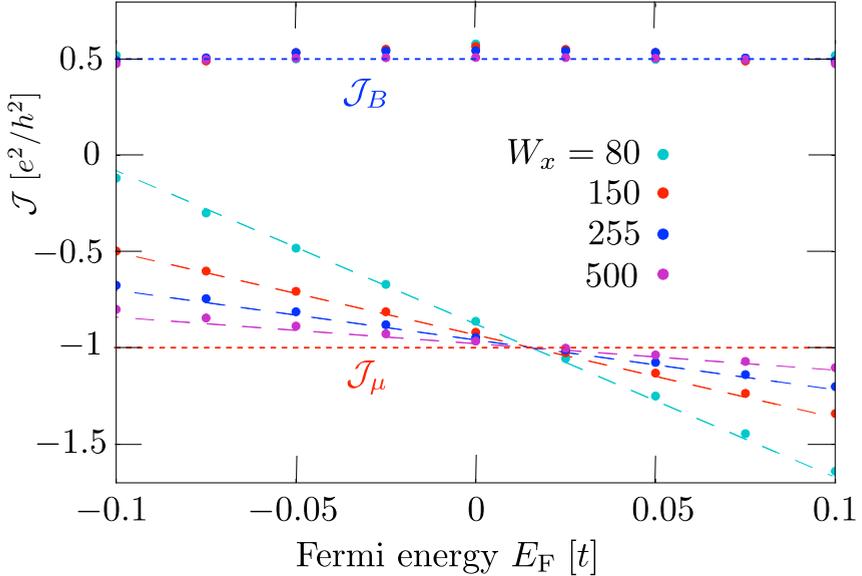
Figure 3.7: Fermi-energy dependence of the CME coefficients $\mathcal{J}_\mu = B^{-1}\delta j/\delta\mu$ (in the limit $\mu \to 0$ at $l_B = 25$) and $\mathcal{J}_B = \mu^{-1}\delta j/\delta B$ (in the limit $B \to 0$ at $\mu = 0.196\,t$), for different widths W_x at fixed $W_y = 5000$ (other parameters as in Fig. 3.1, periodic boundary conditions in the y-direction). The horizontal dotted lines are the expected values (3.10) in the limit of an infinite system, the dashed lines have a slope given by Eq. (3.15).

have not succeeded in an analytical derivation of this numerical result.

3.5 Finite-size effects

We have seen that the surface Fermi arcs modify the magnetic response $\delta j/\delta B$ even in the limit that the size of the system tends to infinity. The response $\delta j/\delta\mu$ to an energy displacement μ of the Weyl cones is unaffected by the surface states in the infinite-system limit, given by Eq. (3.1) in that limit. There are however finite-size effects from the surface state contributions, which we consider in this section.

As shown in Fig. 3.7, finite-size effects on $\mathcal{J}_\mu = B^{-1}\delta j/\delta\mu$ are sensitive to whether or not the Fermi level E_F is symmetrically arranged between the Weyl points ($E_F = 0$ in Fig. 3.1). The earlier plots (Figs. 3.3 and 3.5) were for $E_F = 0$, when finite-size effects are small. A variation

of E_{F} away from the symmetry point has little effect on the magnetic response $\mathcal{J}_B = \mu^{-1}\delta j/\delta B$, provided $|E_{\mathrm{F}}| \lesssim |\mu|$. In contrast, the Fermi level displacement introduces a substantial size-dependence in $\mathcal{J}_\mu$.

Inspection of the band structure in Fig. 3.1b shows that the degeneracy of the zeroth Landau level increases with increasing E_{F}, because surface modes are converted into bulk modes, at a rate given by the inverse of the level spacing $\delta E = h v_{\mathrm{F}}/\mathcal{P}$ (cf. Sec. 3.4.2). Each bulk mode contributes $-(e/h)\delta\mu/\mathcal{A}$ to the induced current density δj, so we expect a finite-size correction to $\mathcal{J}_\mu = B^{-1}\delta j/\delta\mu$ equal to $-(e/h)(B\mathcal{A})^{-1}(E_{\mathrm{F}}/\delta E)$, hence

$$\mathcal{J}_\mu = -(e/h)^2 \left(1 + \frac{\mathcal{P}}{\mathcal{A}} \frac{E_{\mathrm{F}}}{eBv_{\mathrm{F}}}\right). \tag{3.15}$$

As seen in Fig. 3.7, the slope of the E_{F} dependence of J_μ is accurately described by Eq. (3.15).

3.6 Conclusion and discussion of disorder effects

Fig. 3.5 summarizes our main finding: It is known [44, 45, 97–100] that the chiral magnetic effect in a Weyl semimetal can be driven either by a slowly varying inversion-symmetry breaking μ or by a slowly varying magnetic field B. Contrary to the expectation from an infinite system, we find for a finite system that the induced current in the two cases has opposite sign. The difference is due to the surface Fermi arcs, but it is not a finite-size effect: The surface modes and the bulk modes give comparable contribution to the magnetic response no matter how large the system is, because the smaller number of surface modes is compensated by their stronger B-sensitivity.

This finding results from a scattering formulation of the chiral magnetic effect, that we have developed as an alternative to the established Kubo formulation [124, 125]. Similarly to the Landauer formula for electrical conduction, the scattering formula (3.6) is ideally suited to describe finite and disordered systems, without translational invariance. Here we focused on the surface effects in a finite system, but in closing we briefly consider the disorder effects.

A qualitative prediction can be made without any calculation. In Eq. (3.6) disorder reduces the contribution from each mode n by its transmission probability T_n. Assume that the disorder potential is smooth on the scale of the lattice constant a, so that it predominantly couples nearby modes

in the Brillouin zone (with k_n's differing by much less than $1/a$). This coupling can only lead to backscattering, reducing T_n below unity, if it involves both left-moving and right-moving modes. Inspection of Fig. 3.4b shows that the surface modes are insensitive to backscattering, because they all move in the same direction along the wire, in contrast to the bulk Weyl cones. Disorder will therefore reduce the Weyl cone contribution $\mathcal{J}_{B,\text{bulk}} = -\frac{1}{2}(e/h)^2$ to the magnetic response, without affecting the arc state contribution $\mathcal{J}_{B,\text{arc}} = (e/h)^2$. Since these contributions have opposite sign, we predict that disorder will *increase* the magnetically induced current.

For sufficiently strong disorder the bulk contribution to $\mathcal{J}_B$ may be fully suppressed, leaving a B-induced current density equal to $j = (e/h)^2 \mu B$, carried entirely by the surface Fermi arc. This has the same topological origin as the zeroth Landau level that carries the μ-induced current (3.1) — both the Fermi arc and the zeroth Landau level connect Weyl cones of opposite chirality [10, 118]. It has been argued [99, 100] that the chiral magnetic effect produced by an oscillating B is fundamentally different from that produced by an oscillating μ, because the former lacks the topological protection that is the hallmark of the latter. By including surface conduction we can now offer an alternative perspective: Both the μ-response and the B-response are similarly protected by chirality, the difference is that one is a bulk current and the other a surface current.

From an experimental point of view, the inversion-symmetry breaking that sets μ is hardly adjustable, preventing a direct measurement of $\delta j / \delta \mu$, while the magnetic field induced current $\delta j / \delta B$ seems readily accessible. We note that Landau levels are not required for the B-response, so one can work with a nanowire of width small compared to the magnetic length. In such a quasi-one-dimensional system long-range impurity scattering may localize the bulk states, without significantly affecting the chiral surface states. One would be searching for an oscillating current $I(\omega) \cos \omega t$ along the wire in response to an oscillating parallel magnetic field. The frequency ω should be below μ and above the inelastic relaxation rate of the surface modes. The magnetic response is quasi-DC, showing a plateau in this ω-range that would distinguish it from any electrically induced AC current $I(\omega) \propto \omega$.

A final word on nomenclature. The non-topological bulk contribution to the B-induced current has been termed the "gyrotropic magnetic effect" [100]. Because the B-induced current in the surface Fermi arc originates from the same chiral anomaly as the μ-induced current in the zeroth Landau level, we use the name "chiral magnetic effect" for both.

3.A Analytical calculation of the bulk contribution to the magnetic response

We wish to derive the result (3.14) for the contribution

$$\mu^{-1}\delta j_{\text{bulk}}/\delta B = -\tfrac{1}{2}(e/h)^2 \qquad (3.16)$$

from the bulk Weyl cones to the magnetic response. We assume that the two Weyl cones are non-overlapping at the Fermi energy (as they are in Fig. 3.1c), so we can consider them separately.

A single Weyl cone has Hamiltonian

$$H_{\text{Weyl}} = v_x k_x \sigma_x + v_y k_y \sigma_y + v_z k_z \sigma_z. \qquad (3.17)$$

(We have set $\hbar \equiv 1$ for ease of notation, but we will reinstate it at the end.) For generality, we allow for an anisotropic velocity (v_x, v_y, v_z). The modes propagating along the cylindrical wire have energy $E_n(k_z)$. We seek the magnetic moment $\partial E_n(k_z)/\partial B$ for an infinitesimal magnetic field B in the z-direction (along the axis of the cylinder).

For sufficiently large transverse dimensions W_x, W_y the boundary conditions should be irrelevant for the bulk response, and we use this freedom to simplify the calculation. To isolate the bulk contribution we prefer a boundary condition that does not bind a surface state.

In the y-direction we impose periodicity, so that k_y is a good quantum number. The system is then represented by a hollow cylinder of circumference W_y, with an inner and an outer surface at $x = 0$ and $x = W_x$. We can use periodic or antiperiodic boundary conditions,

$$k_y = 2\pi n/W_y \ \ \text{or} \ \ k_y = 2\pi(n + \tfrac{1}{2})/W_y,$$
$$n = 0, \pm 1, \pm 2, \ldots, \qquad (3.18)$$

in the large-W_y limit it makes no difference.

In the x-direction we choose a zero-current boundary condition. A simple choice is to take the spinor $\psi(x, y)$ as an eigenfunction of σ_y at the two surfaces $x = 0$ and $x = W_x$,

$$\lim_{x \to 0} \psi(x, y) = f(y) \begin{pmatrix} 1 \\ i \end{pmatrix}, \quad \lim_{x \to W_x} \psi(x, y) = g(y) \begin{pmatrix} 1 \\ i \end{pmatrix}, \qquad (3.19)$$

for arbitrary complex functions $f(y)$, $g(y)$. This boundary condition corresponds to confinement by a mass term $\propto \sigma_z$ of infinite magnitude and opposite sign at the two surfaces. No surface state is produced by mass

confinement. For $k_z = 0$ the sign change of the mass term does produce a spurious chiral state $\psi = e^{ik_y y}\binom{1}{i}$, $E = v_y k_y$, which carries no current in the z-direction and can therefore be ignored.

The solution of the eigenvalue equation $H_{\text{Weyl}}\psi = E\psi$ that satisfies the boundary condition (3.19) is given by

$$\psi(x,y) = \frac{1}{Z}e^{ik_y y}\left[(E - iv_x k_x - v_y k_y + v_z k_z)\begin{pmatrix} E + v_z k_z \\ v_x k_x + iv_y k_y \end{pmatrix}e^{ik_x x}\right.$$
$$\left. - (E + iv_x k_x - v_y k_y + v_z k_z)\begin{pmatrix} E + v_z k_z \\ -v_x k_x + iv_y k_y \end{pmatrix}e^{-ik_x x}\right],$$
$$\tag{3.20}$$

$$k_x = \pi m/W_x, \quad m = 1, 2, 3, \ldots. \tag{3.21}$$

The band structure $E_{nm}(k_z)$ is determined by the dispersion relation

$$E^2 = (\pi m v_x/W_x)^2 + (2\pi n v_y/W_y)^2 + (v_z k_z)^2. \tag{3.22}$$

Normalization $\langle\psi|\psi\rangle = 1$ gives

$$Z^2 = 8W_x W_y E(E - v_y k_y)(E + v_z k_z)^2. \tag{3.23}$$

The magnetic response is induced by the vector potential $A_y = B(x+X_0)$, with an offset X_0 that accounts for the flux $BW_y X_0$ enclosed by the inner surface of the cylinder. The magnetic moment results from

$$\frac{\partial E}{\partial B} = \langle\psi|\partial H/\partial B|\psi\rangle = -ev_y\langle\psi|(x + X_0)\sigma_y|\psi\rangle$$
$$= -\frac{ev_x v_y v_z k_z}{2E(E - v_y k_y)} - \frac{ev_y^2 k_y}{E}(X_0 + W/2). \tag{3.24}$$

The second term is the magnetic moment of a charge e circulating along the inner surface of the cylinder with velocity $\partial E/\partial k_y = v_y^2 k_y/E$. It drops out when we sum the contributions from $+k_y$ and $-k_y$, producing the magnetic moment

$$\sum_{\pm k_y}\frac{\partial E}{\partial B} = -\frac{ev_x v_y v_z k_z}{E^2 - v_y^2 k_y^2} = -\frac{ev_x v_y v_z k_z}{v_x^2 k_x^2 + v_z^2 k_z^2} \tag{3.25}$$

plotted in Fig. 3.8.

We fix the energy $E_{nm} = E$, adjusting k_z accordingly for each n and m. Both $+k_z$ and $-k_z$ satisfy the dispersion relation (3.22). We consider separately the sum over the magnetic moment of the modes with $k_z > 0$
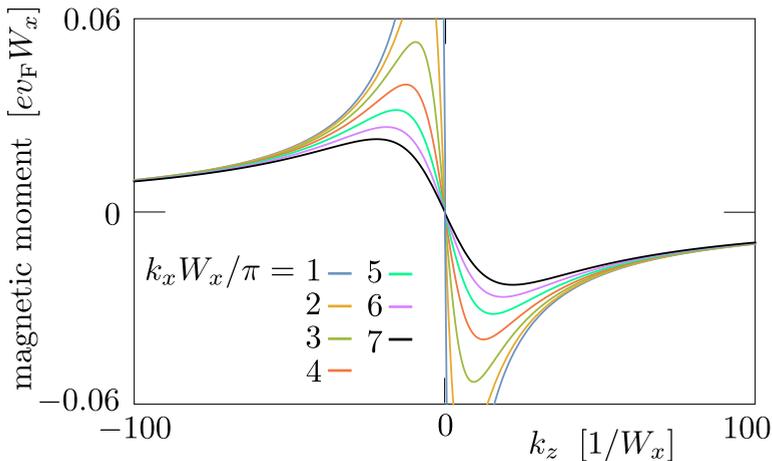
Figure 3.8: Magnetic moment (3.25) of a single Weyl cone (isotropic, $v_x = v_y = v_z \equiv v_F$), summed over $+k_y$ and $-k_y$, as a function of k_z for the seven lowest quantized values of $k_x = m\pi/W_x$. The quantization of k_y can be ignored for $W_y \gg W_x$, so the discrete modes merge into a continuous curve.

and $k_z < 0$, so that we can distinguish left-movers from right-movers in the scattering formula (3.6). In the large-W limit the sum over k_x and k_y, quantized by Eqs. (3.18) and (3.21), can be replaced by an integration over the k_x-k_y plane,

$$\sum_{nm}{}' \mapsto \frac{W_x W_y}{2\pi^2} \int_0^\infty dk_x \int_{-\infty}^\infty dk_y \, \theta(E^2 - v_x^2 k_x^2 - v_y^2 k_y^2), \qquad (3.26)$$

with $\theta(s)$ the unit step function. The prime in the summation indicates that we include only half of the modes, with a given sign of k_z. The integral over Eq. (3.24) is readily evaluated in polar coordinates,

$$\begin{aligned}
\sum_{nm}{}' \left. \frac{\partial E_{nm}}{\partial B} \right|_{E_{nm}=E} &= -(\text{sign } k_z)\frac{eW_x W_y}{4\pi^2 E} \\
&\quad \times \int_{-\pi/2}^{\pi/2} d\phi \int_0^{|E|} r\,dr \, \frac{\sqrt{E^2 - r^2}}{E - r\sin\phi} \\
&= -(\text{sign } k_z)\frac{eW_x W_y |E|}{8\pi}. \qquad (3.27)
\end{aligned}$$

The quantity χ_{nm} that determines the magnetically induced current $\delta I/\delta B$ according to Eq. (3.6) is the magnetic moment $\partial E_{nm}/\partial B$ times

the sign of the velocity $\partial E_{nm}/\partial k_z$ in the z-direction. The sign of the velocity in a single Weyl cone (with Weyl point at $\boldsymbol{k} = 0$, $E = 0$) equals the product of the sign of k_z and the sign of E_{nm}, hence

$$
\sum_{nm} \chi_{nm} = \sum_{nm} \left(\text{sign} \, \frac{\partial E_{nm}}{\partial k_z} \right) \frac{\partial E_{nm}}{\partial B} \bigg|_{E_{nm}=E}
$$
$$
= -\frac{eW_x W_y E}{4\pi\hbar}. \tag{3.28}
$$

In the last equation we have reinstated the $\hbar$ that we had previously set to unity. There is no prime in the summation because now both signs of k_z are included.

We conclude that the contribution to the induced current density $\delta j = \delta I/W_x W_y$ from a single Weyl cone at energy $E = \mu/2$ is

$$
\delta j = \frac{e}{h} \frac{\delta B}{W_x W_y} \sum_{nm} \chi_{nm} = -\tfrac{1}{4}(e/h)^2 \mu \delta B. \tag{3.29}
$$

The other Weyl cone contributes the same amount, for a total CME coefficient given by Eq. (3.16).

4 Weyl-Majorana solenoid

4.1 Introduction

A three-dimensional Weyl semimetal has topological features that are lacking in its two-dimensional counterpart, graphene [20, 31, 94]. One striking feature is the appearance of surface states, in Fermi arcs connecting Weyl cones of opposite topological charge (Chern number or Berry curvature) [10]. Unlike the surface states of a topological insulator, which are the only source of metallic conduction, the Fermi arcs at the surface compete with the Weyl cones in the bulk when it comes to transport properties. Quantum oscillations in the magnetoresistance are one example of an effect where the Fermi arcs play a prominent role [126, 127], the chiral magnetic effect without Landau levels is another example [46].

An interesting way to differentiate surface from bulk is to bring the Weyl semimetal into contact with a superconductor. While the Weyl cones in the bulk remain largely unaffected, the surface states acquire the mixed electron-hole character of a charge-neutral Bogoliubov quasiparticle — a Majorana fermion [69, 70, 117, 128–130]. Here we investigate this proximity effect in the nanowire geometry of Fig. 4.1, in which an axial magnetization causes the surface modes to spiral along the wire, essentially forming a solenoid on the nanoscale [46]. We study the dispersion relation of the Majorana modes and identify a mechanism to trap the quasiparticles at a specified location along the wire.
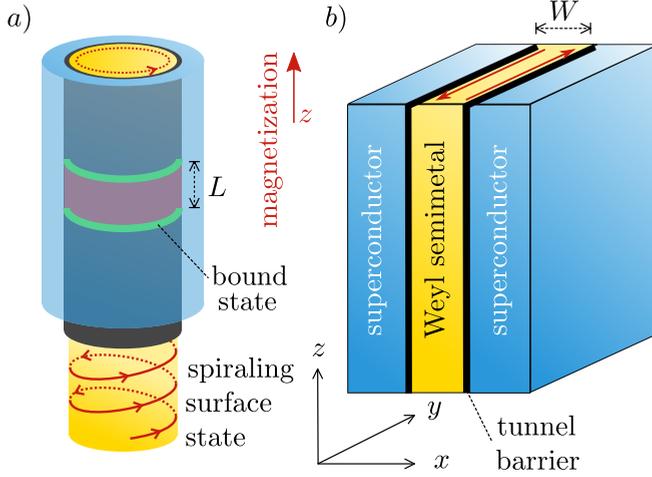
Figure 4.1: Panel a) Weyl-Majorana solenoid, formed by a Weyl semimetal wire with an axial magnetization, coupled via a tunnel barrier to a superconductor. Charge-neutral Majorana modes propagate along the wire, confined to the normal-superconductor (NS) interface. A gap inversion in a segment of length L, induced by a variation in coupling strength, traps a pair of quasiparticles at the two ends of the segment. Panel b) SNS slab geometry to study the Majorana modes at the NS interface.

In the next section we identify the pair of $\mathbb{Z}_2$ quantum numbers ν, κ that label the four surface modes in a given orbital subband. The electron-hole index ν is generic for any surface state where electrons and holes are coupled by Andreev reflection [131–133]. The connectivity index κ is specific for the Fermi arcs, it distinguishes whether the surface state reconnects in the bulk with the Weyl cone at positive or negative energy. In Sec. 4.3 we construct the 4×4 matrix Hamiltonian in the ν, κ basis, constrained by particle-hole symmetry, as an effective low-energy description of the two-dimensional surface modes.

We then proceed in Sec. 4.4 with a numerical calculation of the three-dimensional band structure of a microscopic model Hamiltonian. The unexpected feature revealed by this simulation is a gap inversion, visible in the band structure as a level crossing between two surface modes with the same connectivity index. The gap inversion can be controlled by variation of the tunnel coupling between the semimetal and the superconductor. At the domain wall where the gap changes sign, a charge-neutral quasiparticle

is trapped — as we demonstrate numerically and explain within the context of the effective surface Hamiltonian in Sec. 4.5. In Sec. 4.6 we study the same gap inversion analytically, via a mode-matching calculation. In the concluding Sec. 4.7 we comment on the relation of the gap inversion to the flow of Berry curvature in the Brillouin zone.

4.2 Connectivity index of surface Fermi arcs

The geometry under consideration is shown in Fig. 4.1. A Weyl semimetal wire oriented along the z-axis is covered by a superconductor. We include a thin insulating layer between the superconductor and the Weyl semimetal, forming a tunnel barrier. A magnetization in the z-direction breaks time-reversal symmetry and separates the Weyl cones along the p_z momentum direction in the Brillouin zone. (Induced superconductivity in the presence of time-reversal symmetry, with minimally four Weyl points, has a different phenomenology [69].) The surface states connecting the Weyl cones are chiral, circulating with velocity v_ϕ in a direction set by the magnetization. If inversion symmetry is broken the surface states also spiral with velocity v_z along the wire [46].

As shown in Fig. 4.2, resulting from a model calculation described in Sec. 4.4, at the interface with a superconductor the surface spectrum is drastically modified. We seek an effective Hamiltonian that describes this proximity effect on the Fermi arcs.

The first question we have to address is which pairs of states are coupled by the superconducting pair potential Δ. In the bulk spectrum the answer is well known [70, 117]: Superconductivity couples electrons in a Weyl cone of positive Berry curvature to holes in a Weyl cone of negative Berry curvature, and vice versa. To decide this question for the surface states, we assign to each Fermi arc a "connectivity index" $\kappa = \pm 1$, depending on whether it reconnects in the bulk with the Weyl cone at positive or negative energy. Inspection of Fig. 4.2 shows that Δ predominantly couples Fermi arcs with same κ, pushing them apart, without removing the crossing between states of opposite κ.

More explicitly, in a slab geometry we can identify $\kappa = \text{sign} \, k_y$ and in a cylindrical wire geometry we would have $\kappa = \text{sign} \, p_\phi$. The coupling of states with different κ is then forbidden by (translational or rotational) symmetry. More generally, in the absence of any symmetry, the sign of $\kappa = \pm 1$ says whether the Fermi arc connects with the Weyl cone at $\pm E$, and thus identifies which pairs of Fermi arcs are predominantly coupled by Δ.
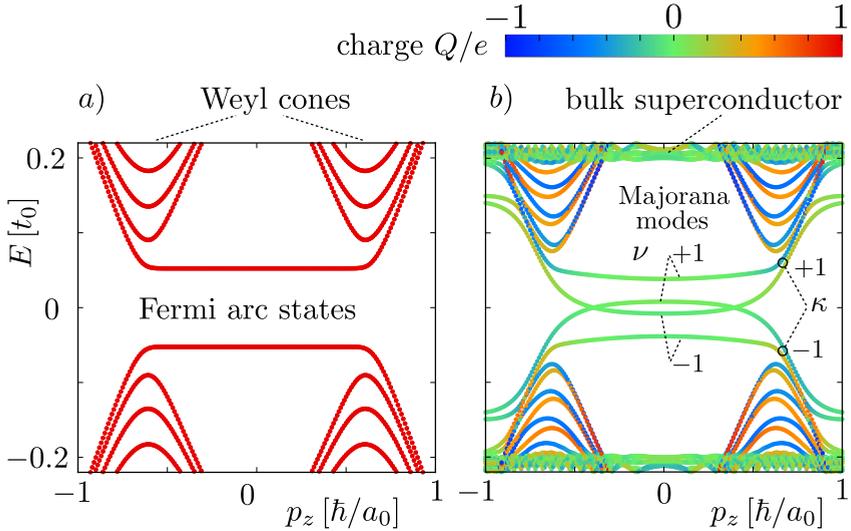
Figure 4.2: Band structure of a Weyl semimetal in the slab geometry of Fig. 4.1b, calculated from the tight-binding model described in the text[*]. In panel a) there is only the Weyl semimetal, in panel b) the superconducting contacts have been added. Inversion symmetry has not been broken, so the spectrum has $\pm p_z$ symmetry, in addition to the particle-hole symmetry $E(p_z) = -E(-p_z)$. In the slab geometry the transverse wave vector k_y is a good quantum number, and to make the figure less crowded only subbands at a single value of k_y are shown. (The Fermi arcs in panel a) are approximately at $\pm v_\phi \sin k_y$.) The superconductor breaks up the two Dirac fermion surface modes in panel a) into four Majorana fermion modes in panel b), labeled by a pair of indices $\kappa, \nu = \pm 1$. The Majorana modes are nearly charge-neutral, as indicated by the color scale (with electron charge $+e$).

4.3 Effective surface Hamiltonian

The superconducting proximity effect is governed by the Bogoliubov-De Gennes (BdG) Hamiltonian, describing the coupling of electrons and holes by the pair potential. In the numerical simulations we will work with the BdG Hamiltonian in a 3D microscopic model. For analytical insight we aim for an effective 2D description involving only surface modes.

---

[*]The microscopic model parameters in the slab geometry of Fig. 4.2 are (energies in units of t_0, lengths in units of a_0): $t = 2$, $t_z = 1$, $m_0 = -0.3$, $\lambda = 0$, $\beta = 0.6$, $\tilde{t} = 7$, $\tilde{t}_z = 3.5$, $\mu_W = 10^{-4}$, $\mu_S = 3.5$, $U_{\text{barrier}} = 0.1$, $\Delta_0 = 0.2$, $d_{\text{barrier}} = 2$, $W = 120$, $k_y = \pi/120$.

Each orbital subband n is associated with four Majorana modes, labeled by a pair of $\mathbb{Z}_2$ indices κ, ν. (See Fig. 4.2.) The connectivity index $\kappa = \pm$ identifies the connectivity of the surface mode (with the Weyl cone at positive or negative energy), the electron-hole index $\nu = \pm$ identifies the pair of Majorana fermions that form a Dirac fermion. The corresponding BdG Hamiltonian $\mathcal{H}_n$ is a 4×4 matrix with p_z-dependent elements. In what follows we omit the subband index n for ease of notation.

The fundamental symmetry of the BdG Hamiltonian is particle-hole symmetry,

$$\mathcal{H}(p_z) = -\kappa_y \nu_y \mathcal{H}^*(-p_z) \kappa_y \nu_y, \tag{4.1}$$

with Pauli matrices κ_α and ν_α acting, respectively on the connectivity and electron-hole degree of freedom ($\alpha = 1, 2, 3 \mapsto x, y, z$ and $\alpha = 0$ for the unit matrix). The operation of particle-hole conjugation squares to $+1$, which places the system in symmetry class D [28] — this is the appropriate symmetry class in the absence of time-reversal and spin-rotation symmetry.

If we neglect the mixing by disorder of surface states with opposite connectivity index $\kappa = \pm$, the 4×4 matrix $\mathcal{H}$ decouples into two blocks $H_\pm$ related by particle-hole symmetry,

$$\mathcal{H} = \begin{pmatrix} H_+ & 0 \\ 0 & H_- \end{pmatrix}, \quad H_-(p_z) = -\nu_y H_+^*(-p_z) \nu_y. \tag{4.2}$$

The 2×2 matrices $H_\pm$ can be decomposed into Pauli matrices,

$$H_\pm(p_z) = \pm D_0(\pm p_z) \nu_0 + \sum_{\alpha=1}^{3} D_\alpha(\pm p_z) \nu_\alpha, \tag{4.3}$$

with real p_z-dependent coefficients D_α.

Diagonalization of the Hamiltonian (4.2) gives the dispersion relation $E_{\kappa,\nu}(p_z)$ of the four Majorana modes in the n-th subband,

$$E_{\kappa,\nu}(p_z) = \kappa D_0(\kappa p_z) + \nu \sqrt{\sum_{\alpha=1}^{3} D_\alpha^2(\kappa p_z)}. \tag{4.4}$$

Particle-hole symmetry is expressed by $E_{\kappa,\nu}(p_z) = -E_{-\kappa,-\nu}(-p_z)$. Inversion symmetry, $E_{\kappa,\nu}(p_z) = E_{\kappa,\nu}(-p_z)$, is satisfied if D_0 is an even function of p_z while each of the functions D_1, D_2, D_3 has a definite parity (even or odd).

4.4 Numerical simulation of a microscopic model

We now turn to a microscopic model of a Weyl semimetal in contact with a superconductor, which we solve numerically. The Weyl semimetal has
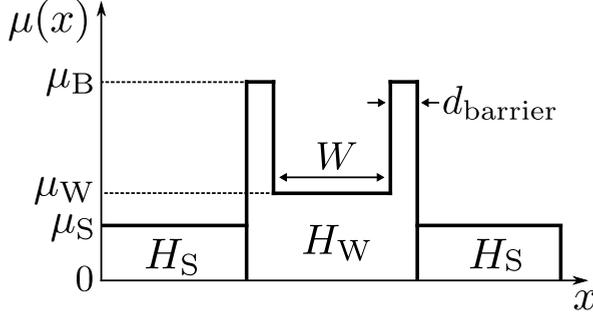
Figure 4.3: Spatial profile of the chemical potential $\mu(x)$.

BdG Hamiltonian

$$H_W(\boldsymbol{k}) = \nu_z\tau_z(t\sigma_x \sin k_x + t\sigma_y \sin k_y + t_z\sigma_z \sin k_z)$$
$$+ m(\boldsymbol{k})\nu_z\tau_x\sigma_0 + \lambda\nu_z\tau_z\sigma_0 + \beta\nu_0\tau_0\sigma_z - \mu\nu_z\tau_0\sigma_0,$$
$$m(\boldsymbol{k}) = m_0 + t(2 - \cos k_x - \cos k_y) + t_z(1 - \cos k_z), \qquad (4.5)$$

with chemical potential μ and charge operator

$$Q = -e\frac{\partial H_W}{\partial \mu} = e\nu_z\tau_0\sigma_0. \qquad (4.6)$$

The Pauli matrices σ_α and τ_α refer to spin and orbital degrees of freedom, respectively, while ν_α acts on the electron-hole index. The momentum $\boldsymbol{k}$ varies over the Brillouin zone $|k_\alpha| < \pi$ of a simple cubic lattice (lattice constant $a_0 \equiv 1$). This is a model of a layered material in the Bi$_2$Se$_3$ family [26], with weak coupling $t_z < t$ in the z-direction, perpendicular to the layers in the x–y plane.

The particle-hole symmetry relation is

$$H_W(\boldsymbol{k}) = -\sigma_y\nu_y H_W^*(-\boldsymbol{k})\sigma_y\nu_y. \qquad (4.7)$$

The magnetization term $\propto \beta$ breaks time-reversal symmetry, $H_W(\boldsymbol{k}) = \sigma_y H_W^*(-\boldsymbol{k})\sigma_y$. Inversion symmetry, $H_W(\boldsymbol{k}) = \tau_x H_W(-\boldsymbol{k})\tau_x$, is broken by the strain term $\propto \lambda$.

The Weyl semimetal is in contact with a spin-singlet s-wave superconductor, with Hamiltonian

$$H_S = [\tilde{t}(2 - \cos k_x - \cos k_y) + \tilde{t}_z(1 - \cos k_z)]\nu_z\tau_0\sigma_0$$
$$- \mu\nu_z\tau_0\sigma_0 + \Delta_0\nu_x\tau_0\sigma_0. \qquad (4.8)$$
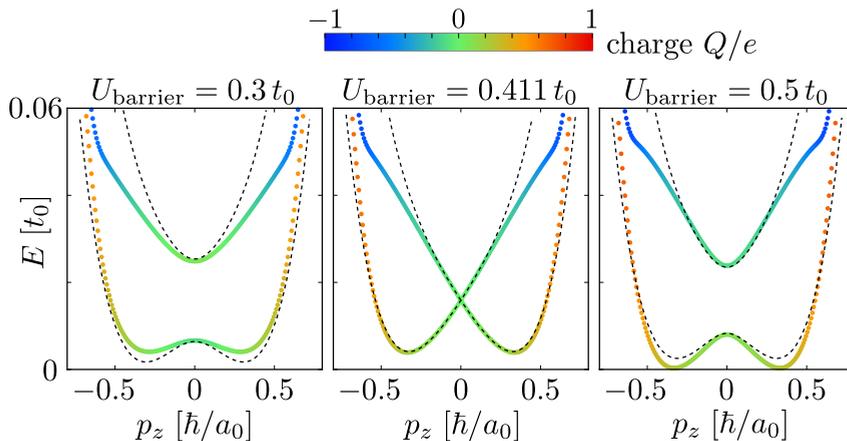
Figure 4.4: Data points: Band structure in the slab geometry (colored according to the charge expectation value), showing the level crossing at $p_z = 0$ between a pair of Majorana modes with $\kappa = +1$, $\nu = \pm 1$. The parameters are those of Fig. 4.2b, except for the tunnel barrier height U_{barrier}, which is varied to tune through the gap inversion. The dashed curves are fits* to the dispersion (4.9) from the effective surface Hamiltonian.

There are different chemical potentials in the Weyl semimetal, $\mu = \mu_{\text{W}}$, and in the superconductor, $\mu = \mu_{\text{S}}$. At the NS interface we include an electrostatic potential barrier of width d_{barrier}, raising μ to a value $\mu_{\text{B}} \equiv U_{\text{barrier}}$. The resulting spatial profile $\mu(x)$ is shown in Fig. 4.3.

We consider the two geometries shown in Fig. 4.1, a wire geometry and a computationally more efficient slab geometry†. In each case there is translational invariance along the z-direction. In the slab geometry there is in addition translational invariance in the y-direction, so the modes are labeled by a continuous quantum number k_y‡.

The dispersion relation in the slab geometry is shown in Fig. 4.2. The mode crossings at nonzero p_z appear because modes with different connectivity index κ are uncoupled in the absence of disorder. In Fig. 4.4 we show a different type of crossing, near $p_z = 0$ between modes with the same κ, induced by variation of the tunnel barrier height. This crossing appears

---

*The fit parameters used in Fig. 4.4 are $D_0(p_z) = 0.016 + 0.035\,p_z^2 + 0.24\,p_z^4$, $c = 0.085$, $c'' = 0.056$.

†To discretize the model Hamiltonian we used the Kwant toolbox [93].

‡The slab geometry has a $\pm k_y$ degeneracy in the spectrum, corresponding to surface states at the opposite NS interfaces $x = \{0, W\}$. We therefore only need to show a single sign of k_y to obtain the full spectrum, as in Fig. 4.2.
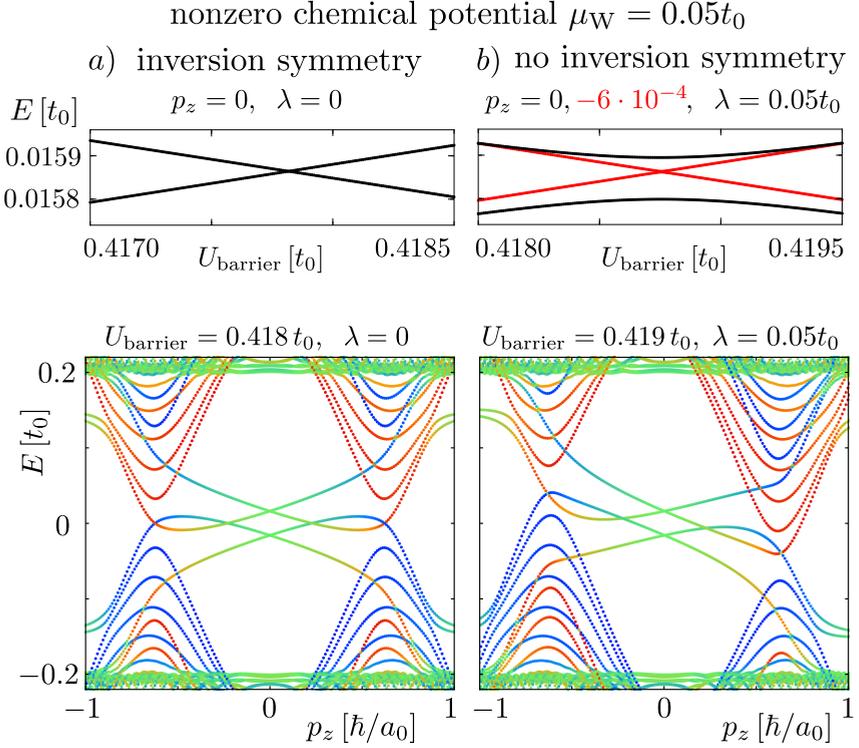
Figure 4.5: Band structure in the slab geometry, showing the level crossing near $p_z = 0$ between modes with the same connectivity index. In the lower panels we show the crossing as a function of p_z at fixed tunnel barrier height U_{barrier}, in the upper panels we show the crossing at fixed p_z as a function of U_{barrier}. The parameters and color scale are those of Fig. 4.2b, but we took a nonzero $\mu_{\text{W}} = 0.05\,t_0$ (notice the displacement of electron and hole bands in the bulk Weyl cones) in order to demonstrate that the level crossing does not require a vanishing chemical potential. The level crossing also persists if inversion symmetry is broken by a nonzero $\lambda = 0.05\,t_0$, but the crossing point is displaced away from $p_z = 0$ (compare black and red curves in panel b, at $p_z = 0$ and $p_z = -6 \cdot 10^{-4}\,\hbar/a_0$).

generically when we vary interface parameters, in Fig. 4.5 we show that it persists at nonzero chemical potential $\mu = \mu_{\mathrm{W}}$ in the Weyl semimetal[*]. Inversion symmetry breaking by a nonzero λ moves the crossing point away from $p_z = 0$, but does not destroy it. The wire geometry gives similar results, see Fig. 4.6.

To model this effect in the framework of the surface Hamiltonian (4.3), we take a momentum-independent complex off-diagonal potential $D_1 - iD_2 \equiv \Delta$ with amplitude $\Delta_0 = c(U_{\mathrm{barrier}} - U_c)$ that crosses zero at some critical barrier height U_c. Inversion symmetry imposes a definite parity on the real diagonal potential $D_3 \equiv \mu(p_z)$, such that even a small admixture of an odd-parity component enforces $\mu(0) = 0$ when $\lambda = 0$. If we take $\mu(p_z) = c'\lambda + c''p_z$ the dispersion relation (4.4) in the pair of modes with $\kappa = +1$ has the form

$$E_\nu(p_z) = D_0(p_z) + \nu\sqrt{c^2(U_{\mathrm{barrier}} - U_c)^2 + (c'\lambda + c''p_z)^2}. \qquad (4.9)$$

The dashed curves in Fig. 4.4 are fits to this functional form, with $\lambda = 0$ and a quartic $D_0(p_z)$. The qualitative behavior agrees reasonably well.

4.5 Quasiparticle trapping by gap inversion

The gap inversion of Fig. 4.4 can be used to trap a quasiparticle by varying the tunnel barrier height $U_{\mathrm{barrier}}(z)$ (by means of a variation in the thickness of the insulating layer), from a value above the critical strength U_c to a value below U_c. A demonstration of this effect in the slab geometry is shown in Fig. 4.7, where we plot the local density of states and charge polarization $\langle\psi|\nu_z|\psi\rangle\langle\psi|\psi\rangle^{-1} \in (-1, +1)$ at each site of the lattice.

In terms of the surface Hamiltonian, the quasiparticle trapping is described by the Schrödinger equation $H_\pm\psi(z) = E\psi(z)$ with

$$H_\pm = \begin{pmatrix} \pm D_0(\pm p_z) + \mu(\pm p_z) & \Delta(z) \\ \Delta^*(z) & \pm D_0(\pm p_z) - \mu(\pm p_z) \end{pmatrix}. \qquad (4.10)$$

We take a real $\Delta(z) = c(U_{\mathrm{barrier}}(z) - U_c)$ and, respectively, an even and odd p_z-dependence of D_0 and $\mu = c''p_z$ — consistent with inversion symmetry. If we neglect quadratic terms in D_0 we have a matrix differential equation of first order,

$$\mp i\hbar c''\nu_z\frac{d\psi}{dz} = \left[(E \mp D_0(0))\nu_0 - \Delta(z)\nu_x\right]\psi(z). \qquad (4.11)$$

---

[*]In figures 4.2, 4.4, and 4.7 we also added a small offset of $10^{-4}\,t_0$ to μ_{W} to break the electron-hole degeneracy.
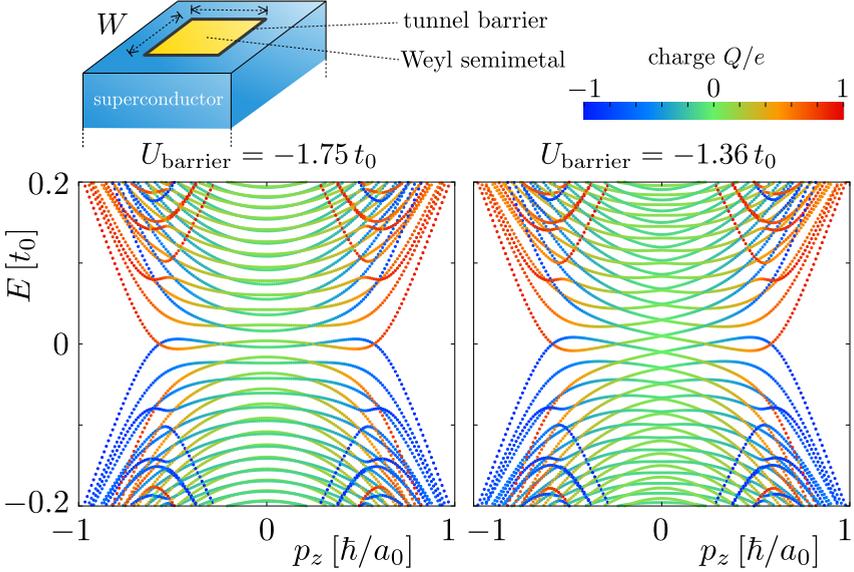
Figure 4.6: Band structure in a wire geometry (square cross section*), showing all modes in the energy range $-0.2 < E/t_0 < 0.2$. (The previous plots in the slab geometry showed only the modes with a single k_y value, but in the wire k_y is not a good quantum number.) The gap between pairs of modes in the same subband and with the same connectivity index closes at $p_z = 0$ upon variation of the tunnel barrier height.

Let $\Delta(z)/c''$ vary from a positive value for $z < 0$ and $z > L$ to a negative value in the interval $0 < z < L$. For sufficiently large L we can consider the domain wall at $z = 0$ separately from the one at $z = L$. At energy $E = \pm D_0(0)$ there is a bound state at $z = 0$ with wave function

$$\psi_\pm(z) = \exp\left(\pm\frac{1}{\hbar c''} \int_0^z dz' \, \Delta(z')\nu_y\right) \psi_\pm(0). \qquad (4.12)$$

This should be a decaying function of $|z|$, so $\psi_\pm(0) = (1, \pm i)$ is an eigenstate of ν_y with eigenvalue ± 1.

Fig. 4.7 shows that the bound state is a charge-neutral quasiparticle. There is one state at energy $+D_0(0)$ and a second state at $-D_0(0)$, but because the BdG equation doubles the spectrum only a single Majorana

---

*The microscopic model parameters in the wire geometry of Fig. 4.6 are (energies in units of t_0, lengths in units of a_0): $t = 2$, $t_z = 1$, $m_0 = -0.3$, $\lambda = 0$, $\beta = 0.6$, $\tilde{t} = 7$, $\tilde{t}_z = 3.5$, $\mu_W = 0.05$, $\mu_S = 3.5$, $\Delta_0 = 0.4$, $d_{\text{barrier}} = 1$, $W = 79$.
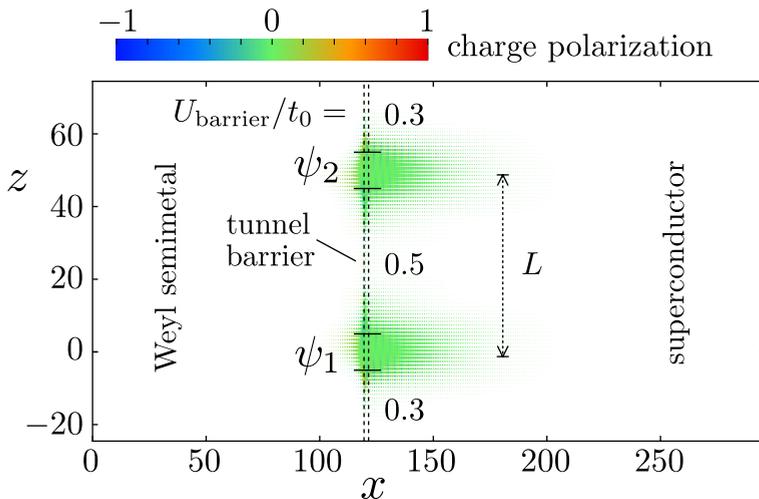
Figure 4.7: Density of states (dot size) and local charge polarization (color) at $E = 0.016\,t_0$ in an NS junction in the slab geometry* with a z-dependent tunnel barrier height. The vertical dashed lines indicate the tunnel barrier at the NS interface. The horizontal lines indicate the regions where the tunnel barrier height U_{barrier} is varied from $0.3\,t_0$ to $0.5\,t_0$ and back, passing through the critical value $U_c = 0.411\,t_0$ near $z = 0$ and $z = 50 \equiv L$. At these domain walls the gap between a pair of surface modes (at given $|k_y| = \pi/120$) closes and reopens, trapping a charge-neutral quasiparticle. The parameters are the same as in Fig. 4.4, with periodic boundary conditions in the z-direction.

fermion is trapped at $z = 0$. A second Majorana fermion is trapped at $z = L$. All of this is for a single orbital mode n. We have found numerically that the critical barrier height U_c is weakly n-dependent, so a domain wall traps one Majorana fermion per orbital subband.

4.6 Analytical mode-matching calculation

4.6.1 Hamiltonian with spatially dependent coefficients

To analytically substantiate our numerical findings we have performed a mode-matching calculation in the slab geometry of Fig. 4.1b, matching

---

*Fig. 4.7 is for an NS junction with a single interface at positive and negative $k_y = \pm\pi/120$. Figs. 4.2, 4.4, and 4.5 are for an SNS junction with two interfaces at a single $k_y = \pi/120$.

electron and hole modes in the normal (N) region $0 < x < W$ to Bogoliubov quasiparticles in the superconducting (S) regions $x < 0$, $x > W$. This procedure can be greatly simplified if we choose a single BdG Hamiltonian H with x-dependent coefficients, rather than the different H_W and H_S of Sec. 4.4 — the former choice is a less realistic model of an SNS junction than the latter, but as we will see the results are essentially equivalent.

Our starting point is therefore the Hamiltonian

$$
\begin{aligned}
H = \nu_z \tau_z (t\sigma_x \sin k_x + t\sigma_y \sin k_y + t_z \sigma_z \sin k_z) \\
+ m\nu_z \tau_x \sigma_0 + \lambda \nu_z \tau_z \sigma_0 + \beta \nu_0 \tau_0 \sigma_z \\
- \mu(x)\nu_z \tau_0 \sigma_0 + \Delta(x)\nu_x \tau_0 \sigma_0,
\end{aligned}
\tag{4.13}
$$

with chemical potential $\mu(x)$, pair potential $\Delta(x)$, and mass term

$$
m(\boldsymbol{k}) = m_0 + t(2 - \cos k_x - \cos k_y) + t_z(1 - \cos k_z). \tag{4.14}
$$

We will compare our analytical mode-matching calculation to a numerical solution of the discretized Hamiltonian (4.13). For this analytics, but not for the numerics, we make one further simplification, which is to linearize the Hamiltonian in the transverse momentum component k_x, so that the mode-matching calculation requires the solution of a set of first order differential equation in x. We thus replace $\sin k_x \mapsto k_x$ and replace the mass term (4.14) by

$$
\tilde{m}(k_y, k_z) = m_0 + t(1 - \cos k_y) + t_z(1 - \cos k_z). \tag{4.15}
$$

4.6.2 First-order decoupling of the mode-matching equations

The Schrödinger equation $H\psi = E\psi$ produces 8 coupled differential equations, and an attempt at direct solution produces unwieldy results. Our approach is to partially decouple these by suitable unitary transformations of H. We take the inversion symmetry breaking strength λ and chemical potential μ as small parameters and seek a decoupling up to corrections of first or second order in λ, μ.

For a first-order decoupling we rotate the ν_x and τ_x spinors by the unitaries

$$
U_\theta = \exp\left(\tfrac{1}{2} i\theta \nu_y \tau_z \sigma_z\right), \quad U_\phi = \exp\left(\tfrac{1}{2} i\phi \nu_0 \tau_y \sigma_z\right). \tag{4.16}
$$

The rotation angles θ, ϕ are x and k_z-dependent,

$$\cos\theta = -(t_z/\Delta_{\text{eff}})\sin k_z, \;\; \sin\theta = \Delta/\Delta_{\text{eff}}, \tag{4.17a}$$

$$\cos\phi = \Delta_{\text{eff}}/M, \;\; \sin\phi = \tilde{m}/M, \tag{4.17b}$$

$$\Delta_{\text{eff}}(x) = \sqrt{\Delta^2(x) + t_z^2\sin^2 k_z}, \tag{4.17c}$$

$$M(x) = \sqrt{\tilde{m}^2 + \Delta^2(x) + t_z^2\sin^2 k_z}. \tag{4.17d}$$

Notice that $\cos\theta \to -\text{sign}\, k_z$ for $\Delta \to 0$. We can avoid this discontinuity at $k_z = 0$ by keeping a small nonzero Δ in the normal region.

The transformed Hamiltonian,

$$
\begin{aligned}
H_{\phi,\theta} &= U_\phi^\dagger U_\theta^\dagger H U_\theta U_\phi \\
&= t\nu_z\tau_z(\sigma_x k_x + \sigma_y\sin k_y) - M\nu_z\tau_z\sigma_z + \beta\nu_0\tau_0\sigma_z + V_b(x) \\
&\quad - \mu\cos\theta\,\nu_z\tau_0\sigma_0 - \mu\sin\theta\cos\phi\,\nu_x\tau_z\sigma_z - \mu\sin\theta\sin\phi\,\nu_x\tau_x\sigma_0 \\
&\quad + \lambda\sin\theta\,\nu_x\tau_0\sigma_z + \lambda\cos\theta\cos\phi\,\nu_z\tau_z\sigma_0 + \lambda\cos\theta\sin\phi\,\nu_z\tau_x\sigma_z,
\end{aligned}
\tag{4.18}
$$

is diagonal in the ν and τ degrees of freedom up to corrections of first order in λ, μ, and up to a boundary potential $V_b(x)$ resulting from the commutator of $k_x = -i\partial/\partial x$ and the x-dependent superconducting gap $\Delta(x)$ at the NS interface. In this section we discard the boundary potential, to simplify the calculations — we will fully include it in the Appendix.

The term $\propto \mu\nu_x\tau_x\sigma_0$ in the Hamiltonian (4.18) can be made diagonal in ν and τ with the unitary transformation

$$H_{\psi,\phi,\theta} = U_\psi^\dagger P_3^\dagger H_{\phi,\theta} P_3 U_\psi, \tag{4.19a}$$

$$U_\psi = \exp(\tfrac{1}{2}i\psi\nu_0\tau_y\sigma_0), \tag{4.19b}$$

$$P_3 = \frac{1}{2}\begin{pmatrix} (\tau_0 + \tau_z)\sigma_0 & (\tau_x - i\tau_y)\sigma_0 \\ (\tau_0 - \tau_z)\sigma_0 & (\tau_x + i\tau_y)\sigma_0 \end{pmatrix}, \tag{4.19c}$$

$$\cos\psi = (1 - \sin^2\theta\cos^2\phi)^{-1/2}\cos\theta, \tag{4.19d}$$

$$\sin\psi = -(1 - \sin^2\theta\cos^2\phi)^{-1/2}\sin\phi\sin\theta. \tag{4.19e}$$

The four blocks in the shift matrix P_3 [with $(P_3)^3 = 1$] refer to the ν

degree of freedom. The transformed Hamiltonian is

$$H_{\psi,\phi,\theta} = H_{\text{diag}} + \delta H_{\text{diag}} + \delta H_{\text{offdiag}}, \tag{4.20a}$$

$$H_{\text{diag}} = t\nu_z\tau_0(\sigma_x k_x + \sigma_y \sin k_y) - M\nu_z\tau_0\sigma_z + \beta\nu_0\tau_0\sigma_z, \tag{4.20b}$$

$$\delta H_{\text{diag}} = -\mu(1 - \Delta^2/M^2)^{1/2}\nu_0\tau_z\sigma_0 - \lambda(t_z/M)\nu_z\tau_0\sigma_0 \sin k_z, \tag{4.20c}$$

$$\delta H_{\text{offdiag}} = \mu(\Delta/M)\nu_y\tau_y\sigma_z + \lambda(M^2 - \Delta^2)^{-1/2}$$
$$\times \left[\tilde{m}\nu_x\tau_z\sigma_z - (\Delta/M)t_z\nu_x\tau_x\sigma_z \sin k_z\right]. \tag{4.20d}$$

The symbol δ keeps track of the order in λ, μ of the diagonal ("diag") and off-diagonal ("offdiag") blocks.

4.6.3 Second-order decoupling via Schrieffer-Wolff transformation

The Schrieffer-Wolff transformation

$$H_{\text{SW}} = e^{i\delta S}H_{\psi,\phi,\theta}e^{-i\delta S}, \tag{4.21}$$

$$\delta S = \begin{pmatrix} 0 & \delta s \\ \delta s^\dagger & 0 \end{pmatrix} \equiv \tfrac{1}{2}(\nu_x + i\nu_y)\delta s + \tfrac{1}{2}(\nu_x - i\nu_y)\delta s^\dagger,$$

with Hermitian off-diagonal matrix δS given by

$$[\delta S, H_{\text{diag}}] = i\delta H_{\text{offdiag}}, \tag{4.22}$$

removes the off-diagonal blocks up to corrections of second order in δ:

$$H_{\text{SW}} = H_{\text{diag}} + \delta H_{\text{diag}} + \mathcal{O}(\delta^2). \tag{4.23}$$

The solution of Eq. (4.22) is*

$$\delta s = \frac{1}{2\beta M}\left[\frac{\lambda}{(M^2 - \Delta^2)^{1/2}}\left(\tilde{m}\tau_z - \frac{\Delta t_z \sin k_z}{M}\tau_x\right)\right.$$
$$\left. - \frac{\mu\Delta}{M}i\tau_y\right]\left(i\beta\sigma_0 + \sigma_y t k_x - \sigma_x t \sin k_y\right). \tag{4.24}$$

The Schrieffer-Wolff matrix δS contributes terms of order δ^2 to the energy spectrum, which is given by the eigenvalues of $H_{\text{diag}} + \delta H_{\text{diag}} + \delta H_{\text{SW}}$ with

$$\delta H_{\text{SW}} = \tfrac{1}{2}i[\delta S, \delta H_{\text{offdiag}}] + i[\delta S, \delta H_{\text{diag}}] + \mathcal{O}(\delta^3). \tag{4.25}$$

---

*To solve Eq. (4.22) for δs we substitute the block-decomposition $H_{\text{diag}} = \begin{pmatrix} h_+ & 0 \\ 0 & h_- \end{pmatrix}$, $\delta H_{\text{offdiag}} = \begin{pmatrix} 0 & \delta h \\ \delta h^\dagger & 0 \end{pmatrix}$ of the 8×8 matrices H_{diag} and $\delta H_{\text{offdiag}}$ in the ν degree of freedom. We thus arrive at the equation $\delta s h_- - h_+ \delta s = i\delta h$ involving 4×4 matrices. This Sylvester equation has a unique solution (unless h_+ and h_- have a common eigenvalue, which they do not).

4.6.4 Dispersion relation of the surface modes

The mode-matching calculation at energy E with the Hamiltonian $H_{\text{diag}} + \delta H_{\text{diag}}$ (not yet including the Schrieffer-Wolff correction) now involves four uncoupled differential equations, labeled by $\nu, \tau \in \{-1, +1\}$, for a two-component spinor $\psi(x)$:

$$t\nu \frac{d\psi}{dx} = \left[i(E + \mathcal{U})\sigma_x + t\nu\sigma_z \sin k_y + (M\nu - \beta)\sigma_y\right]\psi$$
$$\mathcal{U} = \mu\tau(1 - \Delta^2/M^2)^{1/2} + \lambda(t_z/M)\nu \sin k_z. \tag{4.26}$$

We solve this for piecewise constant coefficients. For the normal (N) region at $0 < x < W$ we choose

$$\Delta = \Delta_{\text{N}}, \ \ \mu = \mu_{\text{N}}, \tag{4.27a}$$

and for the superconducting (S) region at $x < 0$ and $x > W$ we choose

$$\Delta = \Delta_{\text{S}}, \ \ \mu = \mu_{\text{S}}, \tag{4.27b}$$

demanding continuity of $\psi(x)$ at $x = 0, W$. We keep a finite pair potential Δ_{N} in the normal region to avoid the discontinuity at $p_z = 0$ noted in Sec. 4.6.2.

To obtain the dispersion relation at a single NS interface we may take $W \to \infty$ and match decaying wave functions at both sides of the interface at $x = 0$. Such a bound surface state is possible if $M\nu - \beta$ has the opposite sign in N and S, which requires $\nu = +1$ (since β and M are both positive). We denote $M \equiv M_{\text{N}}$ in N and $M \equiv M_{\text{S}}$ in S, and similarly denote

$$\pm \mu(1 - \Delta^2/M^2)^{1/2} + \lambda(t_z/M)\sin k_z \equiv \begin{cases} \mathcal{U}_{\text{N}}^{\pm} & \text{in N}, \\ \mathcal{U}_{\text{S}}^{\pm} & \text{in S}. \end{cases} \tag{4.28}$$

The sign $\pm$ accounts for the quantum number τ in Eq. (4.26).

For a surface state we need $M_{\text{N}} - \beta < -|\mathcal{U}_{\text{N}}^{\pm}|$, $M_{\text{S}} - \beta > |\mathcal{U}_{\text{S}}^{\pm}|$ in some interval of E, k_y, k_z around zero. Solution of Eq. (4.26) gives the wave function profile

$$\psi(x) = C_{\text{N}} e^{-x\kappa_{\text{N}}^{\pm}/t} \begin{pmatrix} i\kappa_{\text{N}}^{\pm} - it \sin k_y \\ E + \mathcal{U}_{\text{N}}^{\pm} + M_{\text{N}} - \beta \end{pmatrix}, \ \ \text{for} \ \ x > 0, \tag{4.29}$$

$$\psi(x) = C_{\text{S}} e^{x\kappa_{\text{S}}^{\pm}/t} \begin{pmatrix} -i\kappa_{\text{S}}^{\pm} - it \sin k_y \\ E + \mathcal{U}_{\text{S}}^{\pm} + M_{\text{S}} - \beta \end{pmatrix}, \ \ \text{for} \ \ x < 0, \tag{4.30}$$

with inverse decay lengths

$$\kappa_{\mathrm{N,S}}^{\pm} = \sqrt{t^2 \sin^2 k_y + (M_{\mathrm{N,S}} - \beta)^2 - (E + \mathcal{U}_{\mathrm{N,S}}^{\pm})^2} \qquad (4.31)$$

on the normal and superconducting sides of the NS interface.

The amplitudes C_{N} and C_{S} are to be adjusted so that $\psi(x)$ is continuous at $x = 0$. By requiring that the matrix of coefficients of the mode-matching equations has vanishing determinant, we arrive at the dispersion relation of the surface modes,

$$E_{\pm}(k_y, k_z) = t \sin k_y + \frac{(M_{\mathrm{N}} - \beta)\mathcal{U}_{\mathrm{S}}^{\pm} - (M_{\mathrm{S}} - \beta)\mathcal{U}_{\mathrm{N}}^{\pm}}{M_{\mathrm{S}} - M_{\mathrm{N}}} + \mathcal{O}(\delta^2), \quad (4.32)$$

discarding terms of second order in μ, λ. The level crossing at $k_z = 0$, for a given k_y, happens for $m_0 = t(\cos k_y - 1)$. The corresponding charge expectation value $Q = -e\partial E/\partial \mu$ is

$$Q_{\pm} = \mp e(M_{\mathrm{S}} - M_{\mathrm{N}})^{-1}\left[(M_{\mathrm{N}} - \beta)\sqrt{1 - \Delta_{\mathrm{S}}^2/M_{\mathrm{S}}^2}\right.$$
$$\left. - (M_{\mathrm{S}} - \beta)\sqrt{1 - \Delta_{\mathrm{N}}^2/M_{\mathrm{N}}^2}\right] + \mathcal{O}(\delta), \qquad (4.33)$$

one order in μ, λ less accurate than the energy.

In Fig. 4.8 we compare the numerical diagonalization of the Hamiltonian (4.13) with the analytical mode matching calculation. Unlike the comparison in Fig. 4.4, here there is not a single fit parameter. The agreement is excellent for the energy, somewhat less for the average charge.

4.6.5 Effective surface Hamiltonian

In Sec. 4.3 we constructed an effective surface Hamiltonian by relying only on particle-hole symmetry. As an alternative route, we present here a derivation starting from the model Hamiltonian (4.20).

The motion perpendicular to the NS interface at $x = 0$ is governed by the reduced Hamiltonian

$$H_{\perp} = t\nu_z\tau_0\sigma_x k_x - M\nu_z\tau_0\sigma_z + \beta\nu_0\tau_0\sigma_z, \qquad (4.34)$$

with neglect of the terms $\propto \mu, \lambda$ as well as the k_y and k_z-dependent terms for motion parallel to the interface. The wave function profile $\psi(x)$ at $E = 0$,

$$H_{\perp}\psi = 0 \Rightarrow \psi(x) = \qquad\qquad\qquad (4.35)$$
$$\exp\left[t^{-1}\int_0^x dx'\left(M(x')\nu_0\tau_0\sigma_y - \beta\nu_z\tau_0\sigma_y\right)\right]\psi(0),$$
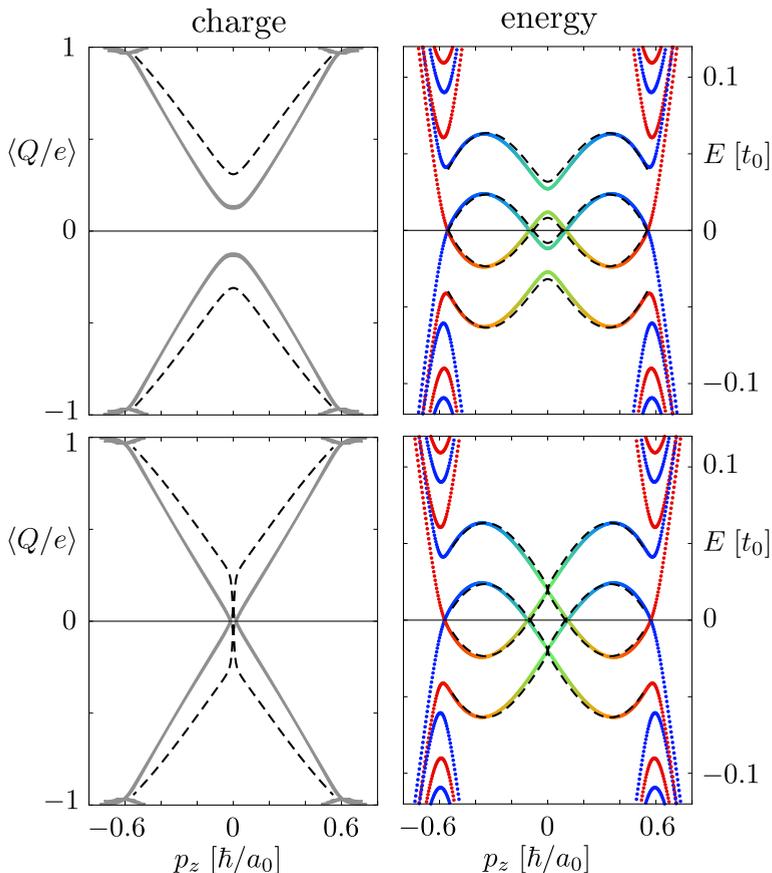
Figure 4.8: Colored data points: Energy spectrum (color scale as in Fig. 4.2) and average charge obtained from a numerical diagonalization of the discretized Hamiltonian (4.13). The top row is for $m_0 = 0.05$, the bottom row for $m_0 = 0$, other parameters: $t = 2$, $t_z = 1$, $\lambda = 0$, $\beta = 0.6$, $\mu_N = \Delta_N = 10^{-2}$, $\mu_S = 0.2$, $\Delta_S = 0.8$, $W = 120$, $k_y = 0.01$. The black dashed curves result directly from the analytical mode-matching calculation, Eqs. (4.32) and (4.33), *without any adjustable parameters.*

decays for $x \to -\infty$ (inside the superconducting region) because of the term $\propto M(-\infty) > \beta$ and for $x \to +\infty$ (inside the Weyl semimetal region) because of the term $\propto \beta > M(\infty)$. This two-sided decay is ensured if $\psi(0)$ is an eigenstate with eigenvalue $+1$ of both $\nu_0 \tau_0 \sigma_y$ and $\nu_z \tau_0 \sigma_y$. The resulting eigenspace has rank two.

The 2×2 effective surface Hamiltonian H_{eff} for motion parallel to the surface is obtained by projecting H onto this two-dimensional eigenspace, resulting in

$$H_{\text{eff}} = \tau_0 t \sin k_y - \lambda(t_z/M)\tau_0 \sin k_z$$
$$- \mu(1 - \Delta^2/M^2)^{1/2}\tau_z. \tag{4.36}$$

The corresponding charge operator is momentum dependent,

$$Q_{\text{eff}} = -e\,\partial H_{\text{eff}}/\partial\mu = e(1 - \Delta^2/M^2)^{1/2}\tau_z. \tag{4.37}$$

In this effective surface description the energy scales Δ and μ should be regarded as weighted averages of the x-dependent parameters from Eq. (4.27).

The two surface modes have opposite charge $Q_{\pm} = \pm e\,(1 - \Delta^2/M^2)^{1/2}$ and dispersion relation

$$E_{\pm}(k_z) = t \sin k_y - (\Delta^2 + \tilde{m}^2(k_y, k_z) + t_z^2 \sin^2 k_z)^{-1/2}$$
$$\times \left[\lambda t_z \sin k_z \pm \mu\sqrt{\tilde{m}^2(k_y, k_z) + t_z^2 \sin^2 k_z} \right], \tag{4.38}$$

representing the spiraling surface Fermi arc illustrated in Fig. 4.1. The $\pm$ index corresponds to the ν index of Sec. 4.3, the κ index is taken care of by the sign of $\sin k_y$. The gap $\delta E = E_+(0) - E_-(0)$ at $k_z = 0$ equals

$$\delta E = \frac{2\mu m_{\text{eff}}}{\sqrt{m_{\text{eff}}^2 + \Delta^2}}, \quad m_{\text{eff}} = |m_0 + t(1 - \cos k_y)|. \tag{4.39}$$

We interpret m_{eff} as the effective coupling strength of the surface state to the superconductor, and as the parameter that in the microscopic model of Sec. 4.4 is varied by varying U_{barrier}. The level crossing then happens when $m_{\text{eff}} = 0$. At the level crossing the excitations are charge neutral.

We may include the Schrieffer-Wolff correction, by projecting δH_{SW} from Eq. (4.25) onto the surface eigenspace. The result is a correction of order δ^2 to the effective surface Hamiltonian,

$$\delta H_{\text{eff}} = -\frac{t \sin k_y}{2\beta M^3}\left(2\mu\lambda\frac{\Delta^2\tau_z t_z \sin k_z + \Delta M\tilde{m}\tau_x}{\sqrt{M^2 - \Delta^2}} \right.$$
$$\left. + (\lambda^2\tilde{m}^2 + \lambda^2\Delta^2 + \mu^2\Delta^2)\tau_0 \right). \tag{4.40}$$

The dominant effect of this correction is to shift the level crossing away from $k_z = 0$ to $k_z = -(\lambda/\beta)(t/t_z)\sin k_y$.

4.7 Conclusion

In summary, we have investigated the superconducting proximity effect on the dispersion relation of surface modes in a Weyl-Majorana solenoid — a Weyl semimetal nanowire with an axial magnetization covered by a superconductor. The surface Fermi arc connecting bulk Weyl cones is broken up into nearly charge-neutral Majorana modes. We have identified a "connectivity index" that determines between which pair of modes a gap is opened by the superconductor.

We have discovered that the sign of the induced gap can be inverted by variation of the tunnel coupling strength between the semimetal and the superconductor. A domain wall separating segments of the nanowire with opposite sign of the gap traps a charge-neutral quasiparticle. This bound Majorana fermion is not at zero energy, so it should not be confused with the Majorana zero-modes in semiconductor nanowires [134–136]. The gap inversion is studied for a 3D model Hamiltonian, both numerically in a tight-binding formulation, and analytically via mode matching at the normal-superconductor interface. Further insight is obtained by an effective 2D surface Hamiltonian.

In closing we remark on a global aspect of the gap inversion in terms of the flow of Berry curvature (topological charge) in the Brillouin zone [137]. The minimal number of two Weyl cones in a Weyl semimetal with broken time-reversal symmetry is doubled if we include the electron-hole degree of freedom. The sign of the Berry curvature at a given point in the Brillouin zone is not changed by the doubling [70], so the Fermi arc connecting Weyl cones of opposite Berry curvature must still run across the Brillouin zone — but now it has a choice: it may connect cones of the same or opposite electrical charge. If we inspect Fig. 4.4 we see that the Fermi arcs always connect Weyl cones of the same electrical charge (coded blue or red), except at the gap inversion point. At the critical tunnel barrier height $U_{\text{barrier}} = U_c$ the Majorana surface modes connect bulk states of opposite electrical charge (from blue to red).

In Fig. 4.4 the anomalous connection by Fermi arcs of Weyl cones of opposite electrical charge and opposite topological charge happens only at an isolated point in parameter space, because the superconductivity is induced only at the surface of the Weyl semimetal. By inducing superconductivity throughout the bulk (for example, using the heterostructure approach of Ref. [70]) one should be able to stabilize the anomalous connection in an entire region of parameter space. We expect an anomalous Josephson effect to develop in the Weyl-Majorana solenoid as a result of this topologically nontrivial connection.

4.A Effect of the boundary potential on the mode-matching calculation

The unitary transformations in Sec. 4.6 introduce a boundary potential in the Hamiltonian (4.20), given by

$$
\begin{aligned}
V_b(x) = & -itU_\psi^\dagger(x)P_3^\dagger U_\phi^\dagger(x)U_\theta^\dagger(x)\nu_z\tau_z\sigma_x \left[\frac{\partial}{\partial x}, U_\theta(x)U_\phi(x)P_3U_\psi(x)\right] \\
= & \tfrac{1}{2}t(\theta'\sin\phi + \psi')\nu_z\tau_y\sigma_x - \tfrac{1}{2}t(\phi'\sin\psi + \theta'\cos\psi\cos\phi)\nu_x\tau_x\sigma_y \\
& - \tfrac{1}{2}t(\phi'\cos\psi - \theta'\sin\psi\cos\phi)\nu_x\tau_z\sigma_y \\
= & -\frac{\tfrac{1}{2}tm_z}{\Delta^2(x) + m_z^2}\frac{d\Delta(x)}{dx}\nu_x\tau_x\sigma_y,
\end{aligned}
\tag{4.41}
$$

where we abbreviated

$$
m_z = (\tilde{m}^2 + t_z^2\sin^2 k_z)^{1/2}.
\tag{4.42}
$$

For simplicity we omitted $V_b(x)$ from the mode-matching calculations and the derivation of the effective surface Hamiltonian in Sec. 4.6. In the following we include it in the calculation, resulting in an improved agreement of the analytics with the numerics but without simple closed-form expressions as Eqs. (4.32) and (4.33).

The step-function variation of the pair potential $\Delta(x)$ at the NS interfaces $x = 0, W$ produces a delta-function boundary potential. Let us focus on the interface at $x = 0$, with $\Delta = \Delta_N$ for $x > 0$ and $\Delta = \Delta_S$ for $x < 0$. Because of the boundary potential, the wave function does not vary continuously across the NS interface. Instead, the wave functions at the two sides of the interface $x = 0$ are related by the transfer matrix,

$$
\begin{aligned}
\psi(0^+) &= e^{i\mathcal{M}_{NS}}\psi(0^-), \\
\mathcal{M}_{NS} &= -\frac{1}{t}\int_{0^-}^{0^+} dx\, \nu_z\tau_0\sigma_x V_b(x) = -\tfrac{1}{2}\alpha\nu_y\tau_x\sigma_z,
\end{aligned}
\tag{4.43}
$$

where the angle α is given by the integral

$$
\alpha = \int_{\Delta_S}^{\Delta_N} d\Delta\, \frac{m_z}{\Delta^2 + m_z^2} = \arctan\frac{\Delta_N}{m_z} - \arctan\frac{\Delta_S}{m_z}.
\tag{4.44}
$$

Note that at the level crossing point we have $m_z = 0$ hence $\alpha = 0$, so the level crossing itself is not affected by the boundary potential.

As explained in Sec. 4.6.5, to obtain the effective surface Hamiltonian we impose a two-sided decay of the wave function, by demanding that ψ is an eigenstate with eigenvalue $+1$ of $\nu_0\tau_0\sigma_y$ in S and of $\nu_z\tau_0\sigma_y$ in N. The former condition can be rewritten as a boundary condition in N,

$$\psi(0^+) = U_b\psi(0^+), \quad U_b = e^{i\mathcal{M}_{\mathrm{NS}}}\nu_0\tau_0\sigma_y e^{-i\mathcal{M}_{\mathrm{NS}}}. \tag{4.45}$$

Note that U_b and $\nu_z\tau_0\sigma_y$ commute, so they can be diagonalized simultaneously. The rank two eigenspace of eigenvalue $+1$ is spanned by the vectors

$$v_1 = (0, 0, \sin\alpha, i\sin\alpha, 1 - \cos\alpha, -i + i\cos\alpha, 0, 0),$$
$$v_2 = (\sin\alpha, i\sin\alpha, 0, 0, 0, 0, 1 - \cos\alpha, -i + i\cos\alpha).$$

The Hamiltonian projected onto this eigenspace is

$$\begin{aligned}
H_{\mathrm{eff}} &= \tau_0 t\sin k_y - (\gamma/\bar{M})(\lambda\tau_0 t_z \sin k_z - \mu\tau_z m_z),\\
\gamma &= \cos\alpha + (\bar{\Delta}/m_z)\sin\alpha,
\end{aligned} \tag{4.46}$$

where the x-dependent gap $\Delta(x)$ in the full Hamiltonian has been replaced by a spatial average $\bar{\Delta}$, and $\bar{M} = (m_z^2 + \bar{\Delta}^2)^{1/2}$.

Comparison with Eq. (4.36) shows that the effect of the boundary potential is to renormalize the parameters λ and μ by a factor γ. For $\Delta_{\mathrm{S}} \gg m_z$ we have

$$\gamma = (\Delta_{\mathrm{N}}^2 + m_z^2)^{-1/2}(\Delta_{\mathrm{N}} - \bar{\Delta}). \tag{4.47}$$

The full mode-matching calculation of Sec. 4.6.4 is also modified by the new boundary condition. Since Eq. (4.43) mixes the ν and τ indices, we can no longer use the block-diagonalization of the Hamiltonian to simplify the mode matching, and we could not find a closed-form solution analogous to Eqs. (4.32) and (4.33). Including both the diagonal and off-diagonal terms in the Hamiltonian (4.20) we find the energy and charge expectation value shown in Fig. 4.9 (dashed curves). The solid curves are the numerical solution of the tight-binding model. Comparison with Fig. 4.8, where we did not include the boundary potential and discarded off-diagonal ν, τ terms in the Hamiltonian, shows little difference in the energy but an improved agreement in the charge.
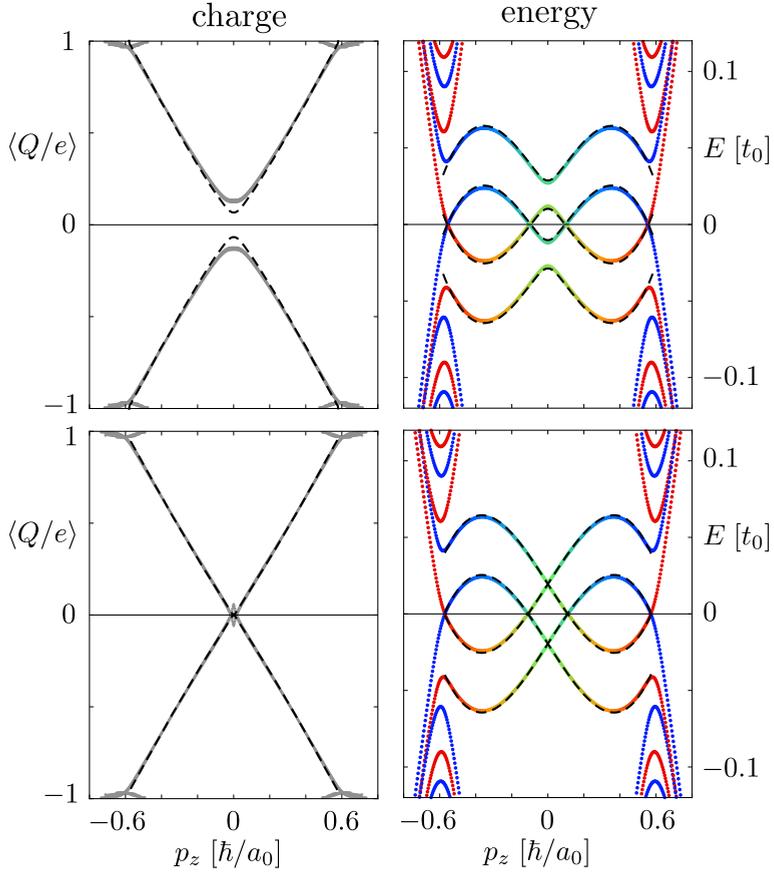
Figure 4.9: Colored data points: Energy spectrum (color scale as in Fig. 4.2) and average charge obtained from a numerical diagonalization of the discretized Hamiltonian (4.13). The parameters are the same as in Fig. 4.8. The black dashed curves result from the mode-matching calculations including the boundary potential and the full Hamiltonian (with the off-diagonal terms).

5 Andreev-Bragg reflection from an Amperian superconductor

5.1 Introduction

Doped Mott insulators exhibit new symmetry-broken states of matter with coexisting magnetic, charge, and superconducting order [138–140]. Notable examples of such "intertwined order" are superconductors with a pair-density wave (PDW), such that the Cooper pairs acquire a nonzero center-of-mass momentum [140–145]. In the first proposals by Fulde, Ferrell, Larkin, and Ovchinnikov (FFLO) the PDW order was induced by an external magnetic field [67, 146], but it can appear with preserved time-reversal symmetry in doped Mott insulators (and possibly also in a broader context [147]).

In a remarkable recent paper [68], Patrick Lee has carried this development to its logical endpoint, by proposing PDW order with the maximal $2k_{\mathrm{F}}$ Cooper pair momentum. The pairing mechanism comes from the gauge field formulation of the resonating valence bond theory of high-T_c superconductivity [138, 148–151], where electrons moving in the same direction feel an attractive force analogous to Ampère's force between current-carrying wires [152]. Lee has proposed this *Amperian pairing* to explain the diversity of anomalous properties that characterize the pseudogap phase in underdoped cuprate superconductors, including the appearance of Fermi arcs in the quasiparticle spectrum [153], charge order with a doping-dependent wave vector [154–163], and indications of short-range superconducting order [164–167].

Phase-sensitive experimental tests for Amperian pairing are hindered by phase fluctuations and the nucleation of vortex anti-vortex pairs that are believed to suppress long-range phase coherence [68]. Here we propose to use Andreev reflection as a phase-insensitive probe, which being a local process would not require long-range superconducting order. Earlier studies of the FFLO state have indicated that conductance spectroscopy shows signatures of the nonzero momentum of Cooper pairs [168–172], but these are typically small effects. We find that the extreme $2k_F$ momentum transfer upon Andreev reflection from an Amperian superconductor changes *the sign* of the current in a three-terminal configuration, allowing for an well-defined experimental test.

5.2 Model

We study the mean-field Hamiltonian

$$H = \sum_{\mathbf{k},\sigma} \xi(\mathbf{k}) c_{\mathbf{k}\sigma}^{\dagger} c_{\mathbf{k}\sigma} + \sum_{i,\mathbf{k}} \left[\Delta_{\mathbf{Q}_i}(\mathbf{k}) c_{\mathbf{k}\downarrow}^{\dagger} c_{\mathbf{Q}_i-\mathbf{k},\uparrow}^{\dagger} + \text{H.c.} \right] \tag{5.1}$$

with square-lattice dispersion

$$\begin{aligned} \xi(\mathbf{k}) &= -2t(\cos k_x + \cos k_y) - 4t' \cos k_x \cos k_y \\ &\quad - 2t''(\cos 2k_x + \cos 2k_y) - \mu \end{aligned} \tag{5.2}$$

(nearest neighbor hopping energy t, chemical potential μ, lattice constant $a \equiv 1$). To make contact with the cuprate superconductor $\text{Bi}_{2+x}\text{Sr}_{2-y}\text{CuO}_{6+\delta}$ (Bi2201), we have also included further-neighbor hopping energies $t' = -0.2\,t$ and $t'' = 0.05\,t$ [161].

The PDW order parameter $\Delta_{\mathbf{Q}_i}(\mathbf{k})$ describes pairing with total momentum $\mathbf{Q}_i = 2\mathbf{K}_i$ (up to a reciprocal lattice vector) near the points $\mathbf{K}_i \in \{\pm\mathbf{K}_x, \pm\mathbf{K}_y\}$ where the free-fermion Fermi surface crosses the boundary of the first Brillouin zone (see Fig. 5.1b). This pairing of electrons on the same side of the Fermi surface defines the Amperian superconductor [68].

Following Lee [68], we take a phenomenological Gaussian profile (width k_0) for the $\mathbf{k}$-dependence of the order parameter near the momenta $\mathbf{K}_i$ and their images upon translation by a reciprocal lattice vector $2\pi\mathbf{j} = 2\pi(n, m)$, $n, m \in \mathbb{Z}$:

$$\Delta_{\mathbf{Q}_i}(\mathbf{k}) = \frac{\Delta_0}{C} \sum_{\mathbf{j}} \exp\left(-\frac{|\mathbf{k} - \mathbf{K}_i - 2\pi\mathbf{j}|^2}{2k_0^2} \right). \tag{5.3}$$

a)

b)
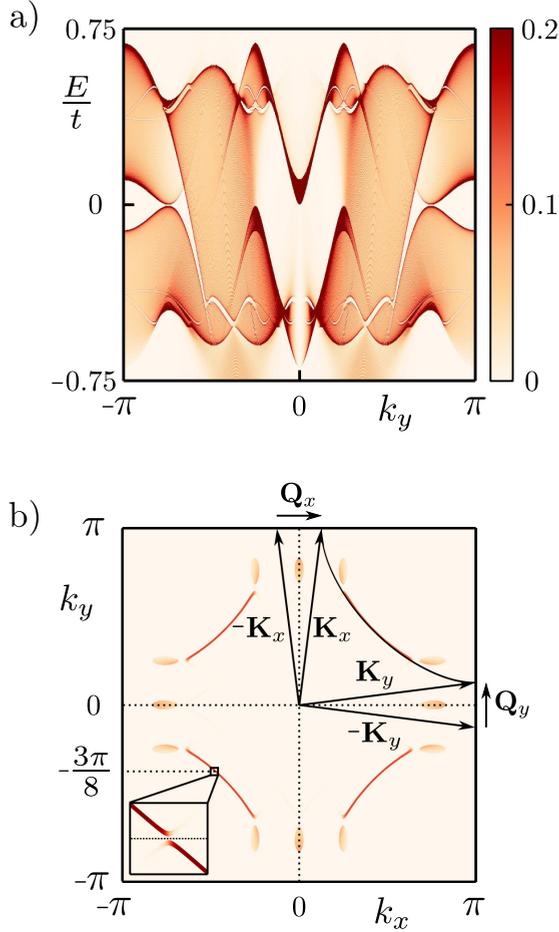
Figure 5.1: *a)* Density of states $\rho(E, \boldsymbol{k})$ as a function of energy E and momentum k_y integrated over $k_x \in (-\pi, \pi)$. Only the electron contribution is shown (in units of $1/t$), the full density of states also includes the hole contribution $\rho(-E, -\boldsymbol{k})$ to ensure particle-hole symmetry. *b)* Density of states as a function of k_x and k_y, integrated over a narrow energy interval around the Fermi level $E = 0$. The Amperian pairing takes place near the momenta $\pm\boldsymbol{K}_x$ and $\pm\boldsymbol{K}_y$ where the free-electron Fermi surface crosses the boundary of the first Brillouin zone (black arc and arrows). The PDW with wave vector $\pm\boldsymbol{Q}_x$ or $\pm\boldsymbol{Q}_y$ has a periodicity of 8 unit cells. This folds the Brillouin zone, but for clarity the figure shows the bands unfolded (extended zone scheme). Inset: Magnified region of the Brillouin zone near $k_y = -3\pi/8$, showing a minigap.

By choosing the coefficient C such that $\Delta_{\boldsymbol{Q}_i}(\boldsymbol{K}_i) = \Delta_0$, the usual BCS order parameter follows in the limit $k_0 \to \infty$ at $\boldsymbol{K}_i = 0$. In what follows we set $\Delta_0 = 0.4\,t$ and $k_0 = 1.2$.

We take chemical potential $\mu = -0.75\,t$ corresponding to hole doping fraction $p \approx 0.14$ deep inside the pseudogap phase [138]. The wave vectors $\boldsymbol{Q}_i$ for this doping are $\pm Q_0 \hat{\boldsymbol{e}}_x$ and $\pm Q_0 \hat{\boldsymbol{e}}_y$ with $Q_0 = \pi/4$, corresponding to a PDW periodicity of 8 square-lattice unit cells.

5.3 Density of states

To prepare for the calculation of the Andreev reflection probability at a normal-superconductor interface, we have first computed the electron density of states in the unbounded superconductor. We use the KWANT toolbox for all our tight-binding calculations [93]. The result in Fig. 5.1 shows the characteristic features of an Amperian superconductor identified by Lee [68]: Fermi arcs and gaps both above and below the Fermi level, in good agreement with experimental data from angle-resolved photoemission spectroscopy (ARPES) [153, 161] and scanning tunneling microscopy [157]. Close inspection reveals that the Fermi arcs are interrupted by a multitude of minigaps (cf. inset of Fig. 5.1b), originating from higher order Bragg reflection processes with a momentum shift $\sum_i n_i \mathbf{Q}_i$ ($n_i \in \mathbb{Z}$). Lifetime broadening would presumably hide these minigaps from ARPES measurements.

5.4 Andreev-Bragg reflection

We now introduce an interface with a normal metal along the line $x = 0$, extended in the y-direction over 256 lattice sites with periodic boundary conditions. The Amperian superconductor is at $x > 0$, with Hamiltonian (5.1), while for the normal metal at $x < 0$ we take a nearest-neighbor tight-binding Hamiltonian (same a and t, $\mu = -0.5\,t$, $\Delta_0 = 0$, $t' = t'' = 0$). We adopt the so-called maximum contact boundary conditions of Ref. [170], whereby the periodic modulation of the order parameter in the x-direction has a maximum at the $x = 0$ interface.

We inject an electron with energy E and transverse momentum k_y^{in} from the normal metal towards the superconductor and calculate the probability $R(E, k_y^{\mathrm{in}}, k_y^{\mathrm{out}})$ for Andreev reflection as a hole with transverse momentum
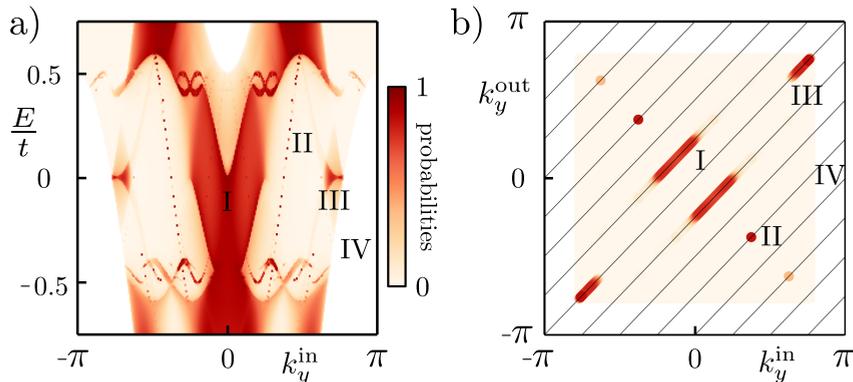
Figure 5.2: *a)* Total Andreev reflection probability (5.4) as a function of energy E and incoming transverse momentum k_y^{in}, integrated over the outgoing transverse momenta k_y^{out}. The regions of non-zero R_{tot} correspond to the gapped regions in Fig. 5.1. *b)* Andreev reflection probability at $E = 0$ as a function of incoming and outgoing transverse momenta. The diagonal black lines correspond to momentum shifts $k_y^{\text{out}} = k_y^{\text{in}} + nQ_0$, $n \in \mathbb{Z}$. Region I around $E = 0$ and $k_y^{\text{in}} = 0$ exhibits Andreev-Bragg reflection with transverse momentum shift Q_0 between the incoming electron and the outgoing hole. Region II shows transverse momentum shifts of $3Q_0$. (The resonance lines labeled II in panel *a* are interrupted by the finite k_y resolution.) Region III supports Andreev retroreflection (without transverse momentum shift), because the periodic modulation of the order parameter is perpendicular to the normal-superconductor interface. Region IV (white) has no incoming electron modes from the normal metal.

k_y^{out}. Fig. 5.2*a* shows the total Andreev reflection probability

$$R_{\text{tot}}(E, k_y^{\text{in}}) = \int_{-\pi}^{\pi} dk_y^{\text{out}} \, R(E, k_y^{\text{in}}, k_y^{\text{out}}), \tag{5.4}$$

while Fig. 5.2*b* shows how the probability at the Fermi-level $R(0, k_y^{\text{in}}, k_y^{\text{out}})$ varies as a function of incoming and outgoing transverse momenta.

As can be seen in Fig. 5.2*a*, there are distinct regions I, II, III of nonzero R_{tot}, each with a gapped density of states (cf. Fig. 5.1*a*). The corresponding Andreev reflection processes can be understood by recalling that the Amperian superconductor is described by a bi-directional (checkerboard) modulation of the order parameter with periodicity $2\pi/Q_0$ along both the x- and y-directions. Since the interface is parallel to the y-direction the modulation along x gives rise to usual Andreev retroreflection without a
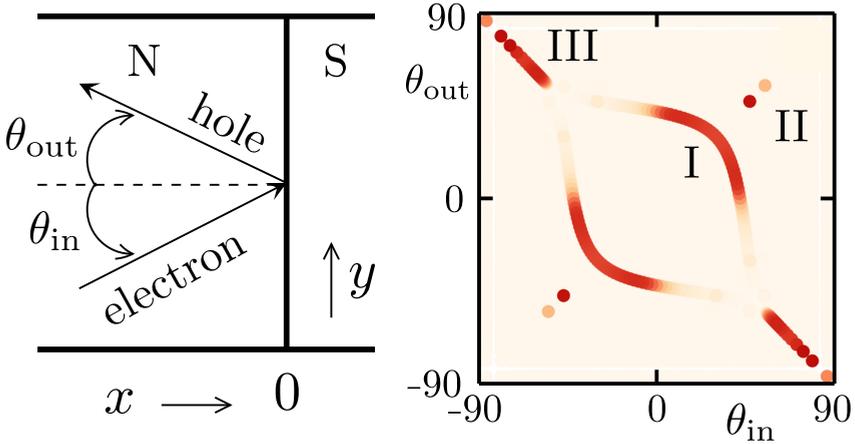
Figure 5.3: Right panel: Same as Fig. 5.2b, but now as a function of angles θ of velocities (measured in degrees) rather than transverse momentum k_y. The left panel indicates the geometry of the normal-superconductor (NS) interface, with retroreflection corresponding to $\theta_{\mathrm{out}} = -\theta_{\mathrm{in}}$ and specular reflection to $\theta_{\mathrm{out}} = \theta_{\mathrm{in}}$.

momentum shift (region III). In contrast, the modulation along y produces Andreev-Bragg reflection with transverse momentum shift nQ_0 ($n \in 2\mathbb{Z}+1$). The order $n = \pm 1$ and $n = \pm 3$ processes are visible in Fig. 5.2b, in regions I and II, respectively. Momentum shifts at even multiples of Q_0 do not appear, because these produce only normal reflection (without electron-to-hole conversion).

The angular dependence in real space of the Andreev reflection processes of type I, II, and III is shown in Fig. 5.3. The directionality of Andreev-Bragg reflection is centered around specular reflection ($\theta_{\mathrm{in}} = \theta_{\mathrm{out}}$), with a broad spread of angles for the first-order Bragg shift (type I) and a narrow collimation for higher orders (type II). The conventional Andreev retroreflection (type III, $\theta_{\mathrm{in}} = -\theta_{\mathrm{out}}$) appears only near grazing incidence.

5.5 Method of detection

Electrical detection of momentum transfer upon Andreev reflection has been proposed in the context of FFLO superconductors, notably using a magnetic-flux controlled interferometer [172]. (A similar Aharonov-Bohm interferometer has been proposed [173] to detect specular Andreev reflection in graphene [174].) Here we investigate an alternative electrical
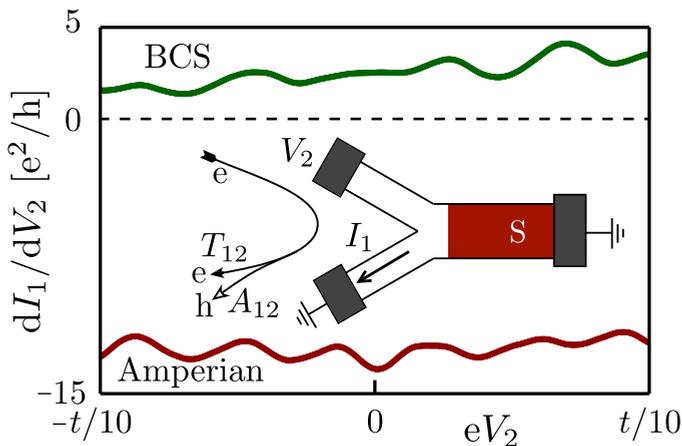
Figure 5.4: Computer simulation of the differential cross-conductance for the Y-junction geometry shown in the inset. The sign of the cross-conductance $dI_1/dV_2 \propto T_{12} - A_{12}$ distinguishes Amperian pairing ($A_{12} > T_{12}$) from BCS pairing ($T_{12} > A_{12}$).

method of detection of Andreev-Bragg reflection that relies on ballistic transport, but does not require long-range phase coherence and might therefore be more easily realized.

We consider the three-terminal Y-junction of Fig. 5.4 (inset), similar to geometries considered for the detection of "Cooper pair splitting" [175]. One difference with those experiments is that here the size of the junction is much larger than the superconducting coherence length (which is on the order of a few lattice constants). The current I_1 flowing into the grounded normal-metal contact 1 is measured while the other normal-metal contact 2 is biased at voltage V_2. (The superconductor is also grounded*.) The differential cross-conductance dI_1/dV_2 is expressed by a three-terminal

---

*The geometry of Fig. 5.4 describes a *three-terminal* differential conductance measurement, so no $\pm V_2$ symmetry is enforced. Asymmetry in the electron band structure around the Fermi level shows up in the T_{12} contribution of Eq. (5.5), but has no effect on the A_{12} contribution. This explains why the differential conductance in Fig. 5.4 has a stronger $\pm V_2$ asymmetry for BCS pairing than for Amperian pairing. We also note in this connection that the two grounded terminals in Fig. 5.4 may alternatively be biased at some nonzero potential —- the differential conductance dI_1/dV_2 remains the same because the contributions from different terminals are additive if we remain close to equilibrium (when electron heating effects can be neglected).
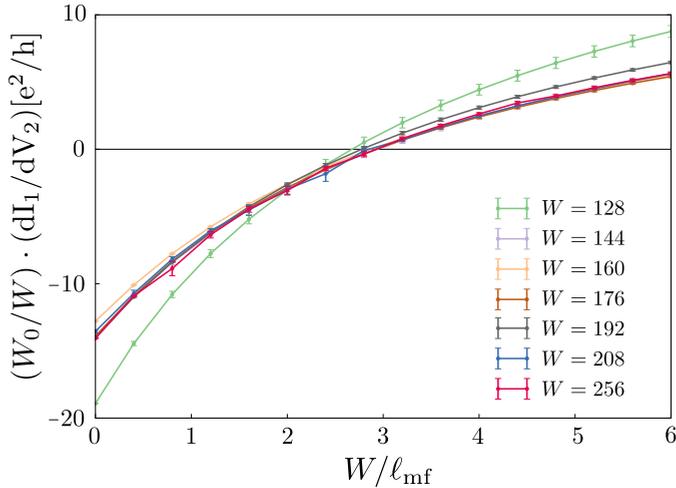
Figure 5.5: Effect of disorder on the cross-conductance of Fig. 5.4, for Amperian pairing at $V_2 = 0$. The data is averaged over four disorder realizations (error bars show standard error of the mean). Data collapse for different system widths W is achieved by rescaling the conductance by a factor W_0/W, with $W_0 = 256$. The negative cross-conductance persists for $W/\ell_{\mathrm{mf}} \lesssim 2$.

variation of the Blonder-Tinkham-Klapwijk formula [176],

$$\frac{dI_1}{dV_2} = \frac{2e^2}{h} \int_{-\infty}^{\infty} dE \left[T_{12}(E) - A_{12}(E) \right] \frac{df(E - eV_2)}{-dE}, \qquad (5.5)$$

in terms of the probabilities (summed over all transverse modes) for an electron to be transmitted from contact 2 into contact 1, either as an electron (normal transmission probability T_{12}) or as a hole (crossed Andreev reflection probability A_{12}). The probabilities are integrated over energy E, weighted by the derivative of the Fermi distribution $f(E) = (e^{\beta E} + 1)^{-1}$.

We have performed computer simulations to determine whether such a device has sufficient angular resolution to distinguish Andreev-Bragg reflection from the usual retroreflection. We took a $60°$ angle between the two normal-metal leads, each 146 lattice constants wide, with open boundary conditions. The conductance was calculated from Eq. (5.5) at a temperature of $0.01 \Delta_0$. We compared Amperian pairing with BCS pairing, keeping all other parameters of the tight-binding Hamiltonian the same.

The results plotted in Fig. 5.4 demonstrate that for a large range of voltages the differential cross-conductance is negative in the Amperian case
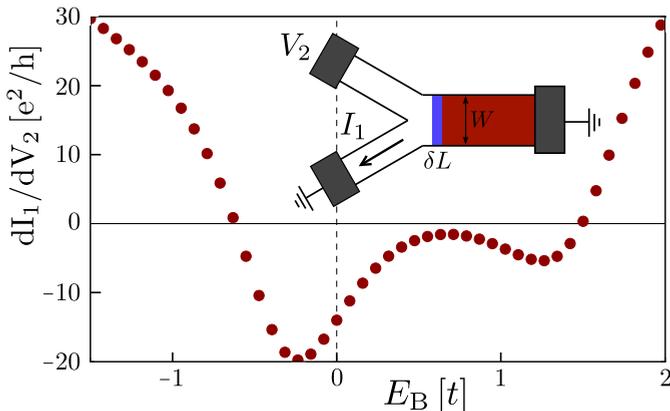
Figure 5.6: Effect of an interface barrier (height E_B, length $\delta L = 3$, width $W = 256$) on the cross-conductance of Fig. 5.4, for Amperian pairing at $V_2 = 0$. The sign changes occur when the average normal-state transmission probabilities of the barrier are $T_B = 0.68$ ($E_B = -0.63\,t$) and $T_B = 0.50$ ($E_B = 1.5\,t$). The T_B's are calculated by averaging over all the incoming modes at different energies, weighted with the Fermi distribution.

($A_{12} > T_{12}$, because Andreev-Bragg reflection dominates) and positive in the BCS case ($T_{12} > A_{12}$, because retroreflection dominates). Notice that an entirely normal system would have $A_{12} \equiv 0$, hence $dI_1/dV_2 > 0$ — so the negative cross-conductance can only originate from Andreev reflection.

5.6 Effects of disorder and interface barrier

Because the negative cross-conductance is a ballistic effect, strong impurity scattering will obscure it, but the sign change should persist if the mean free path ℓ_{mf} is not much smaller than the width W of the junction. To confirm this, we model electrostatic disorder by a random on-site energy with a Gaussian distribution with variance σ^2, resulting in $\ell_{mf} = \hbar v_F (2\pi N_0 \sigma^2)^{-1} \approx 0.9(t/\sigma)^2$. (We have used that the metallic part of the Y-junction has a nearly circular Fermi surface, with density of states per spin N_0.) Results shown in Fig. 5.5 confirm our expectation.

Another detrimental effect is the presence of a barrier at the interface with the superconductor, since this would suppress Andreev reflection in favor of normal reflection. The computer simulation of Fig. 5.6 shows that the effect of a tunnel barrier has a significant electron-hole asymmetry,

but eventually for barrier heights $|E_B| \gtrsim t$ the negative cross-conductance disappears. A high quality interface is therefore needed.

5.7 Conclusion

We have shown that Andreev reflection from an Amperian superconductor involves a transverse momentum transfer of odd multiples of $Q_0 = 2k_F$, because of Bragg scattering from the pair-density wave. Computer simulations show that this Andreev-Bragg reflection can be detected in a Y-junction, through a sign change of the differential cross-conductance. Long-range phase coherence is likely to be absent in the Amperian superconductor [68], but since Andreev reflection is a local process we expect the predicted experimental signature of the $2k_F$ pairing to be robust and accessible.

The experimental signature of Andreev-Bragg reflection proposed here may for example be observed in $Bi_2Sr_2CaCu_2O_{8+x}$, where recent experiments have shown evidence for the excistence of a pair density wave using scanned Josephson tunnelling microscopy [177]. Beyond that, the signature may be of use in other contexts as well. The pair-density waves predicted in Mott insulators [140] have crystal momentum on the order of the inverse lattice constant, and might therefore be detected via a negative cross-conductance in the geometry of Fig. 5.4. Ultracold fermionic atoms in a two-dimensional optical lattice provide an altogether different realization of the Hubbard model [178]. Thus, these systems may also support PDW states, which can potentially be detected via Andreev-Bragg reflections. An energy-resolved scattering experiment is challenging in that context, but in the light of the recent observation of conductance quantization in a cold atom setup [179], the analogue of negative cross-conductance may become observable as well.

Bibliography

[1] D. J. Thouless, M. Kohmoto, M. P. Nightingale, and M. den Nijs. *Quantized Hall Conductance in a Two-Dimensional Periodic Potential.* Phys. Rev. Lett. **49**, 405 (1982).

[2] B. I. Halperin. *Quantized Hall conductance, current-carrying edge states, and the existence of extended states in a two-dimensional disordered potential.* Phys. Rev. B **25**, 2185 (1982).

[3] Y. Hatsugai. *Edge states in the integer quantum Hall effect and the Riemann surface of the Bloch function.* Phys. Rev. B **48**, 11851 (1993).

[4] Y. Hatsugai. *Chern number and edge states in the integer quantum Hall effect.* Phys. Rev. Lett. **71**, 3697 (1993).

[5] B. A. Bernevig, T. L. Hughes, and S.-C. Zhang. *Quantum Spin Hall Effect and Topological Phase Transition in HgTe Quantum Wells.* Science **314**, 1757 (2006).

[6] M. König, S. Wiedmann, C. Brüne, A. Roth, H. Buhmann, L. W. Molenkamp, X.-L. Qi, and S.-C. Zhang. *Quantum Spin Hall Insulator State in HgTe Quantum Wells.* Science **318**, 766 (2007).

[7] C. L. Kane and E. J. Mele. *Quantum Spin Hall Effect in Graphene.* Phys. Rev. Lett. **95**, 226801 (2005).

[8] L. Fu, C. L. Kane, and E. J. Mele. *Topological Insulators in Three Dimensions.* Phys. Rev. Lett. **98**, 106803 (2007).

[9] J. E. Moore, and L. Balents. *Topological invariants of time-reversal-invariant band structures.* Phys. Rev. B **75**, 121306 (2007).

[10] X. Wan, A. M. Turner, A. Vishwanath, and S. Y. Savrasov. *Topological semimetal and Fermi-arc surface states in the electronic structure of pyrochlore iridates.* Phys. Rev. B **83**, 205101 (2011).

[11] A. A. Burkov, and L. Balents. *Weyl Semimetal in a Topological Insulator Multilayer.* Phys. Rev. Lett. **107**, 127205 (2011).

Bibliography

[12] A.A. Burkov, M.D. Hook, and L. Balents. *Topological nodal semimetals.* Phys. Rev. B **84**, 235126 (2011).

[13] A. A. Zyuzin, S. Wu, and A. A. Burkov. *Weyl semimetal with broken time reversal and inversion symmetries.* Phys. Rev. B **85**, 165110 (2012).

[14] K. Sun, W.V. Liu, A. Hemmerich, and S. Das Sarma. *Topological semimetal in a fermionic optical lattice.* Nat. Phys. **8**, 67 (2012).

[15] J.-H. Jiang. *Tunable topological Weyl semimetal from simple-cubic lattices with staggered fluxes.* Phys. Rev. A **85**, 033640 (2012).

[16] P. Hosur, S.A. Parameswaran, and A. Vishwanath. *Charge Transport in Weyl Semimetals.* Phys. Rev. Lett. **108**, 046602 (2012).

[17] P. Delplace, J. Li, and D. Carpentier. *Topological Weyl semi-metal from a lattice model.* EPL **97**, 67004 (2012).

[18] A. M. Turner and A. Vishwanath. *Beyond Band Insulators: Topology of Semimetals and Interacting Phases.* Contemporary Concepts of Condensed Matter Science **6**, 293 (Elsevier 2013).

[19] I. C. Fulga, F. Hassler, and A. R. Akhmerov. *Scattering theory of topological insulators and superconductors.* Phys. Rev. B **85**, 165409 (2012).

[20] S. Rao. *Weyl semi-metals : a short review.* J. Indian Inst. Sci. **96**, 145 (2016).

[21] A.A. Burkov. *Topological semimetals.* Nat. Mater. **15**, 1145 (2016).

[22] S. Jia, S.-Y. Xu, and M. Z. Hasan. *Weyl semimetals, Fermi arcs and chiral anomalies.* Nat. Mater. **15**, 1140 (2016).

[23] O. Klein. *Die Reflexion von Elektronen an einem Potentialsprung nach der relativistischen Dynamik von Dirac.* Z. Phys. **53**, 157 (1929).

[24] V. V. Cheianov, and V. I. Fal'ko. *Selective transmission of Dirac electrons and ballistic magnetoresistance of $n-p$ junctions in graphene.* Phys. Rev. B **74**, 041403 (2006).

[25] M. I. Katsnelson, K. S. Novoselov, and A. K. Geim. *Chiral tunnelling and the Klein paradox in graphene.* Nat. Phys. **2**, 620 (2006).

[26] M. M. Vazifeh and M. Franz. *Electromagnetic response of Weyl semimetals.* Phys. Rev. Lett. **111**, 027201 (2013).

[27] X.-L. Qi, T. L. Hughes, and S.-C. Zhang. *Topological field theory of time-reversal invariant insulators.* Phys. Rev. B **78**, 195424 (2008).

[28] S. Ryu, A. P. Schnyder, A. Furusaki, and A. W. W. Ludwig. *Topological insulators and superconductors: tenfold way and dimensional hierarchy.* New J. Phys. **12**, 065010 (2010).

[29] S. Murakami. *Phase transition between the quantum spin Hall and insulator phases in 3D: emergence of a topological gapless phase.* New J. Phys. **9**, 356 (2007).

[30] J.W. McClure. *Diamagnetism of Graphite.* Phys. Rev. **104**, 666 (1956).

[31] H. B. Nielsen and M. Ninomiya. *The Adler-Bell-Jackiw anomaly and Weyl fermions in a crystal.* Phys. Lett. B **130**, 389 (1983).

[32] A.A. Zyuzin and A.A. Burkov. *Thin topological insulator film in a perpendicular magnetic field.* Phys. Rev. B **83**, 195413 (2011).

[33] A. H. Castro Neto, F. Guinea, N. M. R. Peres, K. S. Novoselov, and A. K. Geim. *The electronic properties of graphene.* Rev. Mod. Phys. **81**, 109 (2009)

[34] P. E. C. Ashby and J. P. Carbotte. *Magneto-optical conductivity of Weyl semimetals.* Phys. Rev. B **87**, 245131 (2013).

[35] S. L. Adler. *Axial-vector vertex in spinor electrodynamics.* Phys. Rev. **177**, 2426 (1969).

[36] J. S. Bell and R. Jackiw. *A PCAC puzzle: $\pi^0 \to \gamma\gamma$ in the σ-model.* Nuovo Cim. A **60**, 47 (1969).

[37] R. Jackiw. *Fractional charge and zero modes for planar systems in a magnetic field.* Phys. Rev. D **29**, 2375 (1984).

[38] G. Semenoff. *Condensed-matter simulation of a three-dimensional anomaly.* Phys. Rev. Lett. **53**, 2449 (1984).

[39] A. A. Burkov. *Chiral anomaly and diffusive magnetotransport in Weyl metals.* Phys. Rev. Lett. **113**, 247203 (2014).

[40] A. A. Burkov. *Negative longitudinal magnetoresistance in Dirac and Weyl metals.* Phys. Rev. B **91**, 245157 (2015).

[41] E. V. Gorbar, V. A. Miransky and I. A. Shovkovy. *Chiral anomaly, dimensional reduction, and magnetoresistivity of Weyl and Dirac semimetals.* Phys. Rev. B **89**, 085126 (2014).

[42] A. A. Zyuzin and A. A. Burkov. *Topological response in Weyl semimetals and the chiral anomaly.* Phys. Rev. B **86**, 115133 (2012).

[43] D. T. Son and N. Yamamoto. *Berry curvature, triangle anomalies, and the chiral magnetic effect in Fermi liquids.* Phys. Rev. Lett. **109**, 181602 (2012).

[44] Y. Chen, S. Wu, and A. A. Burkov. *Axion response in Weyl semimetals.* Phys. Rev. B **88**, 125105 (2013).

[45] P. Goswami and S. Tewari. *Axionic field theory of (3+1)-dimensional Weyl semimetals.* Phys. Rev. B **88**, 245107 (2013).

[46] P. Baireuther, J.A. Hutasoit, J. Tworzydło, C.W.J. Beenakker. *Scattering theory of the chiral magnetic effect in a Weyl semimetal: interplay of bulk Weyl cones and surface Fermi arcs.* New J. Phys. **18**, 045009 (2016).

[47] P. Hosur. *Friedel oscillations due to Fermi arcs in Weyl semimetals.* Phys. Rev. B **86**, 195102 (2012).

[48] S.-Y. Xu, I. Belopolski, N. Alidoust, M. Neupane, G. Bian, C. Zhang, R. Sankar, G. Chang, Z. Yuan, C.-C. Lee, S.-M. Huang, H. Zheng, J. Ma, D. S. Sanchez, B. Wang, A. Bansil, F. Chou, P. P. Shibayev, H. Lin, S. Jia, M. Z. Hasan. *Discovery of a Weyl fermion semimetal and topological Fermi arcs.* Science **349**, 613 (2015).

[49] B. Q. Lv, H. M. Weng, B. B. Fu, X. P. Wang, H. Miao, J. Ma, P. Richard, X. C. Huang, L. X. Zhao, G. F. Chen, Z. Fang, X. Dai, T. Qian, and H. Ding. *Experimental Discovery of Weyl Semimetal TaAs.* Phys. Rev. X **5**, 031013 (2015).

[50] B. Q. Lv, N. Xu, H. M. Weng, J. Z. Ma, P. Richard, X. C. Huang, L. X. Zhao, G. F. Chen, C. E. Matt, F. Bisti, V. N. Strocov, J. Mesot, Z. Fang, X. Dai, T. Qian, M. Shi, and H. Ding. *Observation of Weyl nodes in TaAs.* Nat. Phys. **11**, 724 (2015).

[51] L. X. Yang, Z. K. Liu, Y. Sun, H. Peng, H. F. Yang, T. Zhang, B. Zhou, Y. Zhang, Y. F. Guo, M. Rahn, D. Prabhakaran, Z. Hussain, S.-K. Mo, C. Felser, B. Yan, and Y. L. Chen. *Weyl semimetal phase in the non-centrosymmetric compound TaAs.* Nat. Phys. **11**, 728 (2015).

[52] S.-Y. Xu, N. Alidoust, I. Belopolski, Z. Yuan, G. Bian, T.-R. Chang, H. Zheng, V. N. Strocov, D. S. Sanchez, G. Chang, C. Zhang, D. Mou, Y. Wu, L. Huang, C.-C. Lee, S.-M. Huang, B. Wang, A. Bansil, H.-T. Jeng, T. Neupert, A. Kaminski, H. Lin, S. Jia, M. Z. Hasan. *Discovery of a Weyl fermion state with Fermi arcs in niobium arsenide.* Nat. Phys. **11**, 748 (2015).

[53] S.-Y. Xu, I. Belopolski, D. S. Sanchez, C. Zhang, G. Chang, C. Guo, G. Bian, Z. Yuan, H. Lu, T.-R. Chang, P. P. Shibayev, M. L. Prokopovych, N. Alidoust, H. Zheng, C.-C. Lee, S.-M. Huang, R. Sankar, F. Chou, C.-H. Hsu, H.-T. Jeng, A. Bansil, T. Neupert, V. N. Strocov, H. Lin, S. Jia, and M. Z. Hasan. *Experimental discovery of a topological Weyl semimetal state in TaP.* Science Adv. **1**, 1501092 (2015).

[54] G. Xu, H. Weng, Z. Wang, X. Dai, and Z. Fang. *Chern Semimetal and the Quantized Anomalous Hall Effect in $HgCr_2Se_4$.* Phys. Rev. Lett. **107**, 186806 (2011).

[55] D. Bulmash, C.-X. Liu, and X.-L. Qi. *Prediction of a Weyl semimetal in $Hg_{1-x-y}Cd_xMn_yTe$.* Phys. Rev. B **89**, 081106 (2014).

[56] A.F. Andreev. *Thermal conductivity of the intermediate state of superconductors.* Sov. Phys. JETP **19**, 1228 (1964).

[57] P. G. De Gennes, D. Saint-James. *Elementary excitations in the vicinity of a normal metal-superconducting metal contact.* Phys. Lett. **4**, 151 (1963).

[58] M. Tinkham. *Introduction to Superconductivity.* (second ed.) (Dover 2012).

[59] C. W. J. Beenakker. *Three "universal" mesoscopic Josephson effects.* Springer Ser. Solid-State Sci. **109**, 235 (1992).

[60] T. M. Klapwijk. *Proximity effect from an Andreev perspective.* J. Supercond. **17**, 593 (2004).

[61] W. Belzig, F. K. Wilhelm, C. Bruder, G. Schön, and A. D. Zaikin., *Quasiclassical Green's function approach to mesoscopic superconductivity.* Superlattices and Microstructures **25**, 1251 (1999).

[62] Y. Matsuda, and H. Shimahara. *Fulde-Ferrell-Larkin-Ovchinnikov State in Heavy Fermion Superconductors.* J. Phys. Soc. Jpn. **76**, 051005 (2007).

[63] T. Terashima, K. Kihou, M. Tomita, S. Tsuchiya, N. Kikugawa, S. Ishida, C.-H. Lee, A. Iyo, H. Eisaki, and S. Uji. *Hysteretic superconducting resistive transition in $Ba_{0.07}K_{0.93}Fe_2As_2$*. Phys. Rev. B **87**, 184513 (2013).

[64] P. Burger, F. Hardy, D. Aoki, A. E. Böhmer, R. Eder, R. Heid, T. Wolf, P. Schweiss, R. Fromknecht, M. J. Jackson, C. Paulsen, and C. Meingast. *Strong Pauli-limiting behavior of H_{c2} and uniaxial pressure dependencies in KFe_2As_2*. Phys. Rev. B **88**, 014517 (2013).

[65] D. A. Zocco, K. Grube, F. Eilers, T. Wolf, and H. v. Löhneysen. *Pauli-Limited Multiband Superconductivity in KFe_2As_2*. Phys. Rev. Lett. **111**, 057007 (2013).

[66] A. I. Larkin, Y.N. Ovchinnikov. *Nonuniform state of superconductors.* Sov. Phys. JETP **20**, 762 (1965).

[67] P. Fulde and R. A. Ferrell. *Superconductivity in a strong spin-exchange field.* Phys. Rev. **135**, A550 (1964).

[68] P. A. Lee. *Amperean pairing and the pseudogap phase of cuprate superconductors.* Phys. Rev. X **4**, 031017 (2014).

[69] A. Chen and M. Franz, *Superconducting proximity effect and Majorana flat bands in the surface of a Weyl semimetal*, Phys. Rev. B **93**, 201105 (2016).

[70] T. Meng and L. Balents, *Weyl superconductors*, Phys. Rev. B **86**, 054504 (2012).

[71] P. Baireuther, J. Tworzydło, M. Breitkreiz, I. Adagideli, C.W.J. Beenakker. *Weyl-Majorana solenoid.* New J. Phys. **19**, 025006 (2017)

[72] R. S. K. Mong, A. M. Essin, and J. E. Moore. *Antiferromagnetic topological insulators.* Phys. Rev. B **81**, 245209 (2010).

[73] L. Fu and C. L. Kane. *Topology, delocalization via average symmetry and the symplectic anderson transition.* Phys. Rev. Lett. **109**, 246605 (2012).

[74] I. C. Fulga, B. van Heck, J. M. Edge, and A. R. Akhmerov. *Statistical topological insulators.* Physical Review B **89** (15), 155424 (2014).

[75] M. Z. Hasan and C. L. Kane. *Colloquium: Topological insulators.* Rev. Mod. Phys. **82**, 3045 (2010).

[76] X.-L. Qi and S.-C. Zhang. *Topological insulators and superconductors.* Rev. Mod. Phys. **83**, 1057 (2011).

[77] A. M. Essin and V. Gurarie. *Antiferromagnetic topological insulators in cold atomic gases.* Phys. Rev. B **85**, 195116 (2012).

[78] C. Fang, M. J. Gilbert, and B. A. Bernevig. *Topological insulators with commensurate antiferromagnetism.* Phys. Rev. B **88**, 085406 (2013).

[79] C.-X. Liu. *Antiferromagnetic crystalline topological insulators.* arXiv:1304.6455.

[80] C.-X. Liu, R.-X. Zhang, and B. K. VanLeeuwen. *Topological non-symmorphic crystalline insulators.* Phys. Rev. B **90**, 085304 (2014).

[81] J. Li, R.-L. Chu, J. K. Jain, and S.-Q. Shen. *Topological Anderson Insulator.* Phys. Rev. Lett. **102**, 136806 (2009).

[82] C. W. Groth, M. Wimmer, A. R. Akhmerov, J. Tworzydło, and C. W. J. Beenakker. *Theory of the Topological Anderson Insulator.* Phys. Rev. Lett. **103**, 196805 (2009).

[83] H.-M. Guo, G. Rosenberg, G. Refael, and M. Franz. *Topological Anderson Insulator in Three Dimensions.* Phys. Rev. Lett. **105**, 216601 (2010).

[84] K. Kobayashi, T. Ohtsuki, and K.-I. Imura. *Disordered Weak and Strong Topological Insulators.* Phys. Rev. Lett. **110**, 236803 (2013).

[85] X.-L. Qi, Y.-S. Wu, and S.-C. Zhang. *Topological quantization of the spin Hall effect in two-dimensional paramagnetic semiconductors.* Phys. Rev. B **74**, 085308 (2006).

[86] J. T. Chalker and A. Dohmen. *Three-Dimensional Disordered Conductors in a Strong Magnetic Field: Surface States and Quantum Hall Plateaus.* Phys. Rev. Lett. **75**, 4496 (1995).

[87] L. Balents and M. P. A. Fisher. *Chiral Surface States in the Bulk Quantum Hall Effect.* Phys. Rev. Lett. **76**, 2782 (1996).

[88] R.-J. Slager, A. Mesaros, V. Juricic, and J. Zaanen. *The space group classification of topological band-insulators.* Nat. Phys. **9**, 98 (2013).

[89] C. W. J. Beenakker. *Colloquium: Andreev reflection and Klein tunneling in graphene.* Rev. Mod. Phys. **80**, 1337 (2008).

[90] M. I. Katsnelson. *Graphene: Carbon in Two Dimensions.* (Cambridge University Press, 2012).

[91] J. Tworzydło, B. Trauzettel, M. Titov, A. Rycerz, and C. W. J. Beenakker. *Sub-Poissonian Shot Noise in Graphene.* Phys. Rev. Lett. **96**, 246802 (2006).

[92] K. Nomura, S. Ryu, M. Koshino, C. Mudry, and A. Furusaki. *Quantum Hall Effect of Massless Dirac Fermions in a Vanishing Magnetic Field.* Phys. Rev. Lett. **100**, 246806 (2008).

[93] C. W. Groth, M. Wimmer, A. R. Akhmerov, and X. Waintal. *Kwant: a software package for quantum transport.* New J. Phys. **16**, 063065(2014).

[94] G. E. Volovik. *The Universe in a Helium Droplet.* (Clarendon, Oxford, 2003).

[95] J. Zhou, H. Jiang, Q. Niu, and J. Shi. *Topological Invariants of Metals and the Related Physical Effects.* Chinese Phys. Lett. **30**, 027101 (2013).

[96] G Başar, D. E. Kharzeev, and H.-U. Yee. *Triangle anomaly in Weyl semimetals.* Phys. Rev. B **89**, 035142 (2014).

[97] M.-C. Chang and M.-F. Yang. *Chiral magnetic effect in a two-band lattice model of Weyl semimetal.* Phys. Rev. B **91**, 115203 (2015).

[98] Y. Alavirad and J. D. Sau. *Role of boundary conditions, topology, and disorder in the chiral magnetic effect in Weyl semimetals.* Phys. Rev. B **94**, 115160 (2016).

[99] J. Ma and D. A. Pesin. *Chiral magnetic effect and natural optical activity in metals with or without Weyl points.* Phys. Rev. B **92**, 235205 (2015).

[100] S. Zhong, J. E. Moore, and I. Souza. *Gyrotropic Magnetic Effect and the Magnetic Moment on the Fermi Surface.* Phys. Rev. Lett. **116**, 077201 (2016)

[101] A. Vilenkin. *Equilibrium parity-violating current in a magnetic field.* Phys. Rev. D **22**, 3080 (1980).

[102] A. Y. Alekseev, V. V. Cheianov, and J. Fröhlich. *Universality of Transport Properties in Equilibrium, the Goldstone Theorem, and Chiral Anomaly.* Phys. Rev. Lett. **81**, 3503 (1998).

[103] M. Giovannini and M. E. Shaposhnikov. *Primordial hypermagnetic fields and the triangle anomaly.* Phys. Rev. D **57**, 2186 (1998).

[104] K. Fukushima, D. E. Kharzeev, and H. J. Warringa. *Chiral magnetic effect.* Phys. Rev. D **78**, 074033 (2008).

[105] P. Hosur and X. L. Qi. *Recent developments in transport phenomena in Weyl semimetals.* C. R. Phys. **14**, 857 (2013).

[106] D. E. Kharzeev. *The Chiral Magnetic Effect and anomaly-induced transport.* Prog. Part. Nucl. Phys. **75**, 133 (2014).

[107] A. A. Burkov. *Chiral anomaly and transport in Weyl metals.* J. Phys. Condens. Matter **27**, 113201 (2015).

[108] N. Xu, H. M. Weng, B. Q. Lv, C. E. Matt, J. Park, F. Bisti, V. N. Strocov, D. Gawryluk, E. Pomjakushina, K. Conder, N. C. Plumb, M. Radovic, G. Autès, O. V. Yazyev, Z. Fang, X. Dai, T. Qian, J. Mesot, H. Ding, and M. Shi. *Observation of Weyl nodes and Fermi arcs in tantalum phosphide.* Nat. Commun. **7**, 11006 (2016).

[109] J. Xiong, S. K. Kushwaha, T. Liang, J. W. Krizan, M. Hirschberger, W. Wang, R. J. Cava, and N. P. Ong. *Evidence for the chiral anomaly in the Dirac semimetal Na_3Bi.* Science **350**, 413 (2015).

[110] X. Huang, L. Zhao, Y. Long, P. Wang, D. Chen, Z. Yang, H. Liang, M. Xue, H. Weng, Z. Fang, X. Dai, and G. Chen. *Observation of the Chiral-Anomaly-Induced Negative Magnetoresistance in 3D Weyl Semimetal TaAs.* Phys. Rev. X **5**, 031023 (2015).

[111] Q. Li, D. E. Kharzeev, C. Zhang, Y. Huang, I. Pletikosic, A. V. Fedorov, R. D. Zhong, J. A. Schneeloch, G. D. Gu, and T. Valla. *Chiral magnetic effect in $ZrTe_5$.* Nat. Phys. **12**, 550 (2016)

[112] C. Zhang, S.-Y. Xu, I. Belopolski, Z. Yuan, Z. Lin, B. Tong, N. Alidoust, C.-C. Lee, S.-M. Huang, H. Lin, M. Neupane, D. S. Sanchez, H. Zheng, G. Bian, J. Wang, C. Zhang, T. Neupert, M. Z. Hasan, and S. Jia. *Observation of the Adler-Bell-Jackiw chiral anomaly in a Weyl semimetal.* arXiv:1503.02630.

[113] J. Behrends, A. G. Grushin, T. Ojanen, and J. H. Bardarson. *Visualizing the chiral anomaly in Dirac and Weyl semimetals with photoemission spectroscopy.* Phys. Rev. B **93**, 075114 (2016).

[114] C. Zhang, E. Zhang, W. Wang, Y. Liu, Z.-G. Chen, S. Lu, S. Liang, J. Cao, X. Yuan, L. Tang, Q. Li, C. Zhou, T. Gu, Y. Wu, J. Zou, and F. Xiu. *Room-temperature chiral charge pumping in Dirac semimetals.* arXiv:1504.07698.

[115] F. Arnold, C. Shekhar, S.-C. Wu, Y. Sun, R. D. dos Reis, N. Kumar, M. Naumann, M. O. Ajeesh, M. Schmidt, A. G. Grushin, J. H. Bardarson, M. Baenitz, D. Sokolov, H. Borrmann, M. Nicklas, C. Felser, E. Hassinger, and B. Yan. *Negative magnetoresistance without well-defined chirality in the Weyl semimetal TaP.* Nat. Commun. **7**, 11615 (2016).

[116] The experimental developments are reviewed in: A. Vishwanath. *Viewpoint: Where the Weyl Things Are.* Physics **8**, 84 (2015); B. A. Bernevig. *It's been a Weyl coming.* Nat. Phys. **11**, 698 (2015); A. A. Burkov. *Chiral anomaly without relativity.* Science **350**, 378 (2015).

[117] U. Khanna, D. K. Mukherjee, A. Kundu, and S. Rao, *Chiral nodes and oscillations in the Josephson current in Weyl semimetals*, Phys. Rev. B **93**, 121409 (2016).

[118] F. D. M. Haldane. *Attachment of Surface "Fermi Arcs" to the Bulk Fermi Surface: "Fermi-Level Plumbing" in Topological Metals.* arXiv:1401.0529.

[119] E. V. Gorbar, V. A. Miransky, I. A. Shovkovy, and P. O. Sukhachov. *Chiral separation and chiral magnetic effects in a slab: The role of boundaries.* Phys. Rev. B **92**, 245440 (2015)

[120] S. N. Valgushev, M. Puhr, and P. V. Buividovich. *Chiral Magnetic Effect in finite-size samples of parity-breaking Weyl semimetals.* arXiv:1512.01405.

[121] S. Datta, *Electronic Transport in Mesoscopic Systems* (Cambridge University Press, 1997).

[122] Y. Imry, *Introduction to Mesoscopic Physics* (Oxford University Press, 2008).

[123] Yu. V. Nazarov and Ya. M. Blanter, *Quantum Transport: Introduction to Nanoscience* (Cambridge University Press, 2009).

[124] D. E. Kharzeev and H. J. Warringa. *Chiral magnetic conductivity.* Phys. Rev. D **80**, 034028 (2009).

[125] K. Landsteiner, E. Megías, and F. Pena-Benitez. *Gravitational Anomaly and Transport Phenomena*. Phys. Rev. Lett. **107**, 021601 (2011).

[126] A. C. Potter, I. Kimchi, and A. Vishwanath. *Quantum oscillations from surface Fermi-arcs in Weyl and Dirac semi-metals*. Nat. Commun. **5**, 5161 (2014).

[127] Y. Zhang, D. Bulmash, P. Hosur, A. C. Potter, and A. Vishwanath. *Quantum oscillations from generic surface Fermi arcs and bulk chiral modes in Weyl semimetals*. Sci. Rep. **6**, 23741 (2016).

[128] S. Uchida, T. Habe, and Y. Asano. *Andreev reflection in Weyl semimetals*. J. Phys. Soc. Japan **83**, 064711 (2014).

[129] U. Khanna, A. Kundu, S. Pradhan, and S. Rao. *Proximity-induced superconductivity in Weyl semimetals*. Phys. Rev. B **90**, 195430 (2014).

[130] W. Chen, L. Jiang, R. Shen, L. Sheng, B. G. Wang, and D. Y. Xing. *Specular Andreev reflection in inversion-symmetric Weyl semimetals*. EPL **103**, 27006 (2013).

[131] H. Hoppe, U. Zülicke, and G. Schön. *Andreev reflection in strong magnetic fields*. Phys. Rev. Lett. **84**, 1804 (2000).

[132] P. Rakyta, A. Kormányos, Z. Kaufmann, and J. Cserti. *Andreev edge channels and magnetic focusing in normal-superconductor systems: A semiclassical analysis*. Phys. Rev. B **76**, 064516 (2007).

[133] J. A. M. van Ostaay, A. R. Akhmerov, and C. W. J. Beenakker. *Spin-triplet supercurrent carried by quantum Hall edge states through a Josephson junction*. Phys. Rev. B **83**, 195441 (2011).

[134] C. W. J. Beenakker. *Search for Majorana fermions in superconductors*. Annu. Rev. Condens. Matter Phys. **4**, 113 (2013).

[135] S. R. Elliott and M. Franz. *Majorana Fermions in nuclear, particle and solid-state physics*. Rev. Mod. Phys. **87**, 137 (2015).

[136] M. Sato and S. Fujimoto. *Majorana fermions and topology in superconductors*. J. Phys. Soc. Japan **85**, 072001 (2016).

[137] S. Murakami and N. Nagaosa. *Berry phase in magnetic superconductors*. Phys. Rev. Lett. **90**, 057002 (2003).

[138] P. A. Lee, N. Nagaosa, and X. G. Wen. *Doping a Mott insulator: Physics of high-temperature superconductivity*. Rev. Mod. Phys. **78**, 17 (2006).

[139] P. Corboz, T. M. Rice, and M. Troyer. *Competing States in the $t-J$ Model: Uniform d-Wave State versus Stripe State*. Phys. Rev. Lett. **113**, 046402 (2014).

[140] E. Fradkin, S. A. Kivelson, and J. M. Tranquada. *Colloquium: Theory of intertwined orders in high temperature superconductors*. Rev. Mod. Phys. **87**, 457 (2015).

[141] A. Himeda, T. Kato, and M. Ogata. *Stripe States with Spatially Oscillating d-Wave Superconductivity in the Two-Dimensional $t-t'-J$ Model*. Phys. Rev. Lett. **88**, 117001 (2002).

[142] H.-D. Chen, O. Vafek, A. Yazdani, and S.-C. Zhang. *Pair Density Wave in the Pseudogap State of High Temperature Superconductors*. Phys. Rev. Lett. **93**, 187002 (2004).

[143] E. Berg, E. Fradkin, E.-A. Kim, S. A. Kivelson, V. Oganesyan, J. M. Tranquada, and S.-C. Zhang. *Dynamical Layer Decoupling in a Stripe-Ordered High-T_c Superconductor*. Phys. Rev. Lett. **99**, 127003 (2007).

[144] M. Raczkowski, M. Capello, D. Poilblanc, R. Frésard, and A. M. Oleś. *Unidirectional d-wave superconducting domains in the two-dimensional $t-J$ model*. Phys. Rev. B **76**, 140505 (2007).

[145] E. Berg, E. Fradkin, S. A. Kivelson, and J. M. Tranquada. *Striped superconductors: how spin, charge and superconducting orders intertwine in the cuprates*. New J. Phys. **11**, 115004 (2009).

[146] A. Larkin and Y. Ovchinnikov. *Nonuniform state of superconductors*. JETP **20**, 762 (1965).

[147] R. Casalbuoni and G. Nardulli. *Inhomogeneous superconductivity in condensed matter and QCD*. Rev. Mod. Phys. **76**, 263 (2004).

[148] G. Baskaran, Z. Zou, and P. W. Anderson. *The resonating valence bond state and high-Tc superconductivity — A mean field theory*. Solid State Commun. **63**, 973 (1987).

[149] G. Kotliar. *Resonating valence bonds and d-wave superconductivity*. Phys. Rev. B **37**, 3664 (1988).

[150] G. Kotliar and J. Liu. *Superexchange mechanism and d-wave super-conductivity.* Phys. Rev. B **38**, 5142 (1988).

[151] T. Senthil and P.A. Lee. *Coherence and Pairing in a Doped Mott Insulator: Application to the Cuprates.* Phys. Rev. Lett. **103**, 076402 (2009).

[152] S.-S. Lee, P. A. Lee and T. Senthil. *Amperean Pairing Instability in the U(1) Spin Liquid State with Fermi Surface and Application to $\kappa - (BEDT - TTF)_2 Cu_2 (CN)_3$.* Phys. Rev. Lett. **98**, 067006 (2007).

[153] R.-H. He, M. Hashimoto, H. Karapetyan, J. D. Koralek, J. P. Hinton, J. P. Testaud, V. Nathan, Y. Yoshida, H. Yao, K. Tanaka, W. Meevasana, R. G. Moore, D. H. Lu, S.-K. Mo, M. Ishikado, H. Eisaki, Z. Hussain, T. P. Devereaux, S. A. Kivelson, J. Orenstein, A. Kapitulnik, and Z.-X. Shen. *From a Single-Band Metal to a High-Temperature Superconductor via Two Thermal Phase Transitions.* Science **331**, 1579 (2011).

[154] C. Howald, H. Eisaki, N. Kaneko, and A. Kapitulnik. *Coexistence of periodic modulation of quasiparticle states and superconductivity in $Bi_2 Sr_2 CaCu_2 O_{8+\delta}$.* Proc. Natl. Acad. Sci. U.S.A. **100**, 9705 (2003).

[155] M. Vershinin, S. Misra, S. Ono, Y. Abe, Y. Ando, and A. Yazdani. *Local Ordering in the Pseudogap State of the High-Tc Superconductor $Bi_2 Sr_2 CaCu_2 O_{8+\delta}$.*, Science **303**, 1995 (2004).

[156] T. Hanaguri, C. Lupien, Y. Kohsaka, D-H. Lee, M. Azuma, M. Takano, H. Takagi, and J. C. Davis. *A 'checkerboard' electronic crystal state in lightly hole-doped $Ca_{2-x} Na_x CuO_2 Cl_2$.* Nature **430**,1001 (2004).

[157] W.D. Wise, M. C. Boyer, K. Chatterjee, T. Kondo, T. Takeuchi, H. Ikuta, Y. Wang, and E. W. Hudson. *Charge-density-wave origin of cuprate checkerboard visualized by scanning tunnelling microscopy.* Nat. Phys. **4**, 696 (2008).

[158] G. Ghiringhelli, M. Le Tacon, M. Minola, S. Blanco-Canosa, C. Mazzoli, N. B. Brookes, G. M. De Luca, A. Frano, D. G. Hawthorn, F. He, T. Loew, M. Moretti Sala, D. C. Peets, M. Salluzzo, E. Schierle, R. Sutarto, G. A. Sawatzky, E. Weschke, B. Keimer, and L. Braicovich. *Long-Range Incommensurate Charge Fluctuations in $(Y, Nd) Ba_2 Cu_3 O_{6+x}$.* Science **337**, 821 (2012).

[159] J. Chang, E. Blackburn, A. T. Holmes, N. B. Christensen, J. Larsen, J. Mesot, R. Liang, D. A. Bonn, W. N. Hardy, A. Watenphul, M. von Zimmermann, E. M. Forgan, and S. M. Hayden. *Direct observation of competition between superconductivity and charge density wave order in $YBa_2Cu_3O_{6.67}$*. Nat. Phys. **8**, 871 (2012).

[160] M. Le Tacon, A. Bosak, S. M. Souliou, G. Dellea, T. Loew, R. Heid, K. P. Bohnen, G. Ghiringhelli, M. Krisch, and B. Keimer. *Inelastic X-ray scattering in $YBa_2Cu_3O_{6.6}$ reveals giant phonon anomalies and elastic central peak due to charge-density-wave formation*. Nat. Phys. **10**, 52 (2014).

[161] R. Comin, A. Frano, M. M. Yee, Y. Yoshida, H. Eisaki, E. Schierle, E. Weschke, R. Sutarto, F. He, A. Soumyanarayanan, Yang He, M. Le Tacon, I. S. Elfimov, J. E. Hoffman, G. A. Sawatzky, B. Keimer, and A. Damascelli. *Charge Order Driven by Fermi-Arc Instability in $Bi_2Sr_{2lx}La_xCuO_{6+\delta}$*. Science **343**, 390 (2014).

[162] E. H. da Silva Neto, P. Aynajian, A. Frano, R. Comin, E. Schierle, E. Weschke, A. Gyenis, J. Wen, J. Schneeloch, Z. Xu, S. Ono, G. Gu, M. Le Tacon, and A. Yazdani. *Ubiquitous Interplay Between Charge Ordering and High-Temperature Superconductivity in Cuprates*. Science **343**, 393 (2014).

[163] R. Comin, R. Sutarto, F. He, E. da Silva Neto, L. Chauviere, A. Frano, R. Liang, W. N. Hardy, D. Bonn, Y. Yoshida, H. Eisaki, J. E. Hoffman, B. Keimer, G. A. Sawatzky, and A. Damascelli. *Symmetry of charge order in cuprates*. Nat. Mater. **14**, 796 (2015).

[164] Y. Wang, L. Li, M. J. Naughton, G. D. Gu, S. Uchida, and N. P. Ong. *Field-Enhanced Diamagnetism in the Pseudogap State of the Cuprate $Bi_2Sr_2CaCu_2O_{8+\delta}$ Superconductor in an Intense Magnetic Field*. Phys. Rev. Lett. **95**, 247002 (2005).

[165] L. Li, Y. Wang, S. Komiya, S. Ono, Y. Ando, G. D. Gu, and N. P. Ong. *Diamagnetism and Cooper pairing above T_c in cuprates*. Phys. Rev. B **81**, 054510 (2010).

[166] A. Dubroka, M. Rössle, K. W. Kim, V. K. Malik, D. Munzar, D. N. Basov, A. A. Schafgans, S. J. Moon, C. T. Lin, D. Haug, V. Hinkov, B. Keimer, Th. Wolf, J. G. Storey, J. L. Tallon, and C. Bernhard. *Evidence of a Precursor Superconducting Phase at Temperatures as High as 180 K in $RBa_2Cu_3O_{7-\delta}(R = Y, Gd, Eu)$ Superconducting*

Crystals from Infrared Spectroscopy. Phys. Rev. Lett. **106**, 047006 (2011).

[167] F. Yu, M. Hirschberger, T. Loew, G. Li, B. J. Lawson, T. Asaba, J. B. Kemper, T. Liang, J. Porras, G. S. Boebinger, J. Singleton, B. Keimer, Lu Li, and N. P. Ong. *Magnetic phase diagram of underdoped $YBa_2Cu_3O_y$ inferred from torque magnetization and thermal conductivity.* Proc. Natl. Acad. Sci. U.S.A. **113**, 12667 (2016).

[168] Q. Cui, C.-R. Hu, J. Y. T. Wei, and K. Yang. *Conductance characteristics between a normal metal and a two-dimensional Fulde-Ferrell-Larkin-Ovchinnikov superconductor: The Fulde-Ferrell state.* Phys. Rev. B **73**, 214514 (2006).

[169] Q. Cui, C.-R. Hu, J. Y. T. Wei, and K. Yang. *Spectroscopic signatures of the Larkin-Ovchinnikov state in the conductance characteristics of a normal-metal/superconductor junction.* Phys. Rev. B **85**, 014503 (2012).

[170] Y. Tanaka,Y. Asano, M. Ichioka and S. Kashiwaya. *Theory of Tunneling Spectroscopy in the Larkin-Ovchinnikov State.* Phys. Rev. Lett **98**, 077001 (2007).

[171] J. Kaczmarczyk, M. Sadzikowski, and J. Spałek. *Andreev reflection between a normal metal and the FFLO superconductor II: A self-consistent approach.* Physica C **471**, 193 (2011).

[172] W. Chen, M. Gong, R. Shen, and D. Y. Xing. *Detecting Fulde–Ferrell superconductors by an Andreev interferometer.* New J. Phys. **16**, 083024 (2014).

[173] J. Schelter, B. Trauzettel, and P. Recher. *How to Distinguish between Specular and Retroconfigurations for Andreev Reflection in Graphene Rings.* Phys. Rev. Lett. **108**, 106603 (2012).

[174] C. W. J. Beenakker. *Specular Andreev Reflection in Graphene.* Phys. Rev. Lett. **97**, 067007 (2006).

[175] L. Hofstetter, S. Csonka, J. Nygård, and C. Schönenberger, *Cooper pair splitter realized in a two-quantum-dot Y-junction.* Nature **461**, 960 (2009).

[176] G. E. Blonder, M. Tinkham and T. M. Klapwijk. *Transition from metallic to tunneling regimes in superconducting microconstrictions:*

Excess current, charge imbalance, and supercurrent conversion. Phys. Rev. B **25**, 4515 (1982).

[177] M. H. Hamidian, S. D. Edkins, Sang Hyun Joo, A. Kostin, H. Eisaki, S. Uchida, M. J. Lawler, E.-A. Kim, A. P. Mackenzie, K. Fujita, Jinho Lee, J. C. Séamus Davis. *Detection of a Cooper-pair density wave in $Bi_2Sr_2CaCu_2O_{8+x}$*. Nature **532**, 343 (2016).

[178] U. Schneider, L. Hackermüller, S. Will, Th. Best, I. Bloch, T. A. Costi, R. W. Helmes, D. Rasch, and A. Rosch. *Metallic and Insulating Phases of Repulsively Interacting Fermions in a 3D Optical Lattice*. Science **322**, 1520 (2008).

[179] S. Krinner, D. Stadler, D. Husmann, J.-Ph. Brantut, and T. Esslinger. *Observation of quantized conductance in neutral matter*. Nature **517**, 64 (2014).

Samenvatting

Topologische halfmetalen zijn een nieuwe klasse van materialen, waarin de geleidingsband en de valentieband elkaar toevalligerwijs raken in afzonderlijke punten van de Brillouin-zone. In de nabijheid van deze raakpunten, is de dispersierelatie lineair en bewegen de massaloze excitaties zich met een energie-onafhankelijke snelheid (net zoals de lichtsnelheid voor fotonen). Dit veroorzaakt fascinerende transporteigenschappen die waargenomen zijn in het tweedimensionale halfmetaal grafeen.

In drie dimensies wordt het verhaal nog een stuk interessanter. De toevallige raakpunten zijn dan beschermd door de topologie van de derde ruimtelijke dimensie. Nabij de Fermi-energie bestaat het spectrum uit een even aantal conussen, die elk beschreven worden door de Weyl-vergelijking uit de relativistische quantummechanica. De Weyl-conussen hebben een linkshandige of rechtshandige draaiing die "chiraliteit" of "Berry-kromming" wordt genoemd. Deze unieke eigenschappen veroorzaken opmerkelijke elektromagnetische eigenschappen, zoals een zeer grote negatieve magnetoweerstand, chirale Landau-niveaus, en het chirale magneto-elektrische effect. Aan het oppervlak van een Weyl halfmetaal bestaat het Fermi-oppervlak uit open contours, de zogenaamde Fermi-bogen. Fermi-bogen beginnen en eindigen bij de projectie van de Weyl-conussen in het binnenste op de Brillouin-zone aan het oppervlak. Deze topologisch beschermde toestanden en hun transporteigenschappen vormen het hoofdonderwerp van dit proefschrift.

We beginnen in hoofdstuk twee met de studie van de hieraan verwante antiferromagnetische topologische isolatoren. In deze systemen is tijdomkeersymmetrie lokaal gebroken maar globaal hersteld door de combinatie met translatie over een halve eenheidscel. Anders dan de afzonderlijke tijdomkeersymmetrie, wordt deze gecombineerde symmetrie verstoord door wanorde. In onze studie vinden we echter dat de symmetrie *gemiddelderwijs* behouden blijft. (Dit is een voorbeeld van een *statistische* topologische isolator.) Bij de faseovergang tussen een gewone isolator en een antiferromagnetische topologische iolator sluit de energie-gap zich op afzonderlijke punten in de Brillouin-zone. Daar ontstaat een lineair spectrum van Weyl conussen.

In een Weyl halfmetaal wordt de antiferromagnetische koppeling vervan-

gen door een ferromagnetische koppeling. Dit breekt de tijdomkeersymmetrie en stabiliseert de halfmetallische fase. In hoofdstuk drie van dit proefschrift bestuderen wij één van de meest kenmerkende transporteigenschappen van een Weyl halfmetaal, het zogenaamde chirale magnetische effect. Dit is één van de eigenschappen die een Weyl halfmetaal onderscheiden van grafeen. Voor dit effect is een sterk magnetisch veld met Landauniveaus nodig. Wat we ontdekt hebben, is dat er een variant van hetzelfde chirale magnetische effect mogelijk is in een zwak magnetisch veld, zonder Landauniveaus. Deze variant is vermoedelijk eenvoudiger waar te nemen in een experiment.

In het vierde hoofdstuk vervolgen we de studie van de oppervlakte Fermi-bogen. Terwijl deze duidelijk waargenomen zijn in optische experimenten, kunnen sommige van hun unieke eigenschappen alleen onderzocht worden in transportexperimenten. De grote moeilijkheid bij het uitvoeren van zo'n transportexperiment is dat een Weyl halfmetaal, in tegenstelling tot een topologische isolator, zowel een geleidend oppervlak als een geleidende binnenkant heeft. Het is daardoor moeilijk om oppervlakte en binnenkant van elkaar te onderscheiden. Wij benaderen dit probleem door het Weyl halfmetaal in contact te brengen met een supergeleider. De supergeleider heeft geen invloed op de binnenkant van het Weyl halfmetaal, maar het splitst de Fermi-bogen in bijna ladingsneutrale Majorana banden. We laten zien hoe we door middel van een tunnelbarrière Majorana deeltjes kunnen opsluiten.

In het vijfde hoofdstuk verlaten wij het terrein van de halfmetalen om Fermi-bogen te bestuderen in supergeleiders. In koperhoudende supergeleiders bij hoge temperatuur zijn Fermi-bogen waargenomen en geïnterpreteerd als tekenen van een nieuw soort paarvorming van de elektronen, genaamd Ampère-paarvorming omdat de aantrekkende kracht lijkt op de Ampèrekracht tussen gelijkgerichte evenwijdige stroomdraden. We onderzoeken hoe de Andreev-verstrooiing van elektronen in gaten door de Ampère-paarvorming beïnvloed wordt. We sluiten af met een voorstel voor een geleidingsexperiment in een Y-vormige junctie, dat gebruikt zou kunnen worden om de Ampère-paarvorming te detecteren.

Summary

Topological semimetals are a new class of materials, in which the conductance and the valence band touch accidentally at discrete points of the Brillouin zone. Near these touching points, the dispersion relation is linear and the massless excitations move with an energy-independent velocity (much like the speed of light for photons). This leads to fascinating transport properties, that have been observed in the two-dimensional semimetal graphene.

In three dimensions, the story becomes even more interesting. The accidental touching points are topologically protected by the third spatial dimension. Near the Fermi energy, the spectrum consists of an even number of cones, each of which is described by the Weyl equation of relativistic quantum mechanics. The Weyl cones come in two different chiralities, they are sources and sinks of Berry curvature. These unique features lead to remarkable electromagnetic properties such as a huge negative magnetoresistance, chiral Landau levels, and the chiral magnetic effect. At the surface of a Weyl semimetal, the Fermi surface consists of open contours, called Fermi arcs. Fermi arcs start and end at projections of the bulk Weyl cones onto the surface Brillouin zone. These topologically protected states and their transport properties are the main focus of this thesis.

We begin in chapter two by studying the related antiferromagnetic topological insulators. In these systems time-reversal symmetry is broken locally but restored in conjunction with a translation by half a unit cell. Unlike true time-reversal symmetry, this effective time-reversal symmetry is destroyed by disorder. In our studies however, we find a remarkable robustness of the topological phase against electrostatic disorder. The reason is that the symmetry still holds *on average*, placing the antiferromagnetic topological insulator in the class of statistical topological insulators. At the phase transition between a normal insulator and an antiferromagnetic topological insulator the bulk gap closes at discrete points in the Brillouin zone, forming a linear low energy spectrum: Weyl cones.

In a Weyl semimetal, the antiferromagnetic coupling is replaced by a ferromagnetic coupling. This breaks time-reversal symmetry and stabilizes the Weyl semimetal phase. In chapter three of this thesis, we study one

of the key transport signatures of a Weyl semimetal, the chiral magnetic effect. It is one of the features that distinguishes a Weyl semimetal from graphene. For this effect, a magnetic field strong enough to form Landau levels is needed. We find that there also exists a variant of the chiral magnetic effect in a weak magnetic field without Landau levels. This variant is likely to be more easily accessible in an experimental setting.

In the fourth chapter, we continue to study the surface Fermi arcs. While they have been clearly observed in optical experiments, some of their unique properties can only be probed by transport experiments. A key difficulty in devising such a transport experiment is that, in contrast to a topological insulator, both the bulk and the surface of a Weyl semimetal are conducting. Therefore, it is difficult to distinguish the surface from the bulk response. We address this problem by bringing the Weyl semimetal with broken time-reversal symmetry in contact with a conventional superconductor. The superconductor does not affect the bulk of the Weyl semimetal, but splits the Fermi arcs into nearly charge neutral Majorana modes. We show how we can trap Majorana fermions using a tunnel barrier.

In the fifth chapter, we venture beyond the horizon of Weyl semimetals and study Fermi arcs in the pseudo-gap phase of high temperature cuprate superconductors. These have been interpreted as signatures of a novel pairing mechanism called "Amperian pairing", because the attraction resembles the Amperian force of parallel electrical currents. We examine how the Andreev scattering of electrons into holes is affected by the Amperian pairing. We conclude by showing how a transport experiment in a tri-junction can be used to detect the Amperian pairing.

Curriculum Vitæ

I was born in Freiburg im Breisgau, Germany, in 1985. I spent most of my youth in Kenzingen, where I attended primary and secondary school. After graduating from Gymnasium Kenzingen in 2005, I travelled to Australia and China, where I worked in various jobs over the course of a year.

In 2006, I started studying physics at Karlsruhe Institute of Technology. During my studies, I was fortunate to spend a year at Princeton University with a stipend from the German Academic Exchange Service (DAAD). After this experience, I returned to Karlsruhe to complete my studies with a Diploma thesis on "Squeezed Light Emitting Diodes", under the supervision of Prof. Dr. Jörg Schmalian in 2012.

In 2013, I joined the group of Prof. Dr. Carlo Beenakker as a PhD student at Instituut-Lorentz, Leiden University. During my time in Leiden, I was teaching assistant for the quantum theory class. I participated in several schools and conferences, and presented my work in The Netherlands, Germany, France, Italy, Poland, Norway, and the USA.

List of publications

- P. Baireuther, P. P. Orth, I. Vekhter, and J. Schmalian. *Manipulation of a two-photon pump in superconductor-semiconductor heterostructures.* Physical Review Letters **112**, 077003 (2014).

- P. Baireuther, J. M. Edge, I. C. Fulga, C. W. J. Beenakker, and J. Tworzydło. *Quantum phase transitions of a disordered antiferromagnetic topological insulator.* Physical Review B **89**, 035410 (2014).
  [Chapter 2]

- P. Baireuther, T. Hyart, B. Tarasinski, and C. W. J. Beenakker. *Andreev-Bragg reflection from an Amperian superconductor.* Physical Review Letters **115**, 097001 (2015). [Chapter 5]

- P. Baireuther, J. A. Hutasoit, J. Tworzydło, and C. W. J. Beenakker. *Scattering theory of the chiral magnetic effect in a Weyl semimetal: interplay of bulk Weyl cones and surface Fermi arcs.* New Journal of Physics **18**, 045009 (2016). [Chapter 3]

- P. Baireuther, J. Tworzydło, M. Breitkreiz, İ. Adagideli, and C. W. J. Beenakker. *Weyl-Majorana solenoid.* New Journal of Physics **19**, 025006 (2017). [Chapter 4]